CRYSTAL GROWTH OF ORGANIC-INORGANIC LEAD HALIDE PEROVSKITES: IMPACT OF KINETIC PARAMETERS ON MORPHOLOGY, STRUCTURE AND PROPERTIES

A Dissertation
Presented to the Faculty of the Graduate School
of Cornell University
In Partial Fulfillment of the Requirements for the Degree of
Doctor of Philosophy

by
David Todd Moore
January 2015

© 2015 David Todd Moore

CRYSTAL GROWTH OF ORGANIC-INORGANIC LEAD HALIDE PEROVSKITES: IMPACT OF KINETIC PARAMETERS ON MORPHOLOGY, STRUCTURE AND PROPERTIES

David Todd Moore, Ph.D.
Cornell University, 2015

In this work I present both a phenomenological and fundamental study of the crystallization of the organic-inorganic halide perovskites; this includes determining the overall structural evolution, extraction of kinetic parameters for the primary crystallization step, and establishing several processing-structure relationships. In addition, I will show examples of the application of the primary results to control crystal growth and enhance the material's performance in working devices.

The organic-inorganic halide perovskites have shown great promise as a potential next generation photovoltaic (PV) material with device efficiencies exceeding 17%. For the last 2-3 years most research efforts have been dedicated to understanding the general operating principles of perovskite PV devices and engineering better device architectures. Although these efforts have resulted in an unprecedented increase in efficiencies over a very short period of time, many reports point to film or crystal morphology as a limiting factor.

In order to control film and crystal growth a better understanding of this systems fundamental crystallization behavior is needed. Employing in-situ wide angle X-ray scattering allowed for the determination of the general evolution of thin films cast from solution. This initial work revealed an Ostwald Step Rule path in which the final perovskite is preceded by a solid-state precursor structure. Understanding the general evolution allowed for monitoring of the precursor-perovskite transition to establish processing-structure relationships. One such relationship is the temperature profile used in the annealing step, optimization of this profile results in better film coverage and better crystal texture, both of which increase device performance. The second major study was to elucidate the disposition of the constituent salts during

crystallization and confirmed that all reagent salts are completely dissociated during film formation. This result led to the realization that the crystallization was insensitive to the lead source allowing for manipulation of the system kinetics by using alternate lead compounds. Finally, a study of the kinetics of the precursor-perovskite transition provided for the extraction of the activation energy. Combined with the previous work, the kinetics study gave the insights needed to determine a general formula for the precursor structure as well as a general pathway for the solid-state transformation.

The implication of the work presented here is better control of perovskite thin film growth through manipulation of the processing and chemistry employed. Several recent reports, as well as my own experimental results, are beginning to show the value of this understanding through better films, made at lower temperatures and faster times, and providing improved performance in working PV devices.

BIOGRAPHICAL SKETCH

David Todd Moore was born to Donna M. Stringer and Vern L. Moore in Portland, Oregon in 1964; the Year of the Dragon. Our family moved to Sacramento, California in 1967 where I remained until I was 17 years of age. Although we were not below the poverty line, we could see it from our house and I attended schools that principally served underprivileged students. School was not a priority for me while growing up and so, after graduating high school, I chose the service as a way out.

I served 4 years in the US Army providing signal intelligence for special operations command as a member of the 18th Airborne Corps at Ft. Bragg, North Carolina. My service experience included many things that changed me, many of which are beyond the scope of this dissertation; of note, however, is the extensive travel which exposed me to cultures from all over the world, and my job, which exposed me to leading edge technology.

In the 17 years following my service I was lucky to have a wide variety of jobs and experiences including such things as: dock worker, fast-food manager, truck driver, software engineer, and systems engineer for commercial lighting control systems. In the course of my work in the electrical lighting industry I worked for a company that made daylighting control equipment which would switch off electric lighting in response to available daylight; this was my first introduction to energy issues and the challenges that we would face in supplying power for an increasing global demand.

At the end of my career in the lighting industry I began to write software for the Internet and, eventually, started my own company writing Internet based business process automation software. But the software I wrote did nothing to address energy issues, and, after 8 years sold my company so that I could be more directly involved with solving what I saw as a critical global issue.

After some exploration I discerned that my best role in addressing these energy issues was as a scientist working directly on new solar materials and systems that would help move solar energy from a niche technology with limited application to the primary form of power generation. I began school at North Seattle Community

College in the fall of 2005 and transferred to the University of Washington in 2007. In June of 2009 I completed my bachelor's degree in chemical engineering. During my time at the University of Washington I did research on organic photovoltaics under Dr. David Ginger, who then hired me as a research assistant for an additional year to help with the completion of a project.

My success in my undergraduate degree allowed me to gain acceptance to several top universities and, after much reflection, chose Cornell University and the Materials Science & Engineering department to do my PhD studies. In retrospect, the decisions I made during my education were all correct; the University of Washington, Dr. Ginger's research group, and Cornell University have all proven to be critical to both the person and the scientist that I am today. Although others in my field may not agree, or may think that I might have done better for myself in other ways, or may think that I'm not that good a scientist or person I give these words from someone wiser than myself:

"Not one drop of my self worth depends on your acceptance of me".

- Quincy Jones

ACKNOWLEDGEMENTS

It is an incredible challenge to enumerate all those to whom I owe my success and to express, in writing, how important they have been. Any of my work that has any impact, or affects any positive change, is certainly due to their influence in my education and my life. On the other hand, any of the work here that may turn out to be wrong is completely my doing.

I must begin with Dr. Lara Estroff, my advisor, for doing all those things I expected and wanted an advisor to do; teach, push, pull, listen, and freely give of her experience so I wouldn't have to make the mistakes of others before me. But most of all, when I was seeking a research group to finish my studies, she said yes. Taking a chance on me and my research demonstrated a trust and consideration that she had no specific reason to give, other than that is who she is, and I thank her for that.

The balance of my committee, Dr. Darrell Schlom, Dr. John Marohn, and Dr. Uli Wiesner, have been the most involved and active committee that I know of; and I was the lucky recipient of their efforts. Very commonly a graduate student's advisor is involved with their education and research while the minority committee members are fairly absent; in my case, every one of my committee members was intimately aware of and involved in my PhD experience. I thank them all for what they have taught me and specifically note one trait that they all share, and have passed on to me: a childlike excitement for really cool science.

The members of my group, with which I have shared offices, labs, lunches, targeted discussions about science, and random thoughts about cartoon characters, deserve special thanks for so many things. In spite of not being focused on the same area of research, or coming from the same background, they have made me feel at home, have listened to my rants and raves (even when they didn't know what I was talking about), and, each and every one of them, taught me something I otherwise would not have known.

I could not have accomplished the work detailed here without the help and support of many resources at Cornell; these include user facilities such as CHESS, CCMR, and KAUST, but those resources were useless to me if not for the people who

run them. One of the principle techniques used in my studies was X-ray diffraction done at CHESS, but if not for Dr. Detlef Smilgies and Dr. Margeret Koker I would still be trying to acquire and analyze data. The CCMR staff has been exceptional. Particularly Steve Kriske, who frequently let me modify apparatus to accomplish an experiment specific to me (don't worry Steve, I'll deny this if asked); and Phil Carubia, who, on one occasion, came in on his day off to build something for me just because he wanted to help me out (ditto Phil, deny if asked). In addition there were many people around campus who helped me run an experiment, make some widget, analyze some data, or discuss a theory with absolutely no reason to do so other than being nice. Jun Yang, Trent Scott, Brian Leahy, Tiffany Williams, Kayla Nguyen, Eva Smith, Jonathon Saathoff, Brenda Fisher, Nate Ellis, and every one of my group members are some on this list; there are most certainly others I have forgotten to list, to whom I apologize.

Amongst the list of peers, teacher and collaborators I have had I must reserve this last, and most special thank you, to my two principle collaborators; Dr. Hiroaki Sai and Dr. Kwan Tan. They have taught me so much, given so freely of their time, and been so incredibly good at what they do. To them I owe much of my success, specifically Kwan, who was the one who convinced me to study the perovskites. But mostly, they are both exceptional gentlemen, and it has been an honor to be able to know and work with them.

I would not be a student and could not have made it through these last 9 years if not for my family and friends. I will not even begin to try to detail the overwhelming number of friends that have helped and supported me throughout my studies, you know who you are and you know that you have my eternal gratitude. It is my mother, Donna Stringer, who showed me that going to school later in life is possible; and worth it. My Father, Vern Moore, taught me how to work hard and how to judge what's important in life; it has served me well. And my brothers, Scott and Mark, have both provided examples (in very different ways) of how I could be a better man. If not for a family like this, I would not have come this far.

Finally, I want to thank anyone who has ever been a teacher.

TABLE OF CONTENTS

Biographical Sketch iii
Acknowledgements v
List of Figures xi
List of Equations xvi
List of Abbreviations xvii
Chapter 1 Introduction 1
1.1 Introduction 1
1.2 History, Challenges and Materials 1
1.2.1 Challenges for PV adoption 2
1.2.2 Next Generation Materials 5
1.3 Device architecture and photophysics of PIN materials 6
1.3.1 Ideality of the absorbing layer 9
1.4 Methylammonium lead halide perovskites 10
1.4.1 $(MA)PbX_3$ for PV applications 12
1.5 Processing-Structure relationships 13
1.5.1 Crystallization Theory and Models 14
1.6 Processing-Structure Relationships for $(MA)PbX_3$ 18
1.7 Structure-Property Relationships 20
1.8 Future Work 20
1.9 References 22
Chapter 2 A detailed balance analysis of conversion efficiencies limits for nanocrystal solar cells – Relating the shape of the excitonic peak to conversion efficiencies 27
2.1 Abstract 27
2.2 Introduction 27
2.3 Results and Discussion 28
2.4 Conclusions 38
2.5 References 39

2.6 Supporting Information 41
2.6.1 Calculation of current density and short circuit voltage..... 41
2.6.2 Detailed absorption model and comparison to experimental spectra 42
2.6.3 The relationship between peak-to-valley ratio of the NC absorption profile on PV conversion efficiency. 44
2.6.4 The nature of the low energy absorption tail 45
2.6.5 Conversion efficiency limits in the tandem NC solar cell..... 45
2.6.6 Choice of Spectrum 46
2.6.7 Modeling of quantum yield in the case of multiexciton generation 47
Chapter 3 Thermally Induced Structural Evolution and Performance of Mesoporous Block Copolymer-Directed Alumina Perovskite Solar Cells 49
3.1 Abstract..... 49
3.2 Introduction 49
3.3 Results and Discussion 51
3.3.1 GIWAXS of $CH_3NH_3PbI_{3-x}Cl_x$ Perovskites 51
3.3.2 Characterization of Mesoporous Block Copolymer-Directed Alumina Thin Films..... 52
3.3.3 In situ X-ray Characterization of MBCP-Al_2O_3 Perovskite Structural Evolution..... 53
3.3.4 MBCP-Al_2O_3 Perovskite Solar Cell Performance..... 59
3.4 Conclusion 60
3.5 Methods 61
3.6 References 66
3.7 Supporting Information 72
Chapter 4 Impact of the Organic Halide Salt on Final Perovskite Composition for Photovoltaic Applications..... 75
4.1 Abstract..... 75
4.2 Introduction 75

4.3 Results and Discussion 76
4.4 Conclusions 83
4.5 References 84
4.6 Supporting Information 87
4.6.1 Experimental Methods 89
Chapter 5 A kinetic study of the organic-inorganic trihalide perovskites: Determination of the precursor material and the role of the lead anion in crystallization 92
5.1 Abstract 92
5.2 Introduction 92
5.3 Results and Discussion 94
5.3.1 Quantifying the precursor-to-perovskite transformation 94
5.3.2 Kinetic modeling of the precursor-to-perovskite transformation 98
5.3.3 Application of the model 101
5.3.4 Dependency of activation energy on the lead salt 103
5.3.5 The precursor phase and the role of the spectator salt 106
5.4 Conclusions 111
5.5 Experimental 111
5.6 References 114
5.7 Supporting Information 117
Chapter 6 Conclusions 121
Appendix A: Ultra-smooth organic-inorganic perovskite thin-film formation and crystallization for Efficient Planar Heterojunction Solar Cells 123
A.1 Abstract 123
A.2 Results 126
A.2.1 Crystallographic structure and evolution of perovskite 126
A.2.2 Perovskite film morphology 132
A.2.3 Optical properties of the perovkite films 134
A.2.4 Photovoltaic performance and characterization 136

A.3 Discussion 139
A.4 Methods 142
A.5 References 145
A.6 Acknowledgements 148
Appendix B: Solution processed Perovskite thin films using an ionic liquid 149

LIST OF FIGURES

Figure 1.1: End user cost for electricity produced from different generation sources. 3
Figure 1.2: Production cost targets for first, second, and third generation PV technologies 4
Figure 1.3: NREL efficiency chart for PV technologies (June 2014) 6
Figure 1.4: Schematic device stack and energy band alignments in PN and PIN type solar cells. 8
Figure 1.5: Absorption spectra for different size nanocrystals. 9
Figure 1.6: Perovskite structures with various representations and variations. 11
Figure 1.7: Energy barrier and driving force effects under classic crystal growth theory. 15
Figure 1.8: Driving forces and energy barriers for crystal growth. 17
Figure 2.1: Model of the excitonic absorption spectrum of semiconductor NCs. 29
Figure 2.2: Absorption profiles for idealized SQ, NC with complete absorption above E_{gap}, and NC with complete absorption at E_{gap}. 32
Figure 2.3: Impact of the absorption tail on conversion efficiency. 34
Figure 2.4: Contour plot of theoretical conversion efficiency as a function of excitonic energy gap, E_{gap}, and peak width, W. 35
Figure 2.5: Conversion efficiency limits of tandem NC solar cells 37
Figure 2.6 Modeled and experimental absorption spectra for colloidal NCs. 43
Figure 2.7: Absorption profiles and maximum efficiency for different peak-to-valley ratios (PR). 44
Figure 2.8: Efficiency plots for the maximum efficiency with E_{en} fixed at 15meV 46
Figure 2.9: MEG absorption functions used for calculating efficiencies 48
Figure 3.1: 2D GIWAXS profiles of $CH_3NH_3PbI_{3-x}Cl_x$ perovskite films for varying solution concentrations. 51
Figure 3.2: SEM micrographs and 2D GISAXS profile of MBCP-Al_2O_3 film after calcination. 53

Figure 3.3: 2D GIWAXS profiles for isothermal annealing of MBCP-Al_2O_3 perovskite films at 100 °C 55
Figure 3.4: 2D GIWAXS profiles for isochronal annealing of MBCP-Al_2O_3 perovskite films in nitrogen 57
Figure 3.5: Plan view SEM micrographs of perovskite crystallization in MBCP-Al_2O_3 with isothermal and isochronal annealing 60
Figure 3.6: AFM surface profile of the MBCP-Al_2O_3 film 72
Figure 3.7: Cross-sectional SEM micrographs and GISAXS profiles of Al_2O_3 72
Figure 3.8: SEM micrographs and GISAXS/GIWAXS profile of MBCP-TiO_2 film 73
Figure 3.9: Plan view and cross-sectional SEM micrographs of 20 wt% perovskite on MBCP-Al_2O_3. 74
Figure 4.1: Schematic of perovskite thin film processing pathways 76
Figure 4.2: Azimuthally integrated GIWAXS data, for evaporated lead halide films soaked in various methylammonium halide solutions 79
Figure 4.3: XRD pattern of evaporated $PbCl_2$ thin film transformed by sublimation of MAI at 150 ºC 81
Figure 4.4: XRD pattern and absorbtion spectrum of perovskite films with $Pb(NO_3)_2$ as the Pb source. 83
Figure 4.5: 2D GIWAXS images of perovskite films made by soaking lead halide films in MA halide salts 87
Figure 4.6: SEM images of $MAPbI_3$ made by soaking lead halide films 88
Figure 4.7: FTIR spectra of films made with solution prepared with $Pb(NO_3)_2$ as the lead source 89
Figure 5.1: WAXS images for 40 wt% solution of $PbCl_2$/(MA)I on Si thermally annealed from ambient temperature to 100ºC 95
Figure 5.2: Kinetic data for isothermally annealed samples made from 40 wt% in DMF using $PbCl_2$ as the lead salt 100
Figure 5.3: Kinetic data for isothermally annealed samples made from 40 wt% in DMF using $Pb(NO_3)_2$ as the lead salt 102

Figure 5.4: Kinetic data for all four systems prepared from a 40 wt% solution in DMF using different lead salts. 105
Figure 5.5: 1D, normalized, integrated WAXS data for thin films within 3 minutes of spin coating 107
Figure 5.6: Schematic representation of the perovskite crystallization and growth pathway. 109
Figure 5.7: 1D radial plots of scattering images from the chloride system integrated over all azimuthal angles 117
Figure 5.8: 1D and 2D scattering data for the precursor and perovskite material for all various lead salts 119
Figure A.1: X-ray diffraction spectra for perovskite films deposited on a FTO/c-TiO_2 substrate from solutions containing different lead sources 126
Figure A.2: In-situ WAXS data for all three lead salt systems 129
Figure A.3: TGA curves and their derivatives for CH_3NH_3X (X= Cl, I, Ac) in nitrogen atmosphere. 131
Figure A.4: SEM images of perovskite films deposited on FTO/c-TiO2 substrates from the three different lead sources 133
Figure A.5: AFM images of perovskite films deposited on a FTO/c-TiO_2 substrate derived from the three different lead sources 134
Figure A.6: UV-Vis absorption spectra for perovskite films deposited on FTO/c-TiO_2 substrates derived from different lead sources 136
Figure A.7: J-V curves at optimized conditions using different lead sources measured under simulated AM1.5 sunlight of 100mW/cm^2 138
Figure A.8: Illustration of the stages in the fabrication of $CH_3NH_3PbI_{3-x}Cl_x$ thin films. 140
Figure B.1: Integrated 2D WAXS patterns for spincast films of (MA)PbI3 using methylammonium formate as the solvent 151
Figure B.2: SEM micrographs of (MA)PbI3 thin films made using (MA) formate as the solvent 152

Figure B.3: SEM micrographs of single crystals grown using methylammonium formate as the solvent 153
Figure B.4: SEM micrographs and XRD pattern of thin film grown using methylammonium formate as the solvent 154

LIST OF TABLES

Table 2.1: Empirical values for absorption model..... 42
Table 3.1: MBCP-Al_2O_3 perovskite solar cell performance parameters averaged over a batch of at least 20 devices measured under 100 mW/cm^2 stimulated AM1.5 sunlight irradiation. 74
Table 4.1: Experimental parameters of $MAPbX_3$ perovskite formation studies. 78
Table 5.1: Extracted kinetic parameters for all four systems based on the global fit shown in Fig. 5.4A..... 104

LIST OF EQUATIONS

Equation 1.1 Generalized equation for the transformed fraction of a solid 14
Equation 1.2 General rate equation for a first order reaction 17
Equation 2.1 Absorption model to include energetic & physical disorder 31
Equation 2.2 Short circuit current density equation 41
Equation 2.3 Open circuit voltage equations 41
Equation 2.4 Short circuit current as a function of voltage 41
Equation 2.5 Power conversion efficiency 42
Equation 2.6 Software implemented absorption function 42
Equation 2.7 Gaussian function for absorption onset 45
Equation 2.8 Hybrid function for absorption onset 45
Equation 2.9 Short circuit current for the top cell in a tandem configuration 44
Equation 2.10 Shor circuit current for the bottom cell in a tandem configuration 45
Equation 2.11 Quantum yield step function for MEG 47
Equation 2.12 Quantum yield with linear increase for MEG 47
Equation 5.1 Definition of transformed fraction from x-ray diffraction 97
Equation 5.2 Arhennius-like function for extracting E_a 99
Equation 5.3 Johnson-Mehl-Avrami equation 100
Equation 5.4 Definition of β function 100
Equation 5.5 Fit function for fitting x-ray diffraction data 101
Equation 5.6 Non-stoichiometric reaction equation for $(MA)PbI_3$ 103

LIST OF ABBREVIATIONS

$CaTiO_3$	Calcium titanate
CB	Conduction band
CdSe	Cadmium selenide
CdTe	Cadmium telluride
CIGS	Copper indium gallium selenide
CuO	Copper oxide
DSSC	Dye sensitized solar cell
E_a	Activation energy
ETM	Electron transport material
FF	Fill factor
G	Gibbs free energy
GaAs	Gallium arsenide
HTM	Hole transport material
Jsc	Short-circuit current
k_b	Boltzmann's constant
kWh	Kilowatt-hour
$LaGaO_3$	Lanthanum gallium oxide
$(MA)PbX_3$	Methyl ammonium lead trihalide (chloride, bromide, iodide)
NCQD	Nanocrystal quantum dot
NiO	Nickel oxide
NREL	National Renewable Energy Labs
P3HT	Poly(3-hexylthiophene-2,5-diyl)
Pedot:PSS	Poly(3,4-ethylenedioxythiophene) Polystyrene sulfonate
PIN	p-type:intrinsic:n-type junction
PN	p-type:n-type junction
PV	Photovoltaics
Si	Silicon

Spiro-OMeTAD	2,2',7,7'-Tetrakis[N,N-di(4-methoxyphenyl)amino]-9,9'-spirobifluorene
SQ	Shockley-Queisser
TiO_2	Titanium dioxide
VB	Valence band
Voc	Open-circuit voltage
WAXS	Wide angle X-ray scattering
ZnO	Zinc oxide
μ	Chemical potential

CHAPTER 1 INTRODUCTION

PHOTOVOLTAICS: HISTORY, CHALLENGES, AND MATERIALS

1.1 Introduction

There is overwhelming evidence that continued use of expendable fuel supplies for energy generation is not a viable, long term strategy, due to both limited supply and detrimental environmental impact.[1] Considering that solar energy is the only renewable energy source with enough energy density to supply the entire global power demand, both today and into any foreseeable future, it is clear that solar energy must be a primary component of any long term energy portfolio.[1] This work considers photovoltaic solar, where the best device efficiencies have been relatively stagnant near 20% (commercial) for almost 20 years,[2] and are based on crystalline silicon as the primary absorber. This lack of improvement should not be taken as an indication of the importance, abundance, or progress of photovoltaic (PV) research and scientists; it is simply due to the fact that silicon makes an exceptionally good solar cell. The lack of adoption of PV as a competitive energy source is because it is expensive, and, as such, the primary thrust of most PV research is on next generation PV materials that will perform with similar efficiencies but be produced at much lower cost. The focus of my research has been the study of emerging systems that show promise as next generation PV materials, specifically the organic-inorganic halide perovskites and their crystallization behavior.

1.2 History, Challenges and Materials

The first experiments to produce a voltage by illuminating a material were in the mid-nineteenth century using silver chloride in an electrolytic cell.[3] It would be almost 70 years before the photoelectric effect, which provides the fundamental basis for the photovoltaic process, was described by Einstein in 1905.[4] The flurry of photophysics and semiconductor research during the first half of the twentieth century resulted in robust fundamental descriptions of idealized solid state optoelectronic processes, including photogenerated current in a *p-n* junction. It was during this period

that researchers first tested PV materials such as CdSe and CuO;[3] and by the 1950s this early work, coupled to improvements in growing pure crystalline materials that approached the idealized models, led to the first silicon PV device at Bell Labs.[5]
In the 20 years that followed the work at Bell Labs, silicon solar cells were used sparingly for generation applications but widely for fundamental studies. Given the highly specialized applications, whether for power generation on satellites or physics studies in research labs, practical deployment issues such as longevity and cost were of little concern. Certainly there were scientists who saw PV as a potential commodity power source during this period, but there was little attention paid in terms of research funding until the US energy crisis of the 1970s. Regardless of the cause of this energy crisis, one by-product was the research community's shift to considering PV as a viable competitor to fossil fuel based energy production. Since that time PV research into different materials or systems has been measured in large part by its potential to become a long term replacement for fossil fuel sources. Unfortunately, adding the focus on applications to PV material research immediately highlights its challenges.

1.2.1 Challenges for PV adoption

From the perspective of fundamental science, the silicon solar cell is an exemplary system in that it matches the idealized behavior of a perfect system very closely. Many, if not most, solid state physics courses use silicon as the primary or sole example system to which fundamental processes and calculations are applied. Using silicon as a model system is due to the fact that silicon semiconductors can be manufactured very close to their idealized model including both the crystallinity and doping. The only downside to silicon is its cost which is the only appreciable challenge to PV adoption but a challenge that is not easily overcome.

When assessing a new energy technology one frequently finds claims as to the efficiency; how much energy out for how much energy in. Efficiency numbers are a good metric, but in the context of applied science they are only good within a specific system or class of materials. Comparing the efficiency of a coal/steam turbine to that of a solar cell is useless if trying to ascertain which is better for a specific application. The correct metric, for comparing energy production, is really the cost for which we

can produce or sell some unit of electricity. From a consumer perspective, the cost per kilowatt hour (kWh) is the important cost; frequently the cost to produce (in dollars invested per watt of production capacity) is used as well. In either case the efficiency is part of the overall equation, but not the only part; the cost to produce the system, ongoing maintenance cost, the lifetime of the system before replacement, etc. are also key components to placing a $/kWh value on any energy production system.[6] Figure 1.1 shows the cost per kilowatt hour for several different energy technologies, all of which are fully commercialized. In fact, PV is so expensive to produce that in order to keep up with the increase in power demand all silicon solar cells produced would have to be solely dedicated to the production of the next round of silicon solar cells.[7]

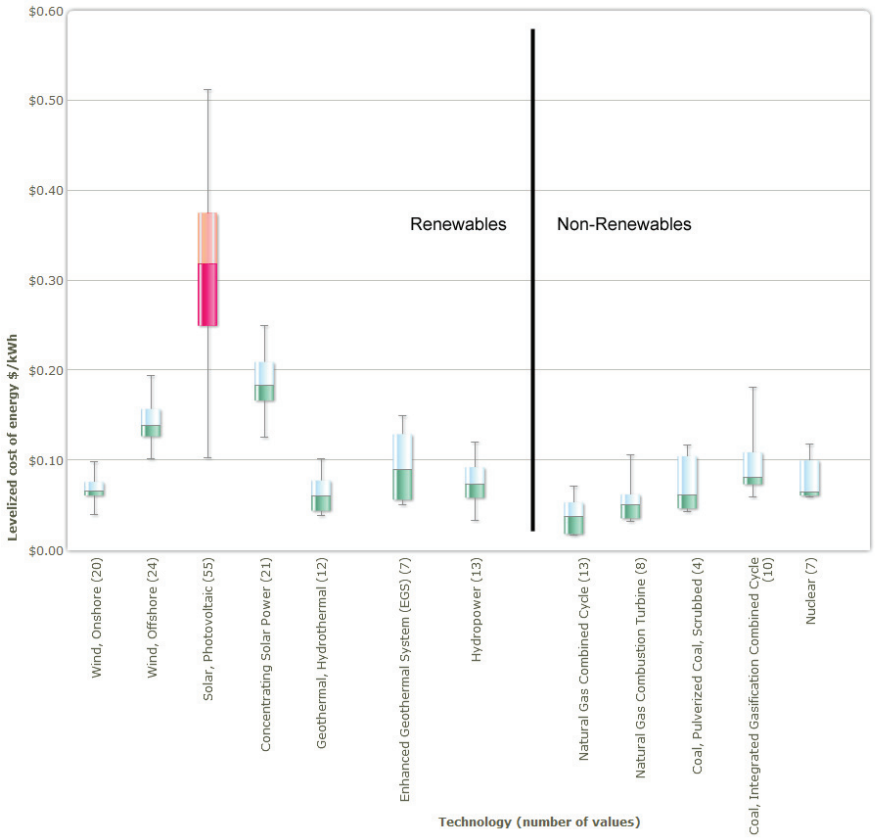

Figure 1.1: End user cost for electricity produced from different generation sources.[6]

Dr. Martin Green, from the University of New South Wales, expressed the cost/efficiency balance from the perspective of the cost to produce (rather than the cost

to purchase) and his results are shown in Figure 1.2.[8] The isocost lines (dashed lines originating at the origin) illustrate this balance visually; there is no specific efficiency that is required for a given cost target, the cost to produce the modules must also be considered. For perspective, the production cost for fossil fuel based power plants was approximately $1.00 per watt in 2000 with the current number being slightly lower due to improvements in natural gas technologies; at that point in time, silicon cells were approximately $3.00 per watt.[8] The plot also shows three regions for first, second and third generation solar, with silicon being firmly in the first generation region. Competitive PV requires, at a minimum, second generation technologies, and if PV is to supply a major portion of the global power demand, third generation technologies would have to be developed.

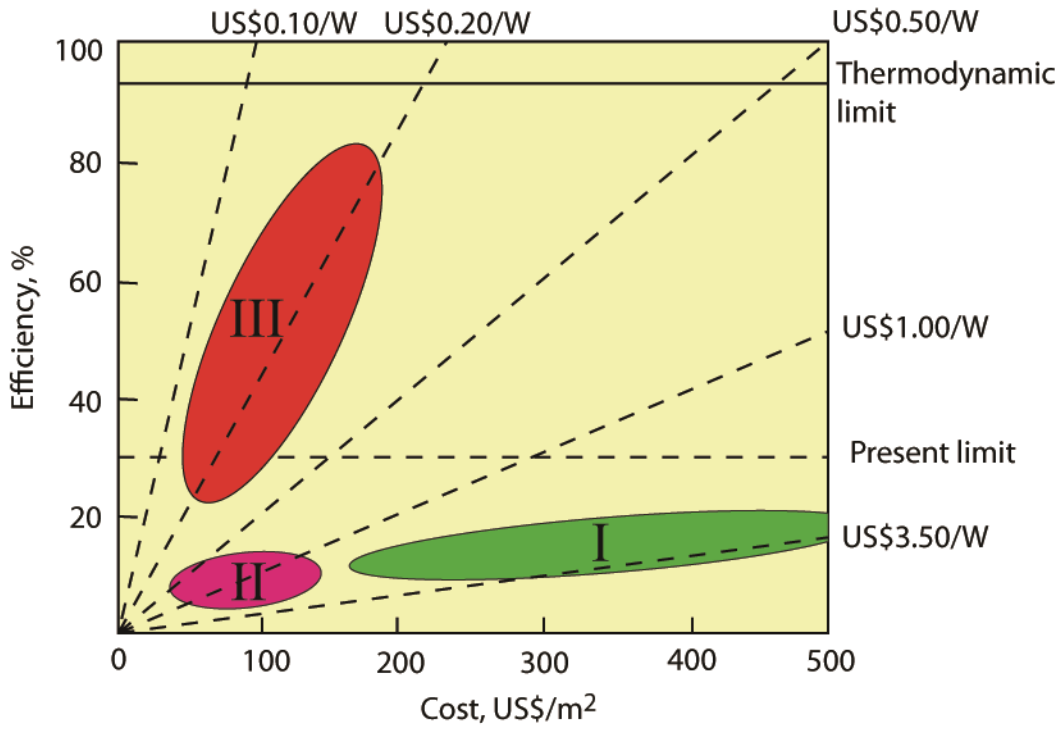

Figure 1.2: Production cost targets for first, second, and third generation PV technologies; the Present limit corresponds to the Shockley-Queisser (SQ) limit for single bandgap systems with one sun illumination. The abscissa is the cost to produce the raw solar modules, the isocost lines are the total power plant cost per watt of production capacity.[8]

1.2.2 Next Generation Materials

The progression from first to third generation technologies would consist of, generally speaking, two major steps. Initially, second generation PV would be much less expensive to produce but still be subject to the present limits. The move to third generation PV would require this same low cost processing while increasing the efficiency above the present limit. The present limit shown in Figure 1.2 is approximately 30% efficiency, the SQ limit, and was first calculated by Shockley and Queisser in 1961.[9] In this seminal work, Shockley and Queisser performed a detailed balance analysis of PV cells under the assumptions of a single bandgap and one sun illumination and determined the maximum efficiency that could be realized from a PV cell as a function of the bandgap of the absorbing material. These cost and efficiency targets set the context in which new PV technologies must be considered:

- Low cost processing: solution based, high throughput, at or near ambient temperatures and pressures
- High efficiency: technologies capable of breaking one or more of the assumptions of the SQ limit

Materials or technologies for next generation PV must satisfy at least one of these two key factors and, hopefully, both. This requirement is, in a very general sense, the reason behind the seemingly slow progress of PV science; high efficiencies and low cost processing have proven, so far, to be mutually exclusive. Figure 1.3 is the current chart of record efficiencies with all concentrator cells removed. There are 18 different technologies tracked by the National Renewable Energy Lab (NREL) of which 5 have never been considered good candidates for broad, terrestrial deployment principally due to cost issues; these are also the top 5 performers in terms of efficiency. The next three highest efficiencies are for Si variants and require single crystals, explaining the 85% market share for silicon PV. The remaining 10 are polycrystalline or amorphous materials that are processed at lower cost but with a maximum efficiency of 20.8% for copper indium gallium selenide (CIGS); it should be noted that both CIGS and CdTe (20.4%) are well commercialized. These facts demonstrate the difficulty of changing this cost/efficiency balance and that one key challenge is the

ability to make single crystals at low cost. In fact, the inability to make single crystals of semiconducting materials, which can be accurately and precisely infiltrated with dopant atoms, mandates a fundamentally different architecture for PV devices.

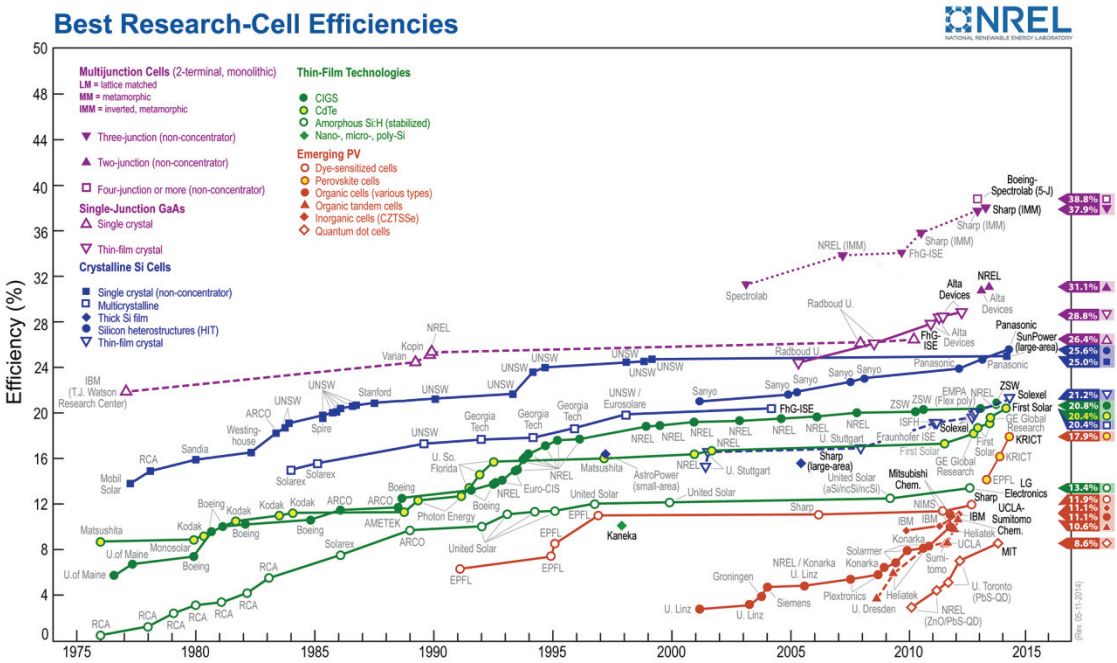

Figure 1.3: NREL efficiency chart for PV technologies (June 2014), all concentrator cell technologies have been removed for clarity.[2]

1.3 Device architecture and photophysics of PIN materials

There are several advantages to using single crystal materials for PV applications. For both Si and GaAs, the active layers in a device consist of only one material that has been infused with dopant atoms to create n-type and p-type regions. These are extrinsically doped semiconductors and the interface, or p-n junction, if made correctly, poses a negligible energy barrier to charge transport as the p and n regions are perfectly matched in both their material and their lattice spacing. The ~5% differential between the best single crystal device efficiencies and those made from polycrystalline or amorphous materials is due, in large part, to the energetics between two disparate materials. These energetics include the energy states formed due to the interface, which can lead to trap states, as well as the band alignments which must be optimal to avoid potential losses in the transferred carriers.

Because low cost processing and single crystals have, so far, been mutually exclusive, devices targeted at 2nd or 3rd generation technologies have taken on a fundamentally different device architecture, the p-type:intrinsic:n-type (PIN) junction as shown in Figure 1.4B. For both architectures shown in Figure 1.4 the extracting contacts are, essentially, the same. Though the actual material used can differ depending on the alignment of the contact's Fermi level with that of the active layer, the necessity and role of the contact is unchanged; therefore, we exclude the contacts from additional discussion. In typical, single crystal PV, as shown in Figure 1.4A, the balance of the device is comprised of a single material, e.g. doped silicon. The requirement for a working device is that the material be doped n-type on one side of the junction and p-type on the other. Since dopant concentrations tend to be on the order of 1-3 atomic %, this has only a small effect on the surface states or lattice parameters between the two regions. A very common manufacturing technique for Si PV is the diffusion of n-type atoms into one side of an already p-type wafer, this means that there is no discernable material interface although there is an electrical junction created. When produced in this fashion the interfacial energy of the p-n junction is negligible; typically, forming low loss interfaces in single or multi crystalline materials is relatively straightforward. In contrast, a PIN, or heterojunction, device consists of 3 different materials: a p-type extracting layer, an intrinsically doped absorber layer, and an n-type extracting layer. This PIN architecture introduces 2 interfaces between disparate materials that, more often than not, have mismatched lattice constants and different constituent atoms. Because the materials and the lattice spacing tend to be different, the interfacial energy can be high and forming low loss junctions is, in this case, a major issue that must be solved.

A second major component of the PIN device is the energy alignment of the conduction (CB) and valence bands (VB) of the different layers (CB and VB used generally to include other systems, e.g. quantum confined systems). An ideal alignment is demonstrated in Figure 1.4D for a PIN junction where the change in Gibbs free energy for the charge transfer ($\Delta G_{\text{transfer}}$) is both minimized and of the correct sign at all interfaces. Any misalignment of these energy levels causes a

reduction in the electron/hole potential resulting in a lower open circuit voltage (V_{oc}) and reduced efficiency.

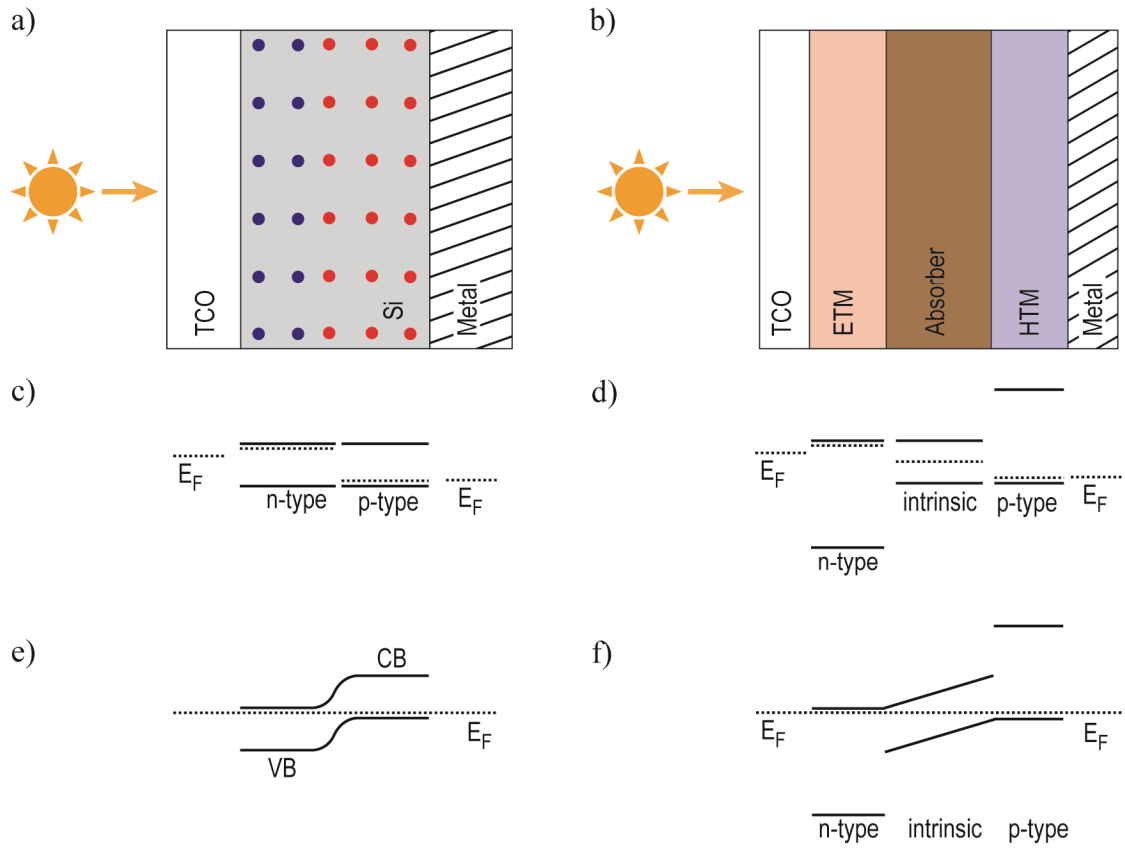

Figure 1.4: Schematic device stack and energy band alignments in PN and PIN type solar cells. Energy alignment is shown both before and after contact is made between layers for (a,c,e) *PN* homojunction and (b,d,f) *PIN* heterojunction. (a) blue dots are n-type dopant atoms and red dots are p-type dopant atoms, (b) ETM and HTM are electron and hole transport materials respectively. Dotted lines in c-f, marked E_F, are the Fermi levels, and VB and CB note the valence and conduction bands respectively. Band offsets and gradient in (f) assume and abrupt junction and a homogeneous electric field.

These two critical issues, interfaces and energy alignment, drive much of PV research into next generation technologies. In addition to the engineering challenge presented by these issues, each of the materials used for the PIN layers must perform its function as close to ideally as possible. As an example, the SQ limit is based on a very specific, highly idealized absorption profile; it is a step function for which there is no absorption below the bandgap and complete absorption above it. This specific issue was explored, briefly, and is included here as the conclusions reached (Chapter 2) cause consideration of a different paradigm regarding the use of nanocrystal

quantum dots (NCQD) in PV devices. One potential use for NCQD is in combination with different absorbing materials, such as the organic-inorganic lead halide perovskites, which is the primary work of this dissertation.

1.3.1 Ideality of the absorbing layer

NCQD systems appear on the NREL chart, and have, over the last several years showed good improvement in their efficiency. The interest in NCQD is due to several interesting properties, one of which is a tunable bandgap that allows specific engineering of the energy alignment through very simple synthetic paths. The size tunability of NCQD is frequently demonstrated with the plot shown in Figure 1.5 where we clearly see a shift in the bandgap as a function of crystal size;[10] however, what is also noticeable in these absorption spectra is a prominent excitonic peak at the primary excitation energy.

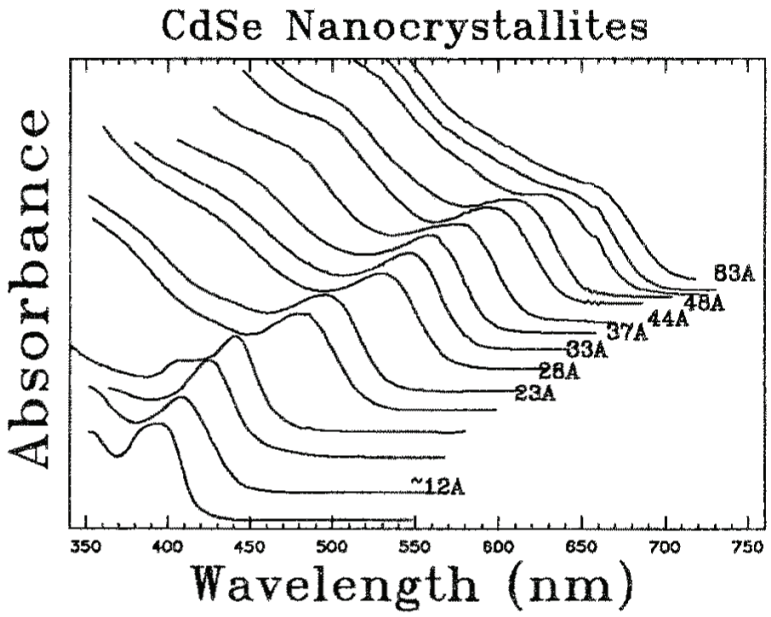

Figure 1.5: Absorption spectra for different size nanocrystals, trace labels are the nominal dot size in Angstroms, from reference 10. The excitonic peak can be seen to shift from ~410 nm to ~660 nm for nanocrystals of 12 Å and 83Å respectively.

This excitonic peak in NCQD is a far deviation from the idealized SQ step function. Chapter 2 of this dissertation details a study of the impact of the shape of the absorption profile on the maximum theoretical efficiency of an NCQD PV cell. One

result from this work is the realization that the maximum efficiency of ~25%, using currently available synthesis and manufacturing techniques, would make it difficult for NCQD to be a good absorber layer for 2nd generation PV. The low maximum possible efficiency does not discount an important role for NCQD, however, that role may be 3rd generation PV or as a transport material. As a transport material the tunability of the energy levels would still allow good engineering of the energy landscape. For NCQD to be applied in this manner, a different absorber material would be necessary. In general, a good absorber would have an absorption edge between 0.9 and 1.6 eV, a step-like absorption profile (particularly below the onset energy), good carrier concentration and mobility, and be solution processable at or near ambient conditions.

1.4 Methylammonium lead halide perovskites

In 2012, Snaith, et. al., reported a solar cell with greater than 10% efficiency in a dye sensitized solar cell (DSSC) configuration but using methylammonium lead trihalide ($MAPbX_3$) as the sensitizer;[11] their publication in Science was a turning point in the PV community's perception of the halide perovskites as a potential PV material. The novelty of their work, however, was not the development of $(MA)PbX_3$ as a new optoelectronic material; that work had been done much earlier. The perovskite structure is a crystal structure named for Lev Perovski, a Russian mineralogist, that was first applied to calcium titanate in the early 20th century. It is a very common structure with a generic formula unit of ABX_3 where A and B are two different cations and X is an anion. The conventional perovskite unit cell is shown in Figure 1.6A, which highlights several features of the structure. The B site cation, typically the smaller of the two, sits in the body center and is octahedrally coordinated to the face-centered X atoms; the larger A site cation occupying the gaps between the octahedra. Most perovskites found in nature are binary metal oxides with both A and B cations being some metal and the X atom being oxygen; $CaTiO_3$, $LaGaO_3$, etc. However, as a general class the perovskites do not require the anion to be oxygen and halide based perovskite structures have been synthesized for some time.

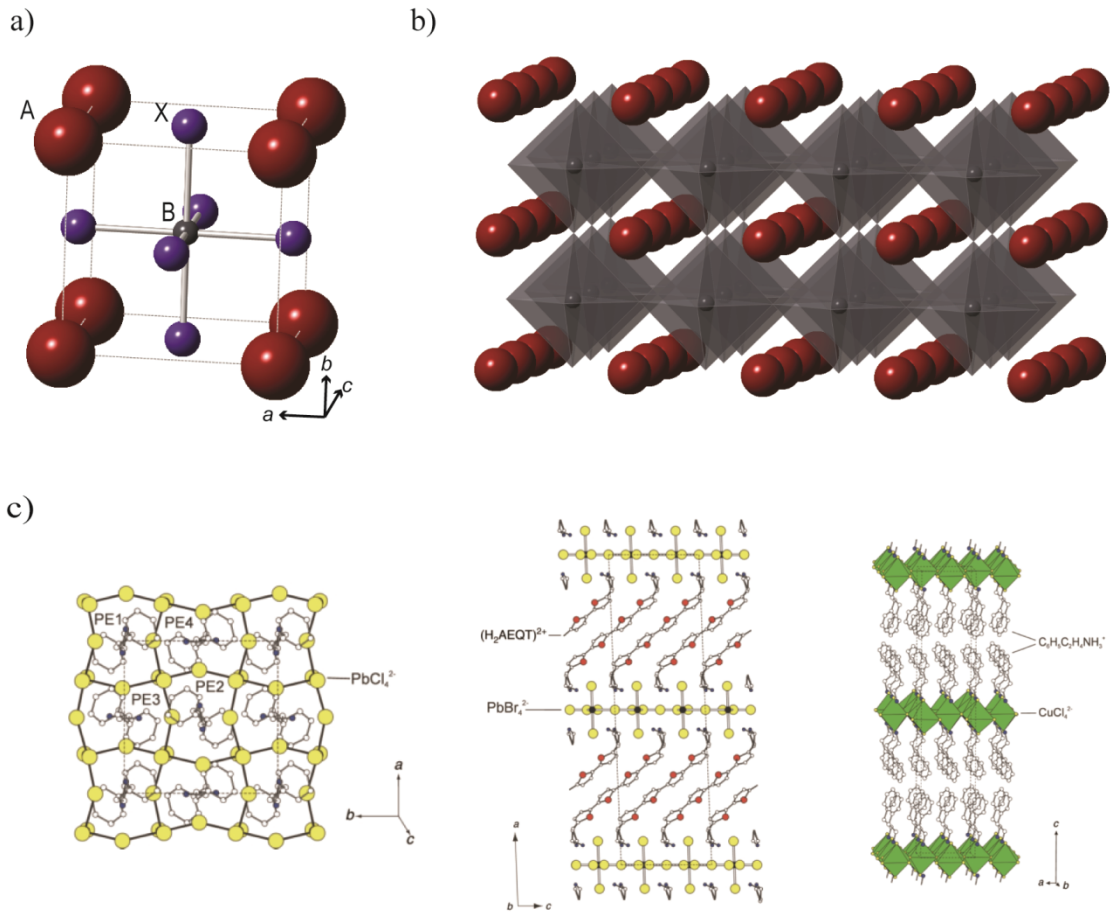

Figure 1.6: Perovskite structures with various representations and variations. (a) Conventional cubic perovskite unit cell with A sites at the corners, B site body centered and face centered X sites, sticks show the octahedral coordination of the B site cation. (b) Extended structure showing the sheet-like nature with alternating octahedral sheets, including the B cation and equatorial anions, and rock salt sheets, including the A cation and apical anions. (c) Various halide perovskite structures from reference 21 including layered structures in which the apical positions of the octahedra are disjoined by use of a large organic moiety on the A site.

As early as the late 1970s there are published investigations of both the crystallographic and electronic properties of halide based perovskites;[12] the initial studies used cesium as the A cation and the structures were typically of the 2D perovskite sheets.[13] In 1987, Poglitsch and Weber published a crystallographic and spectroscopic work on the 3D organic halide perovskites including $(MA)PbX_3$.[14] In the following decade several researchers, most notably David Mitzi at IBM, explored the chemical and structural aspects of these materials.[15-20] The initial interest in the halide perovskites was due to the inclusion of an organic moiety as the A site cation. By changing the size and shape of the organic moiety, a large variety of perovskite

structures, including analogs to the Ruddleston-Popper and Dion-Jacobson structures, could be formed as shown in Figure 1.6C.[21] There was little electronic characterization done during this period although a few papers were published with data from working electronic devices.[22-24]

During this same period of time, the efficiency of DSSC devices was stagnant at ~ 11%. One of the principal limitations for DSSC was the sensitizer which typically was an organic dye. These two areas of study converged in 2009 when Kojima and co-workers first reported a 3.8% efficient DSSC using $MAPbI_3$ as the sensitizer.[25] Two years later NG Park's group made 6.5% efficient cells and one year later, in 2012, improved that number to 9%;[26,27] this was the same year of Snaith's report of a 10% cell. This rapid improved showed that the organic-inorganic halide perovskites not only fit the general criteria in theory, they also demonstrated incredible results as a PV material in practice.

1.4.1 (MA)PbX_3 for PV applications

As a PV material (MA)PbX_3, and specifically the iodide version, fits the criteria discussed above quite well. At 1.6 eV bandgap the maximum theoretical efficiency is still greater than 30% with an extinction length, in the region of the solar spectrum, of less than one micron, which allows for thin films to be used.[28] Additionally, (MA)PbX_3 can be made via a variety of processing pathways (see Chapter 5) the most common of which is a one-step, solution-based deposition at or near ambient conditions.[29-40]

Technically there are two issues mentioned above that are critical for next generation materials, interfaces and energetics. The energetics of (MA)PbI_3 are well suited for PV with CB and VB edges that align well with HTM and ETM that are commonly used;[41] reports of these include TiO_2, ZnO, Spiro-OMeTAD, P3HT, Pedot:PSS, and NiO.[11,25,31-33,40-48] It is probable that some of the future increases in efficiency will be due to better engineering of the energy landscape, particularly the transport materials. Although investigation of the energetics is not the subject of this work, it is noteworthy that one advantage of the halide perovskites is that the energy

levels of the absorber can also be engineered through changes to the organic moiety or partial substitution of the metal cation.[49-51]

The second major issue discussed is the interface formed between the absorbing layer and the transport materials; this is the issue most likely to be affected by the work presented here. Generally speaking the goal is to create continuous, homogeneous interfaces that create no available trap states and pose no substantial barrier to charge transfer. There are many factors that need to be considered to accomplish this goal but certainly one requirement for any crystalline semiconductor is controlled crystal growth. A homogeneous interface, both crystallographically and energetically, would require large crystal grains with a common orientation. The importance of the grain size and orientation depend on the extent to which grain boundaries inhibit transport and the surface energies of the different facets. For the halide perovskites these two properties are not well known, however, several articles have pointed to the importance of crystal growth due to observed behavior.[36,44,52]

Accordingly, the principle work presented in this dissertation is intended to elucidate the crystallization dynamics for the halide perovskites. Controlling the crystal growth to express both crystal and film morphology that closely resembles ideality must begin with understanding the fundamental processes and mechanisms by which growth occurs. For materials scientists this fundamental understanding of how a material forms and grows is paramount in properly defining and controlling processing-structure relationships.

1.5 Processing-Structure relationships

The first step in the classic Processing-Structure-Properties triangle that is the mantra of materials scientists is the processing-structure relationships. The order of this listing is not meant to imply a serial approach to understanding, in fact process-property correlations are frequently found in the course of studying a new material system, including the halide perovskites. However, until the processing-structure relationships are established and understood at some fundamental level these correlations will always be observational in nature. Further, without a good

understanding of the effects of processing on the structure, a systematic study of the structure-property relationships is difficult if not impossible.

The fundamental aspects of the processing-structure relationships, in the case of crystalline materials, are found in the science of crystallization. The ultimate level of structure control would be the ability to grow crystals in specific directions, with specific orientations, of a specific size, i.e. knowing the mechanisms, kinetics, and energetics of the crystallization. The mechanisms by which the many processes involved in crystallization occur are far too vast to discuss in the current context. Suffice it to say that the study of crystallization has a long history and it covers an incredible range of knowledge from very general fundamental descriptions to highly specific mechanistic and mathematical descriptions of crystallization processes. Since this dissertation is not intended to serve as a text on crystallization, the discussion here will be limited to those areas of both general and specific theory and models that are directly applicable to the halide perovskites.

1.5.1 Crystallization Theory and Models

For any material that undergoes a transition from, e.g. $A \rightarrow B$, where B is crystalline, there at least two processes that must occur; nucleation and growth. In fact, under classic crystal growth theory, the state of a material undergoing this transition is fully described by:

$$x \approx \int_0^t \dot{N} \left(\int_t^\tau v dt \right)^{d/m} d\tau \tag{1.1}$$

Where x is the fraction of the material transformed from A to B at any point in time, $\dot{N}$ is a function describing the nucleation rate and v is the growth velocity adjusted by d/m which is the geometric factor.[53] The important thing to note in Equation 1.1 is that the entire state of the film is described by the product of two functions: nucleation and growth; and 1.1 is generally true for solution-solid and solid-solid transformations. Unraveling the mechanisms by which crystals grow begins by separating these two processes and understanding for both of them the driving force (thermodynamics) and energy barriers (kinetics) that dictate their behavior.

The halide perovskites can be made through a variety of processing techniques and a few are discussed briefly in Chapter 5. However, the most common method is a one-step solution based process as it seems most adaptable to high throughput, low cost manufacturing techniques. In this case all reagent materials, a lead salt and an organic halide salt, are dissolved in a common solvent and deposited on a substrate; upon thermal annealing the perovskite forms. The first step is the nucleation of a crystalline phase in solution, which has been widely treated for both classic and non-classic nucleation modes. The driving force and energy barrier for classic solution growth of crystals are illustrated with the commonly used plots in Figure 1.7. Figure 1.7A shows the typical plot of critical radius and free energy; as individual atoms or clusters coalesce there is a critical size, at which we define the clusters as nuclei, and beyond which growth becomes energetically favorable. The free energy that corresponds to the critical radius is the energy barrier for the nucleation step while the driving force is supersaturation, generally taken as a function of $\Delta\mu/k_bT$. Supersaturation can be affected in several ways all of which result in forcing the system beyond the solubility point of the reagents required for the crystal. Figure 1.7B shows the impact of several key crystallization parameters as a function of supersaturation and highlights the need to control the driving force for nucleation in order to effect the final result. Although Figure 1.7B shows a correlation between supersaturation and both crystal size and growth rate, these effects do not tell us about the crystal morphology, i.e. the tract or habitus.

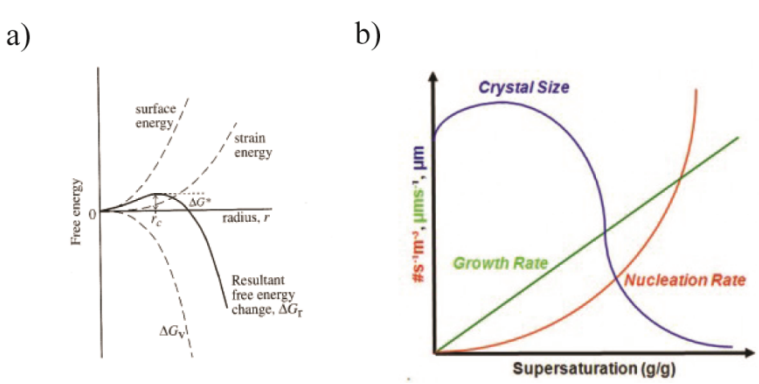

Figure 1.7: Energy barrier and driving force effects under classic crystal growth theory. (a) Changes in energy as a function of cluster size for the individual energy components (dashed lines) and total free

energy (solid line), with the critical radius and corresponding ΔG marked; (b) effect of the degrees of supersaturation on several key crystal growth metrics.[54]

In the limit of the entire crystal growing from a single nucleus, we would have a single crystal; in this way nucleation has some impact on the film morphology, however, this still would not determine the crystal morphology, the single crystal could be a 2D thin film or a 3D bulk crystal. The crystal morphology, although it may be limited by the nucleation, is a function of growth and coarsening (For the purpose of this discussion we will include grain growth, or coarsening, with the crystal growth). Many crystals that grow from solution do so in multiple steps, including the halide perovskites. Ostwald observed this in the late 19th century and described the "step rule" by which many crystals form by way of a metastable intermediate, i.e. $A \rightarrow B' \rightarrow B$ where B' is some intermediate material or phase. The reaction coordinate for such growth is, generally, shown in figure 1.8A and the energy barrier and driving force shown. The general driving force for crystallization is given as $\Delta\mu / k_b T$ where $\Delta\mu$ is the chemical potential difference between the species in the starting and ending states, k_b is Boltzmann's constant, and T is temperature. For nucleation this driving force can be directly equated to supersaturation (S) by $\ln S = \Delta\mu / k_b T$, for growth there is no analogous general descriptor but there are many established descriptors for specific growth modes. The important issue here is the driving force of the growth phase, as that has the largest impact on the crystal morphology. Figure 1.8B shows the change in the crystal morphology as a function of the magnitude of the driving force.

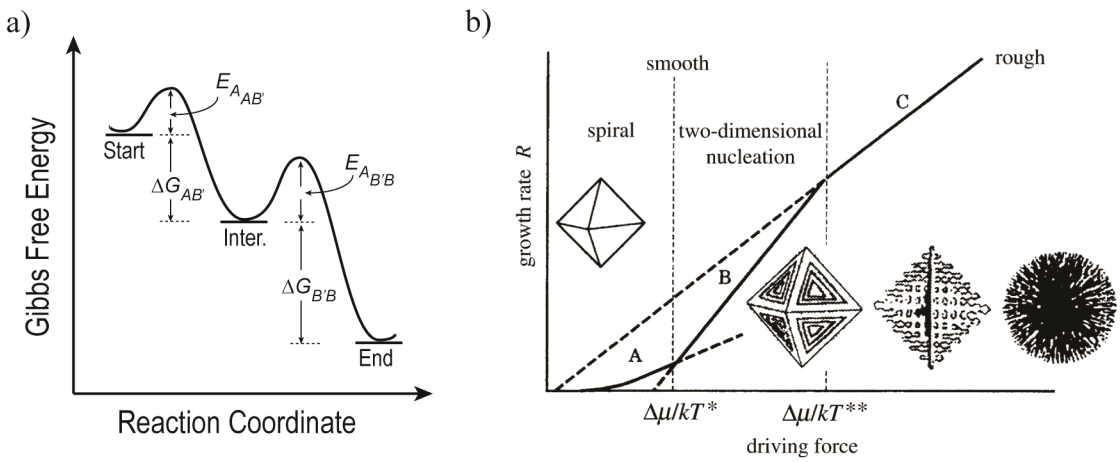

Figure 1.8: Driving forces and energy barriers for crystal growth.[54]

In order to have complete control of the crystal growth we have to consider the four parameters discussed above; the energy barrier and driving force for both the nucleation and the growth. If we take the example of thin film growth from solution, the balance of the different parameters becomes apparent. Typically, thin film morphology is improved with high nucleation rates. Because the length scale involved in nucleation is so much smaller than the area of typical thin films, low nucleation rates can lead to large macroscopic variations in the density of nuclei. Additionally, the time difference between the first and last nucleus formed is increased with lower nucleation rates which leads to large deviations from the median grain size. To encourage nucleation everywhere and move as quickly from nucleation to growth, we would increase the temperature to evaporate solvent faster and move to a high driving force for nucleation. The result on the growth phase is that the higher temperature would also provide a stronger driving force for growth; this would lead to crystal morphologies further from the equilibrium shape.

In the case of the halide perovskites the above discussion is generally applicable. As a result, controlling the final film and crystal morphology requires a way in which manipulating the nucleation and growth can be decoupled from each other. The rate equation for a first order reaction where $A \rightarrow B$ can be written as:

$$Rate = k\frac{a_B}{a_A} = k_0 e^{-E_A/RT}\left(\frac{a_B}{a_A}\right) = k_0 e^{-E_A/RT}\left(\frac{f(\mu_B)}{f(\mu_A)}\right) \quad (1.2)$$

where the activity has been left as a function of μ for clarity (the function is known). Equation 1.2 is included to show that the rate is the experimental variable where kinetics, E_A, and thermodynamics, μ, converge. As such, we can approach morphology control by controlling the rates of nucleation and growth independently without concern for which term on the right hand side of Equation 1.2 we are manipulating. For the halide perovskites the control of nucleation and growth, independent of each other, has not been well studied. The purpose of the work presented in this dissertation is to elucidate these issues for this material system and to demonstrate an ability to affect them.

1.6 Processing-Structure Relationships for (MA)PbX$_3$

One of the primary tools used to discern the structural evolution for (MA)PbX$_3$ in this work was wide angle X-ray scattering (WAXS). A combination of in-situ and ex-situ data were taken on a variety of films while altering such processing parameters as spin speed, solution concentration, ambient concentrations of oxygen and water, annealing temperature, and substrate material. The initial results revealed, amongst other things, the existence of a solid, crystalline material prior to the formation of the perovskite, i.e. (MA)PbX$_3$ follows Ostwald's step rule. The fact that there exists some precursor structure, that transforms to the perovskite, defines the transition of primary interest as a solid state transformation.

Knowledge of the type of transition gives us a starting state and general idea of the starting structure; the ending state and structure are well known. With this information, fundamental questions such as what is the movement of each atom between the start and end states and what is the energy cost for that movement, can be translated to experimental investigations. The scope of possible explorations that stem from these fundamental questions are far too many to consider in the course of this dissertation, so the list of questions, for which the answers are contained in Chapters 3-5, was limited to the following:

I. Observationally: What effect do the thermal annealing conditions have on film or crystal morphology?

II. Mechanistically: Are the reagent salts completely dissociated during the transition or is there some topotactic rearrangement of the reagent salt(s)?

III. Fundamentally: Can we extract quantitative kinetics data for the transition and how are those parameters affected by processing conditions?

In Chapter 3 of this dissertation we probed the effect of annealing conditions on spuncast thin films. The temperature conditions were chosen for study as preliminary work showed the strongest effect on film and crystal morphology was due to temperature. Appendix A contains data for the effect of substrate material as that also has a strong effect. The primary result here is that careful control of the temperature results in better film morphology and, in certain cases, better crystal morphology. The effect of better film and crystal morphology was explored in a collaboration with the Snaith group and found to result in better device performance in planar devices.[36]

Probing the mechanism of the transformation is a difficult and long task, and there are many systems that have been broadly studied for decades for which this understanding does not exist. The purpose of the work presented in Chapter 4 was not to attempt a complete understanding of the mechanisms, but to probe one specific question. There have been other ionic systems for which one or more of the reagents undergoes some topotactic rearrangement, rather than a complete dissociation. By altering the processing path, such that one or both of the reagent salts for $(MA)PbX_3$ were in the solid state, we were able to probe for topotacticity and found instead that all salts are completely dissociated.

The final chapter of this work is a kinetic study of the precursor-perovskite transition, including extraction of the activation energy. The approach here was a widely used technique whereby a property is tracked in time to determine the amount of material in the final state; this is done for multiple temperatures as well as several different systems. Chapter 5 discusses the details and provides the primary results. In addition to kinetic parameters, the information derived allowed for the determination

of a general formula for the precursor material; something previously unknown. Although we still do not know the exact structure of the precursor, knowing the general formula allows for manipulation of the system.

1.7 Structure-Property Relationships

Structure-property relationships are not explored widely in this work, although the work presented here is directly used and demonstrated in collaborative works. As mentioned above, the enhanced device properties associated with a better textured film are discussed in reference 36. That article, which details the effect of a high temperature flash anneal protocol, completes one processing-structure-properties loop with: 130 °C flash anneal→higher orientational order→improved device performance. Similarly, the work presented in both Chapters 4 and 5 led to the use of non-halide lead salts as a reagent, the impact of which was explored by another collaborator. Appendix B is the result of that collaboration in which the impact of affecting the crystallization through chemistry (rather than temperature) is shown; this processing change causes much smoother films with complete coverage which leads to improved device performance. These are only two examples of the application of the results presented here but they both demonstrate the ability to: (a) manipulate the structure, and (b) correlate that to functional properties. Additional work on both manipulating the structure and understanding the associated property changes is discussed in Section 1.8.

1.8 Future Work

The goal of the work presented here is, ultimately, to control the film and crystal morphology to generate thin films with precise control. There are two probable paths to doing this: (a) control the solution-precursor growth as the precursor material templates the final film, or (b) bypass the precursor and control the solution-perovskite growth. Recent work, which is presented in Appendix C, explores the possibility of using ionic liquids as a reaction medium which causes very good film morphology while crystallizing directly to the perovskite. Mediating the crystallization kinetics by direct formation of the perovskite, changes to the lead salt reagent, or additives to the

solution chemistry have all been demonstrated.[34,55] These types of experimental approaches are already showing an impact in the ability to control crystal growth. Future work will most certainly improve the crystal and film growth by coupling these observational effects to a better understanding of the mechanisms by which the precursor or perovskite structures form.

1.9 References

1. Edenhofer, Ottmar, Ramón Pichs Madruga, and Y Sokona. Renewable Energy Sources and Climate Change Mitigation: Special Report of the Intergovernmental Panel On Climate Change. *New York, Cambridge University Press* (2012).

2. NREL Best Research Cell Efficiencies. (2014, September). Retrieved October 13, 2014, from http://www.nrel.gov/ncpv/images/efficiency_chart.jpg

3. The History of Solar. (n.d.). Retrieved October 13, 2014, from https://www1.eere.energy.gov/solar/pdfs/solar_timeline.pdf

4. Einstein, A. Generation and conversion of light with regard to a heuristic point of view. *ANNALEN DER PHYSIK*. **17**, 132-148 (1905)

5. Chapin, D.M., Fuller, C.S., Pearson, G.L. A New Silicon P-N Junction Photocell for Converting Solar Radiation Into Electrical Power, *J. Appl. Phys.*, **25**, 676-677 (1954)

6. Dept. of Energy Transparent Cost Database. (n.d.) Retrieved October 13, 2014, from http://en.openei.org/apps/TCDB/

7. Schneider, D. Solar Energy's Red Queen, (2008). Retrieved October 13, 2014, from http://www.americanscientist.org/issues/pub/2008/1/solar-energys-red-queen

8. Green, M. A. Third generation photovoltaics: advanced solar energy conversion. *Berlin, Springer* (2006).

9. Shockley, W. & Queisser, H. J. Detailed Balance Limit of Efficiency of p-n Junction Solar Cells. *J. Appl. Phys.* **32,** 510 (1961).

10. Murray, C., Nirmal, M. & Norris, D. J. Synthesis and Structural Characterization of II-VI Semiconductor Nanocrystallites (Quantum Dots). *Z. Phys. D.* **26,** S 231–233 (1993).

11. Lee, M. M., Teuscher, J., Miyasaka, T., Murakami, T. N. & Snaith, H. J. Efficient hybrid solar cells based on meso-superstructured organometal halide perovskites. *Science* **338,** 643–7 (2012).

12. Ledsham, R. C. & Day, P. Solid-state photo-polymerization of unsaturated organic cations in layer perovskite halide salts. *J. Chem. Soc. Chem. Commun.* 921 (1981). doi:10.1039/c39810000921

13. Mizusaki, J., Arai, K. & Fueki, K. Ionic conduction of the perovskite-type halides. *Solid State Ionics* **11,** 203–211 (1983).

14. Poglitsch, A. & Weber, D. Dynamic disorder in methylammoniumtrihalogenoplumbates (II) observed by millimeter-wave spectroscopy. *J. Chem. Phys.* **87,** 6373–6378 (1987).

15. Mitzi, D. B., Feild, C. A., Harrison, W. T. A. & Guloy, A. M. Conducting tin halides with a layered organic-based perovskite structure. *Nature* **369,** 467–469 (1994).

16. Wang, S., Mitzi, D. B., Feild, C. A. & Guloys, A. Synthesis and Characterization of $[NH_2C(I)=NH_2]_3MI_5$ (M = Sn, Pb): Stereochemical Activity in Divalent Tin and Lead Halides Containing Single (110) Perovskite Sheets. *J. Chem. Soc.* **117,** 5297–5302 (1995).

17. Wang, S., Mitzi, D. B., Landrum, G. A., Genin, H. & Hoffmann, R. Synthesis and Solid State Chemistry of CH 3 BiI 2 : A Structure with an Extended One-Dimensional Organometallic Framework. *J. Am. Chem. Soc.* **119,** 724–732 (1997).

18. Mitzi, D. B., Liang, K. N. & Wang, S. M. Synthesis and characterization of $[NH_2C(I)=NH_2]_2ASnI_5$ with A = iodoformamidinium or formamidinium: The chemistry of cyanamide and tin(II) iodide in concentrated aqueous hydriodic acid solutions. *Inorg. Chem.* **37,** 321–327 (1998).

19. Liang, K., Mitzi, D. B. & Prikas, M. Synthesis and characterization of organic-inorganic perovskite thin films prepared using a versatile two-step dipping technique. *Chem. Mater.* **10,** 403–411 (1998).

20. Knutson, J. L., Martin, J. D. & Mitzi, D. B. Tuning the band gap in hybrid tin iodide perovskite semiconductors using structural templating. *Inorg. Chem.* **44,** 4699–4705 (2005).

21. Mitzi, D. B. Templating and structural engineering in organic–inorganic perovskites. *J. Chem. Soc. Dalt. Trans.* 1–12 (2001). doi:10.1039/b007070j

22. Hattori, T., Taira, T., Era, M., Tsutsui, T. & Saito, S. Highly efficient electroluminescence from a heterostructure device combined with emissive layered-perovskite and an electron-transporting organic compound. *Chem. Phys. Lett.* **254,** 103–108 (1996).

23. Mitzi, D. B., Kosbar, L. L., Murray, C. E., Copel, M. & Afzali, A. High-mobility ultrathin semiconducting films prepared by spin coating. *Nature* **428,** 299–303 (2004).

24. Matsushima, T., Fujita, K. & Tsutsui, T. High field-effect hole mobility in organic-inorganic hybrid thin films prepared by vacuum vapor deposition technique. *Japanese J. Appl. Phys.Pt. 2* **43,** L1199–L1201 (2004).

25. Kojima, A., Teshima, K., Shirai, Y. & Miyasaka, T. Organometal halide perovskites as visible-light sensitizers for photovoltaic cells. *J. Am. Chem. Soc.* **131,** 6050–1 (2009).

26. Im, J.-H., Lee, C.-R., Lee, J.-W., Park, S.-W. & Park, N.-G. 6.5% Efficient Perovskite Quantum-Dot-Sensitized Solar Cell. *Nanoscale* **3,** 4088–93 (2011).

27. Kim, H.-S. *et al.* Lead iodide perovskite sensitized all-solid-state submicron thin film mesoscopic solar cell with efficiency exceeding 9%. *Sci. Rep.* **2,** 591 (2012).

28. Xing, G. *et al.* Long-Range Balanced Electron- and Hole-Transport Lengths in Organic-Inorganic $CH_3NH_3PbI_3$. *Science* **342,** 344–347 (2013).

29. Noh, J. H., Im, S. H., Heo, J. H., Mandal, T. N. & Seok, S. Il. Chemical management for colorful, efficient, and stable inorganic-organic hybrid nanostructured solar cells. *Nano Lett.* **13,** 1764–9 (2013).

30. Etgar, L. *et al.* Mesoscopic $CH_3NH_3PbI_3/TiO_2$ heterojunction solar cells. *J. Am. Chem. Soc.* **134,** 17396–9 (2012).

31. Liu, D. & Kelly, T. L. Perovskite solar cells with a planar heterojunction structure prepared using room-temperature solution processing techniques. *Nat. Photonics* **8,** 133–138 (2013).

32. Abrusci, A. *et al.* High-performance perovskite-polymer hybrid solar cells via electronic coupling with fullerene monolayers. *Nano Lett.* **13,** 3124–8 (2013).

33. You, J. *et al.* Low-temperature solution-processed perovskite solar cells with high efficiency and flexibility. *ACS Nano* **8,** 1674–80 (2014).

34. Liang, P.-W. *et al.* Additive Enhanced Crystallization of Solution-Processed Perovskite for Highly Efficient Planar-Heterojunction Solar Cells. *Adv. Mater.* **26,** 3748–3754 (2014).

35. Dualeh, A. *et al.* Impedance spectroscopic analysis of lead iodide perovskite-sensitized solid-state solar cells. *ACS Nano* **8,** 362–73 (2014).

36. Saliba, M. *et al.* Influence of Thermal Processing Protocol upon the Crystallization and Photovoltaic Performance of Organic–Inorganic Lead Trihalide Perovskites. *J. Phys. Chem. C* **118**, 17171-17177 (2014).

37. Eperon, G. E., Burlakov, V. M., Docampo, P., Goriely, A. & Snaith, H. J. Morphological Control for High Performance, Solution-Processed Planar Heterojunction Perovskite Solar Cells. *Adv. Funct. Mater.* **24**, 151-157 (2013).

38. Zhao, Y. & Zhu, K. CH_3NH_3Cl - Assisted One-Step Solution Growth of $CH_3NH_3PbI_3$: Structure, Charge-Carrier Dynamics, and Photovoltaic Properties of Perovskite Solar Cells. *J. Phys. Chem. C* **118,** 9412–9418 (2014).

39. Edri, E., Kirmayer, S., Kulbak, M., Hodes, G. & Cahen, D. Chloride Inclusion and Hole Transport Material Doping to Improve Methyl Ammonium Lead Bromide Perovskite-Based High Open-Circuit Voltage Solar Cells. *J. Phys. Chem. Lett.* **5,** 429–433 (2014).

40. Jeng, J.-Y. *et al.* Nickel Oxide Electrode Interlayer in $CH_3NH_3PbI_3$ Perovskite/PCBM Planar-Heterojunction Hybrid Solar Cells. *Adv. Mater.* **26,** 4107–4113 (2014).

41. Edri, E. *et al.* Elucidating the charge carrier separation and working mechanism of $CH_3NH_3PbI_{(3-x)}Cl_x$ perovskite solar cells. *Nat. Commun.* **5,** 3461 (2014).

42. Ball, J. M., Lee, M. M., Hey, A. & Snaith, H. J. Low-temperature processed meso-superstructured to thin-film perovskite solar cells. *Energy Environ. Sci.* **6,** 1739 (2013).

43. Bi, D., Yang, L. & Boschloo, G. Effect of different hole transport materials on recombination in $CH_3NH_3PbI_3$ perovskite-sensitized mesoscopic solar cells. *J. Phys. Chem. Lett.* **4**, 1532-1536 (2013).

44. Chen, Q. *et al.* Planar heterojunction perovskite solar cells via vapor-assisted solution process. *J. Am. Chem. Soc.* **136,** 622–5 (2014).

45. Ramos, F. J. *et al.* Perovskite solar cells based on nanocolumnar plasma-deposited ZnO thin films. *Chemphyschem* **15,** 1148–53 (2014).

46. Chung, I., Lee, B., He, J., Chang, R. P. H. & Kanatzidis, M. G. All-solid-state dye-sensitized solar cells with high efficiency. *Nature* **485,** 486–489 (2012).

47. Chiang, Y.-F. *et al.* High voltage and efficient bilayer heterojunction solar cells based on an organic-inorganic hybrid perovskite absorber with a low-cost flexible substrate. *Phys. Chem. Chem. Phys.* **16,** 6033–40 (2014).

48. Malinkiewicz, O. *et al.* Perovskite solar cells employing organic charge-transport layers. *Nat. Photonics* **8,** 128–132 (2013).

49. Eperon, G. E. *et al.* Formamidinium lead trihalide: a broadly tunable perovskite for efficient planar heterojunction solar cells. *Energy Environ. Sci.* **7,** 982 (2014).

50. Hao, F., Stoumpos, C. C., Chang, R. P. H. & Kanatzidis, M. G. Anomalous Band Gap Behavior in Mixed Sn and Pb Perovskites Enables Broadening of Absorption Spectrum in Solar Cells. *J. Am. Chem. Soc.* **136,** 8094–8099 (2014).

51. Ogomi, Y. *et al.* $CH_3NH_3Sn_xPb_{(1-x)}I_3$ Perovskite Solar Cells Covering up to 1060 nm. *J. Phys. Chem. Lett.* **5,** 1004–1011 (2014).

52. Bretschneider, S. a., Weickert, J., Dorman, J. a. & Schmidt-Mende, L. Research Update: Physical and electrical characteristics of lead halide perovskites for solar cell applications. *APL Mater.* **2,** 040701 (2014).

53. Liu, F., Sommer, F. & Mittemeijer, E. J. Analysis of the kinetics of phase transformations; roles of nucleation index and temperature dependent site saturation, and recipes for the extraction of kinetic parameters. *J. Mater. Sci.* **42,** 573–587 (2006).

54. Sunagawa, I. *Crystals: Growth, Morphology and Perfection*. (Cambridge University Press, 2005).

55. Moore, D. T., Sai, H., Wee Tan, K., Estroff, L. a. & Wiesner, U. Impact of the organic halide salt on final perovskite composition for photovoltaic applications. *APL Mater.* **2,** 081802 (2014).

CHAPTER 2

A DETAILED BALANCE ANALYSIS OF CONVERSION EFFICIENCIES LIMITS FOR NANOCRYSTAL SOLAR CELLS – RELATING THE SHAPE OF THE EXCITONIC PEAK TO CONVERSION EFFICIENCIES

2.1 Abstract

We report the detailed balance analysis of the photovoltaic conversion efficiency of nanocrystal solar cells with discrete excitonic absorption profiles. We calculated the conversion efficiency limits of single junction, multiexciton, and tandem solar cells as a function of exciton peak energy and width. We delineate the width of the absorption spectrum in terms of the energetic width of an isolated nanocrystal and the physical width due to the nanocrystal diameter distribution in the ensemble. Our results suggest that the conversion efficiency is less strongly impacted by the ensemble distribution than by the energetic peak width.

2.2 Introduction

Substantial research efforts are currently directed toward the development of next-generation photovoltaic (PV) technologies that combine high conversion efficiency and low cost. Novel absorber materials, including organic dyes,[1,2] small molecules and polymers, polycrystalline thin films, [3,4] and colloidal nanocrystals (NCs) [5] have garnered attention by virtue of their ability to efficiently harvest light in thin films that can be prepared by low-cost methods. Semiconductor NCs are particularly attractive PV materials since their energy gap can be readily tailored through synthetic adjustment of the NC size and composition. Moreover, recent demonstrations of multiexciton generation (MEG)[6,7] and hot electron transfer[8] have captivated scientists and engineers as an opportunity to exploit these phenomena in third-generation PV.

The surge of interest in NC-based PV has led to significant advances in both our scientific understanding of basic photophysical processes in nanostructures and remarkable improvements in conversion efficiencies in prototype devices with confirmed NC PV record efficiencies reaching ~7-8%.[9] Much of the success in

advancing NC PV along this trajectory was based on describing and analyzing the performance of the NC absorber layers with principles adopted from conventional semiconductors. Specifically, concepts like band bending and carrier depletion width have provided important guidance in the initial design of the NC layer as a continuum. However, it is important to bear in mind that the electronic structure of NC films is significantly more complex due to the presence of myriad nanostructured interfaces between NCs. Quantum confinement effects give rise to unique optical and electrical properties and this motivates a deeper understanding of the impact of these effects on fundamental PV conversion efficiency limits. In this article, we illustrate how characteristic features of the NC absorption spectrum, in particular the shape of the first excitonic peak and the local minima between the first and second excitonic peak (valley), impact the theoretical PV conversion efficiency limits.

2.3 Results and Discussion

The detailed balance analysis of PV energy conversion in a single layer solar cell was first described by Shockley and Queisser in 1961.[10] The well-known Shockley-Queisser (SQ) limit assumes several important idealizations including: (i) an absorber material with a step-like absorption profile (*i.e.*, photons with an energy greater than the energy gap (E_g) are absorbed and generate an electron-hole pair with unity efficiency); $\alpha=1$ for $h\nu \geq E_g$ and $\alpha=0$ for $h\nu < E_g$, (ii) only radiative recombination of electron-hole pairs is considered while non-radiative recombination is neglected, and (iii) the current-voltage characteristics are governed by the diode equation with idealized shunt and series resistances. The detailed balance model does not account for charge transport limitations, which present a key contributor to the inefficiencies encountered in current NC PV cells.

The nature of the absorption profile and variations in the electronic structure of the photovoltaic materials can significantly impact conversion efficiency limits. Rau et al. have reported the theoretical PV conversion efficiency limits accounting for the absorption spectra and electronic structure in organic[11] and CIGS solar cells.[12] Rau and Werner also showed that fluctuations in the band-gap considerably degrade the achievable efficiency of solar cells in the radiative recombination limit.[13] To the best

of our knowledge, the relationship between conversion efficiency and the nature of the electronic structure of the NC film as revealed in the absorption profile, including the excitonic peak and valley, have not been previously investigated. A detailed discussion of the theoretical PV conversion efficiency as a function of the absorption model is given in the supporting information.

Figure 2.1a shows the typical excitonic absorption signature of semiconductor NC, which can, to a first approximation, be described as a Gaussian peak. Fundamentally, the electronic structure of semiconductor NCs is described by a series of discrete states, instead of a continuous density of states common to bulk materials.[14] Accordingly, the absorption of an idealized single NC would be a series of delta functions (Figure 2.1a, red solid lines), which is impractical for panchromatic light absorption in a solar cell. Fortunately, homogeneous and inhomogeneous broadening effects expand the absorption profile of NCs.

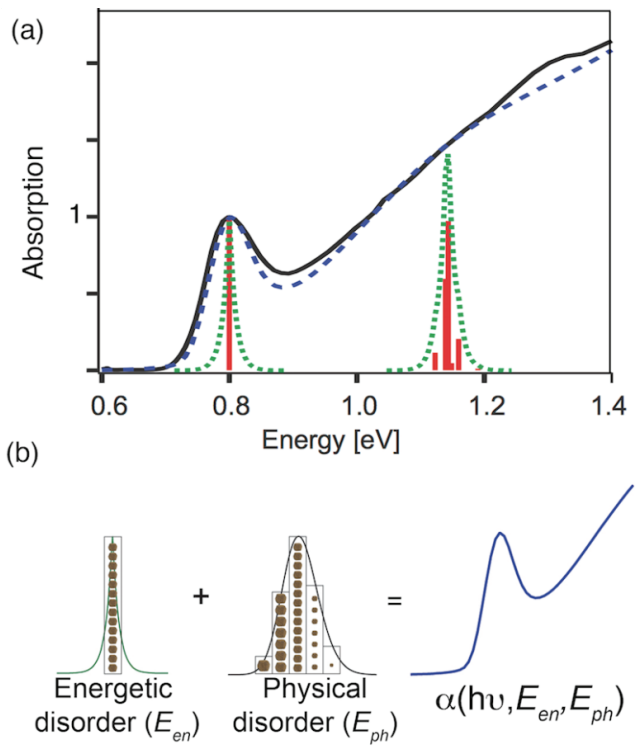

Figure 2.1: Model of the excitonic absorption spectrum of semiconductor NCs. (a) discrete transitions (red , solid), Urbach distributions (green, dot), complete absorption with Gaussian size distribution (blue, dash), experimental data for 0.8eV PbS NCs (black, solid); (b) Schematic illustration of the impact of energetic and physical disorder on the nature of the absorption spectrum.

To understand the origin of the peak width in context of physical properties of the NC film, we need to consider the width of a single particle (denoted here as energetic disorder, E_{en}) and contributions due to the NC diameter distribution in the ensemble (denoted as physical disorder E_{ph}). The interplay between physical and energetic disorder is schematically illustrated in Figure 2.1b. The origin of the line broadening has been explored by others both theoretically[15] and experimentally[16,17] and reported to be as small as 10meV and as large as 100meV. Despite the variation of reported magnitude of this disorder, the unifying factor in these studies is the exponential nature of the absorption tail. Accordingly, the energetic disorder, E_{en}, in our model is represented by an exponential distribution about each particle size [Fig 2.1a, green dashed lines].

The physical disorder in NCs is readily related to the statistical distribution of the NC diameter in the ensemble, which typically ranges from 5-15%; this represents, for example, a FWHM of 80meV for a 5% distribution centered at 1.4eV. Other systems can have physical disorder that affects their band gap, for example Rau et al. estimated separate energies for the physical and energetic disorder in CIGS but showed that in that system the physical disorder was much less then the energetic disorder.[12] In semiconductor NCs the opposite scenario appears to hold and the physical disorder can be an order of magnitude larger than E_{en} and, more importantly, is not an exponential distribution but a skewed Gaussian distribution with respect to energy. It should be noted that the Gaussian nature of the size distribution, and the fact that it overwhelms the disorder, explains why it is the choice for fitting experimental absorption spectra.

Taking the energetic and physical disorder into account leads to an expression for NC absorption of the form $\alpha(h\nu, E_{en}, E_{ph})$. For quantum-confined systems these effects must be applied at each discrete excitation energy. Our model is the sum of a series of exponential distributions that are normally distributed about each allowed excitation energy:

$$\alpha(h\nu, E_{en}, E_{ph}) = \sum_i \int_0^\infty A_i \exp\left(-\frac{(h\nu - E_i)^2}{E_{ph}^2}\right) \exp\left(-\frac{|h\nu - E|}{E_{en}}\right) dh\nu \tag{2.1}$$

where E_i is the ith transition, $h\nu$ is the photon energy and A_i is proportional to the oscillator strength. We use the 4-band approximation developed by Kang and Wise[18] to calculate the excitation energies and oscillator strengths for all transitions with $E_g < h\nu < 4.43$eV (the limit of the AM1.5G spectrum). Figure 2.1a compares the calculated absorption spectrum to experimental data. Only E_{en} and E_{ph} are used as fit parameters in our model. Fits to additional spectra are provided in the supporting information. For clarity, part of the analysis presented below combines energetic and physical disorder into a single energy width, W, which is determined by fitting a single Gaussian distribution to the first excitonic peak of the calculated spectrum. Additional details of the calculation of W and A_i and the comparison of modeled and experimental absorption spectra are provided in the supporting information.

Figure 2.2 illustrates the absorption spectra used in the detailed balance analysis and the corresponding theoretical conversion efficiency limits. The excitonic nature of the absorption profile significantly reduces the single junction conversion efficiency from the 33% SQ limit to 26%. The reduced conversion efficiency arises from two factors: (i) the partial transparency of the NC absorption spectrum between the first and second excitonic states and (ii) the presence of tail states below the excitonic peak. The valley reduces the photogenerated current while the 'tail' reduces the voltage of the PV cell. To determine the relative impact of the valley and the peak, we analyzed each aspect separately in detail below.

To study the impact of the valley in the excitonic absorption spectrum, we calculated the conversion efficiency for a spectrum with a filled valley (i.e., $\alpha=1$ for $h\nu \geq E_g$). The theoretical conversion efficiency for an absorption profile without a valley is improved to 30% at an optimum gap E_g~1.5 eV [Fig. 2.2b]. The valley in the absorption spectrum significantly impacts the generation current and is responsible for approximately 2/3 of the reduction in the conversion efficiency relative to the SQ limit. Additional calculations illustrating the impact of the peak-to-valley ratio on the

conversion efficiency are provided in the supporting information; as expected the efficiency moves monotonically higher as the valley is filled. In a practical NC PV cell, the gap could be filled by increasing the layer thickness or by inclusion of NCs with a higher E_g or polymers with complementary absorption characteristics as a 'secondary' absorber.

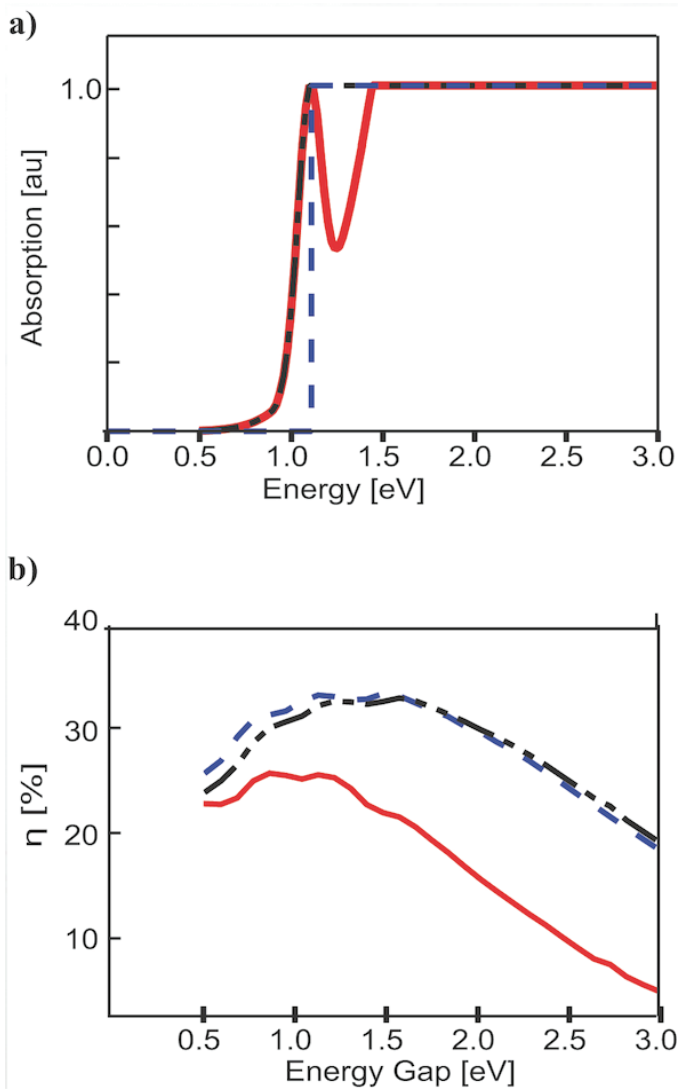

Figure 2.2: Absorption profiles for idealized SQ (blue, dashed), NC with complete absorption above E_{gap} (black, dot-dash), and NC with complete absorption at E_{gap} (red, solid) and the corresponding efficiencies; (b) efficiencies as a function of *width* and E_g for a fixed E_{en} of 0.015eV and complete absorption at E_g (red, solid from (b)) with the maximum of 25.8% at 1.0eV gap and 70meV total width.

Next, we analyze the impact of absorption tail on theoretical conversion efficiency limits; details are provided in the supporting information. The nature of the absorption tail depends on the relative contribution of physical disorder (Gaussian tail) and energetic disorder (exponential tail) [Fig. 2.3]. We investigated the parameter space corresponding to values that are reasonably accessible by experiment, specifically 10-130 meV for both the exponential and Gaussian components of our model. Figure 2.3b shows that the exponential tail arising from energetic disorder reduces open circuit voltage and device efficiency more significantly than the Gaussian tail associated with the physical disorder. Figure 2.3c illustrates the relative sensitivity of the efficiency to the energetic disorder (plotted on the abscissa) to physical disorder (plotted on the ordinate). Energetic disorder above 25 meV reduces the conversion efficiency limit to 13%. By contrast, the physical disorder can be quite large ranging from 20-70 meV with little to no degradation in the efficiency for a given value of E_{en}. Interestingly, the optimal E_{ph} is not at its minimum but at ~ 30meV for E_g~1.4 eV. The maximum arises from the fact that the Gaussian tail of the physical disorder dies much more quickly than the exponential tail of E_{en}; this allows for added current from a broader excitonic peak without providing many additional states below E_g which diminish the V_{oc}. The stronger dependence on E_{en} suggests that chemical or processing treatments that target the narrowing of the energy disorder are more critical than those that target size monodispersity. We fit several absorption spectra for dots ranging from 0.8 to 1.9 eV reported from different labs and found they were best fit for E_{en} between 14 and 21 meV and E_{ph} between 50 and 96 meV [Fig. 2.7]; showing that the region of high efficiency shown in Figure 2.2b should be experimentally accessible. Taken together, the analysis detailed above shows that both the absorption tail and the valley significantly degrade the PV conversion efficiency.

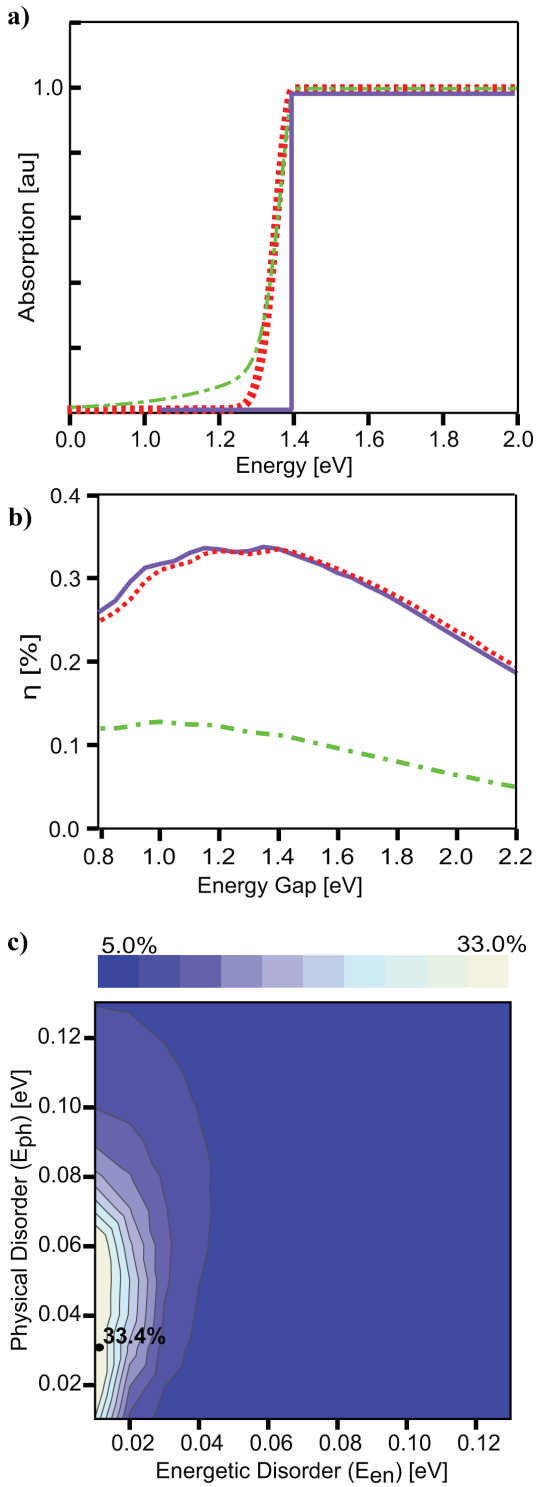

Figure 2.3: Impact of the absorption tail. (a) theoretical absorption profiles with primarily Gaussian tail and no valley (red, dotted), primarily exponential tail with no valley (green, dash-dot), and step function for reference (purple, solid); (b) corresponding conversion efficiencies, (c) contour plot of conversion efficiency as a function of energetic and physical disorder.

We now return to discuss general trends in the efficiency for NC absorber layers as a function of excitonic peak position and width. Figure 2.4 summarizes the detailed balance conversion efficiency limit of a NC solar cell as a function of E_g and W. The peak conversion efficiency of 25.8 % occurs at a gap of 1.0 eV with an effective peak width, W, of 70 meV. The peak width is a combination of energetic and physical disorder; the former was set to 15 meV based on experimental results of Erslev et al. [16], the latter was allowed to vary as a parameter and was found to be 48 meV. The origin of the optimum E_g is the same as in a conventional solar cell and derives from the fact that with increasing energy gap, the cell voltage increases while the current density decreases. The optimum peak width is relatively broad, centered around 70 meV for E_g between 1.0 and 1.2 eV. The presence of an optimum peak width derives from the fact that decreasing the width impacts J_{sc} and V_{oc} similarly to increasing the band gap. A broad excitonic peak is favorable for high current densities since it enables light absorption across a wider spectral range; however, the broad emission profile below the excitonic peak also reduces the photogenerated voltage of the cell.

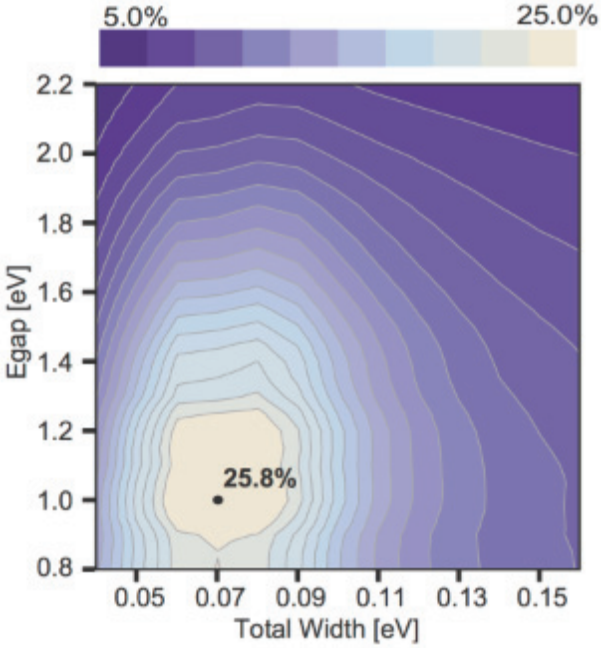

Figure 2.4: Contour plot of theoretical conversion efficiency as a function of excitonic energy gap, E_{gap}, and peak width, W.

Realizing PV conversion efficiencies beyond the SQ limits requires solutions to avoid the loss of photon energy in excess of the energy gap of the absorber. Several approaches to mitigate this inefficiency have been developed including cascaded multi-junctions, intermediate band cells, multi-exciton generation, and hot carrier collection. Interestingly, in the case of NC PV multi-junction,[19,20] multiexciton, [6,7] and hot-carrier collection [8] have been experimentally demonstrated, although in all cases the conversion efficiency still remains below the basic SQ limit. Below, we discuss the application of our detailed balance model to the theoretical conversion efficiency limits of NC tandem and NC MEG solar cells.

Multijunction cells utilize photon energy in excess of the gap by layering multiple cells composed of absorber layers with cascaded energy gaps. The conversion efficiency of multijunction solar cells depends on how the complimentary layers are connected. [21] In the two-terminal configuration, the top and bottom cell are electrically connected in series hence the voltages of the cells are additive while the current density must be matched. In the four-terminal configuration the current and voltage of the top and bottom cells are independent; details are provided in the supporting information.

The theoretical conversion efficiency limit of tandem NC PV involves four variables, *i.e.*, the width and the gap of the excitonic peak in the top and bottom layer. We calculated the conversion efficiency limits of tandem cells by iteratively solving for the optimum energy gap and width of both absorber layers with E_g ranging from 0.6eV to 2.2eV while imposing the constraint that the bottom cell E_g be smaller then that of the top cell. The optimum size distribution, E_{ph}, was varied from 20 to 100meV with a fixed E_{en} of 15meV; the total width is calculated (and reported in figure 2.4) as noted in section 2 and ranged from 40 to 130 meV for both layers.

The contour plots in Figure 2.5 illustrate the conversion efficiency of NC solar cells as a function of energy gap of the top and bottom cell. The peak conversion efficiency limit occurs at 31.5% for a cell with: $E_{g,top}$~1.3 eV and width ~80meV, $E_{g,bottom}$ ~0.80 eV and width ~70meV. The fine structure in the contour plot of the

conversion efficiency appears to arise from alignment of the trough in the absorption spectrum between the top and bottom excitonic peak with atmospheric absorption features in the AM 1.5.

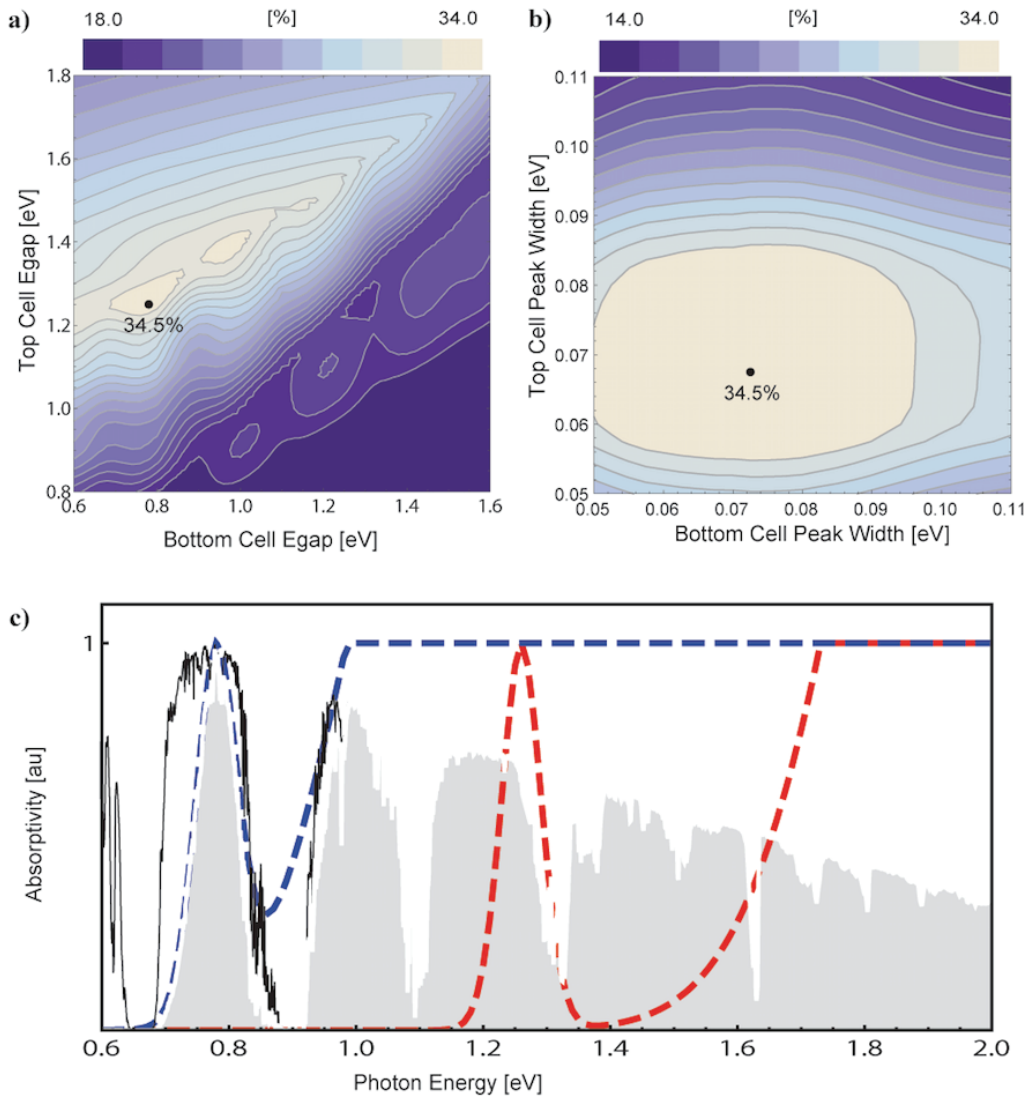

Figure 2.5: Conversion efficiency limits of tandem NC solar cells. (a) Impact of the band gap, and (b) total energy width (c) absorption spectra for the top (red, dashed) and bottom (blue, dashed) cells for the highest efficiency tandem cell, the greyed portion of the AM1.5 represents the incident spectra that is absorbed.

Figure 2.5c shows the composite absorption spectrum of the tandem device stack comprising two NC absorber layers overlaid on the incident AM 1.5 spectrum. To understand the origin of the local maxima of the conversion efficiency we calculated

the detailed balance limit of a tandem NC solar cell illuminated by a smooth blackbody spectrum (T=5700K). In this case, the contour plot of conversion efficiency limits shows only a broad, global maximum near $E_{g,top}$~1.3 eV and $E_{g,bottom}$~0.80 eV.

MEG in NC solar cells introduces the opportunity to utilize excess photon energy above the energy gap to breach the one-to-one limit between absorbed photon and generated electron-hole pair.[22] The detailed efficiency analysis can be easily modified to account for MEG effects by including quantum yield in the form of an internal quantum efficiency (QE) greater than unity. Previous studies have modeled the QE for MEG solar cells as a staircase function in the thermodynamic limit or as a semi-empirical model based on a linear MEG efficiency with a slope and onset derived from experimental data. In the limit of the idealized stair-case MEG quantum yield, the single junction conversion efficiency can be enhanced up to 44%. [23,24]

We analyzed the impact of MEG on the detailed balance limit of NC solar cells by including a MEG QE>1 term in the analysis outlined above, but preserving the characteristic excitonic absorption peak edge near Eg. Consistent with previous reports, our calculations show that MEG can significantly enhance the conversion efficiency relative to the non-MEG case.

2.4 Conclusions

We have calculated the maximum theoretical efficiency for NC PV cells based on a detailed balance approach. For single junction cells the maximum efficiency is 25.8% for an energy gap of 1.0 eV and is located on a plateau in the efficiency plot allowing for a range of both energy gap and width with little impact in the overall power conversion. In tandem cells with 2 junctions the maximum is 34.1% and is much more sensitive to both the energy gaps and width of the individual cells. We also find that the impact of the energy distribution due to energetic disorder is much stronger than that caused by size distributions. Lastly, we find that the largest effect on the potential efficiency is the valley in between the 1st and 2nd excitonic peaks and capturing this photon density, without negatively impacting the transport properties in the device, is key to approaching the SQ limits for discrete NC absorbers.

2.5 References

1 A. Hagfeldt and M. Gratzel, Accounts of Chemical Research **33**, 269 (2000).

2 M.K. Nazeeruddin, E. Baranoff, and M. Gratzel, Solar Energy **85**, 1172 (2011).

3 T. Todorov and D.B. Mitzi, European Journal of Inorganic Chemistry (2010).

4 H.J. Snaith, J Phys Chem Lett **4**, 3623 (2013).

5 J. Tang and E.H. Sargent, Adv Mater **23**, 12 (2010).

6 J.B. Sambur, T. Novet, and B.A. Parkinson, Science **330**, 63 (2010).

7 O.E. Semonin, J.M. Luther, S. Choi, H.Y. Chen, J. Gao, A.J. Nozik, and M.C. Beard, Science **334**, 1530 (2011).

8 W.A. Tisdale, K.J. Williams, B.A. Timp, D.J. Norris, E.S. Aydil, and X.Y. Zhu, Science **328**, 1543 (2010).

9 A.H. Ip, S.M. Thon, S. Hoogland, O. Voznyy, D. Zhitomirsky, R. Debnath, L. Levina, L.R. Rollny, G.H. Carey, A. Fischer, K.W. Kemp, I.J. Kramer, Z. Ning, A.J. Labelle, K.W. Chou, A. Amassian, and E.H. Sargent, Nature Nanotech **7** 577 (2012).

10 W. Shockley and H.J. Queisser, J Appl Phys **32**, 510 (1961).

11 T. Kirchartz, K. Taretto, and U. Rau, J. Phys. Chem. C **113**, 17958 (2009).

12 J.H. Werner, J. Mattheis, and U. Rau, Thin Solid Films **480-481**, 399 (2005).

13 U. Rau and J.H. Werner, Appl Phys Lett **84**, 3735 (2004).

14 F. Wise, Accounts of Chemical Research **33**, 773 (2000).

15 S. Schmitt-Rink, D. Miller, and D.S. Chemla, Phys Rev B **35** 8113 (1987).

16 P.T. Erslev, H.-Y. Chen, J. Gao, M.C. Beard, A.J. Frank, J. van de Lagemaat, J.C. Johnson, and J.M. Luther, Phys Rev B **86**, 155313 (2012).

17 J.J. Peterson and T.D. Krauss, Nano Lett. **6,** 510 (2006).

18 I. Kang and F. Wise, Journal of the Optical Society of America B-Optical Physics **14**, 1632 (1997).

19 S. Choi, J. Luther, M. Hanna, and A. Nozik, Nano Lett **8**, 3904 (2008).

20 X. Wang, G.I. Koleilat, J. Tang, H. Liu, I.J. Kramer, R. Debnath, L. Brzozowski, D.A.R. Barkhouse, L. Levina, and S. Hoogland, Nature Photon **5**, 480 (2011).

21 J. Nelson, *The Physics of Solar Cells* (World Scientific Publishing Company Incorporated, 2003).

22 A. Nozik, Physica E **14**, 115 (2002).

23 M.C. Hanna and A.J. Nozik, J Appl Phys **100**, 074510 (2006).

24 V.I. Klimov, Appl Phys Lett **89**, 123118 (2006).

2.6 Supporting Information

2.6.1 Calculation of current density and short circuit voltage

We briefly summarize how key PV performance characteristics are calculated in the detailed balance analysis. The incident solar emission flux $\Phi S_{(E)}$ can be modeled either as a blackbody spectrum at a temperature of T~6000K or using the standard AM1.5 spectrum. Our analysis is based on the AM1.5 spectrum, although the general trends are insensitive to the specific choice of spectrum. The recombination current density is described in terms of the blackbody emission flux of the cell $\Phi C_{(E)}$. at a temperature TC=300K. The short circuit current density, Jsc, generated in the cell is given by the difference between generation and recombination current density:

$$J_{sc} = q\int_0^{\infty}\left\{\left(\Phi_{S(E)}QE_{(E)}\alpha_{(E)}\right)_G - \left(\Phi_{C(E)}QE_{(E)}\varepsilon_{(E)}\right)_R\right\}dE \tag{2.2}$$

, where q is the fundamental charge of an electron, α(E) and ε(E) are the absorption and emission profiles respectively, and (QE) is the internal quantum efficiency which accounts for the number of electrons generated per absorbed photon. The open circuit voltage is proportional to the natural log of the ratio of absorbed to emitted current density according to:

$$V_{OC} = \frac{k_B T_C}{q}\ln\left(\frac{\int_0^{\infty}\Phi_{S(E)}QE_{(E)}\alpha_{(E)}dE}{\int_0^{\infty}\Phi_{C(E)}QE_{(E)}\varepsilon_{(E)}dE}\right) \tag{2.3}$$

, where ε(E) is the emissivity of the active layer, which in the detailed balance analysis is taken to be the same as the absorptivity, α(E). Equations (2.2) and (2.3) underscore the material-specific absorptivity and emissivity as critical determinants of the solar conversion efficiency. Current and voltage of the device are related through the diode equation:

$$J_{(V)} = J_{sc} - J_0\left(\exp\left(\frac{qV}{k_B T_C}\right) - 1\right) \tag{2.4}$$

, where Jo is the reverse bias saturation current density in the dark, kB is the Boltzmann constant, and TC is the temperature of the cell. Finally, the conversion efficiency at the maximum power point (MPP) is given by:

$$\eta = \left(J_{(V_{MPP})} V_{MPP}\right) / P_{in} \tag{2.5}$$

, where Pin is the incident light power density for the AM1.5 spectrum (100 mW/cm^2).

2.6.2 Detailed absorption model and comparison to experimental spectra

The theoretical absorption spectrum discussed in the main text was fit to experimental data using the Igor software package and is implemented as:

$$\alpha\left(h\upsilon, E_{en}, E_{ph}\right) = \sum_i \int_{0.3eV}^{4.43eV} A_i \left[\frac{1}{2}\left(1 + erf\left[\frac{\beta h\upsilon}{\sqrt{2}}\right]\right)\right] \exp\left(-\frac{\left(h\upsilon - E_i\right)^2}{B_i E_{ph}^2}\right) \exp\left(-\frac{\left|h\upsilon - E_i\right|}{B_i E_{en}}\right) dh\upsilon \tag{2.6}$$

where β is the skewing factor and A_i and B_i are empirical factors. The bracketed term with the erf function is the skewing function and β is found by generating a normal distribution with respect to particle size, translating the size axis to energy, then fitting a skewed normal distribution; the value for β is fixed at 1.18 for all excitation energies.

A_i and B_i are empiricisms that account for the additional states at each transition due to changes in the magnetic quantum number (m) which we have not calculated explicitly. These are found through a series of fits to experimental data then fixed at the values listed below in Table 2.1. There are a maximum of 9 different allowed transitions for the quantum number n within the solar spectrum and, therefore, 9 different empirical values each of which applies to several different values of l. A_1 is set to 1 so that the models are normalized at the primary excitation energy, and B_1 is 1 as there are no additional m states for the first transition.

Table 2.1: Empirical values for absorption model

index	A [1/E_{gap}]	B [1/E_{gap}]
1	1	fit
2	1.25	37.5
3	1.375	43.75
4	1.8	50.0
5	2.3	62.5
6	2.5	62.5
7	2.625	68.75
8	2.75	75.0
9	2.875	81.25

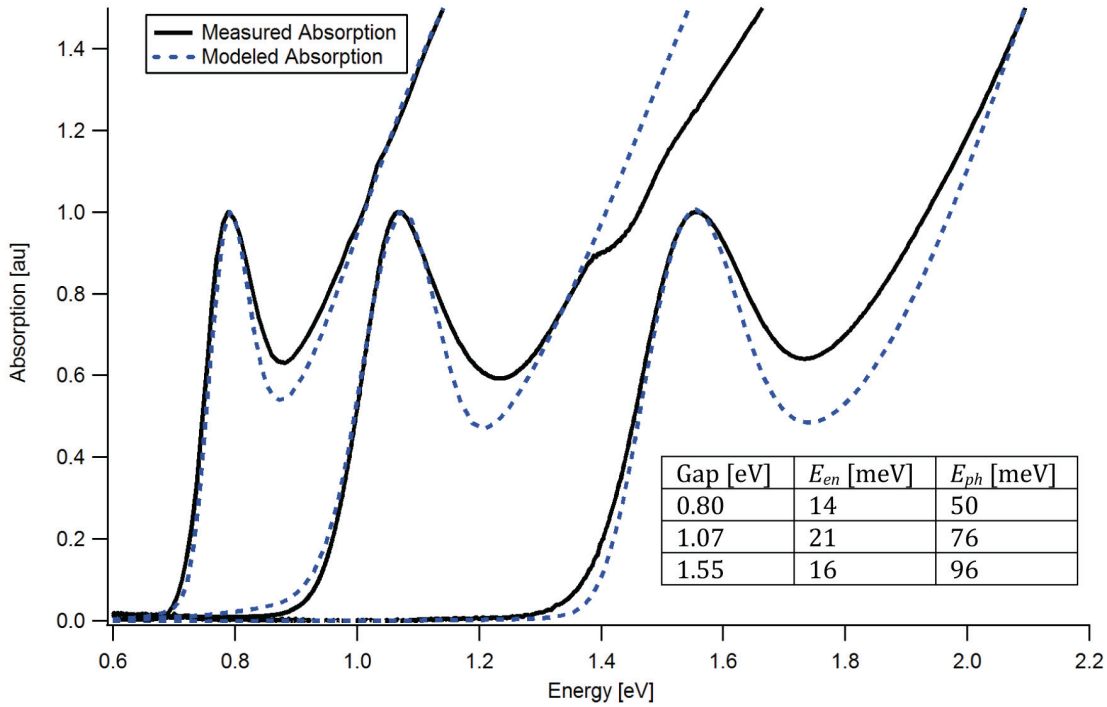

Gap [eV]	E_{en} [meV]	E_{ph} [meV]
0.80	14	50
1.07	21	76
1.55	16	96

Figure 2.6 Modeled (blue, dashed) and experimental (black, solid) absorption spectra, fit parameter values are given in the table. Colloidal NCs were synthesized according to the method adopted from Scholes and Hines. 0.8eV NCs were made by Joshua Choi in the Hanrath lab and spectra taken via photothermal deflection spectroscopy in the Salleo group at Stanford, 1.07eV NCs were made by David Moore in the Hanrath lab and spectra taken on a Cary 5000 UV-Vis/NIR spectrometer, 1.55eV NCs were made by Kyle Seyler in the Wise group lab and measured on a Shimadzu UV3600 UV-Vis/NIR spectrometer.

2.6.3 *The relationship between peak-to-valley ratio of the NC absorption profile on PV conversion efficiency.*

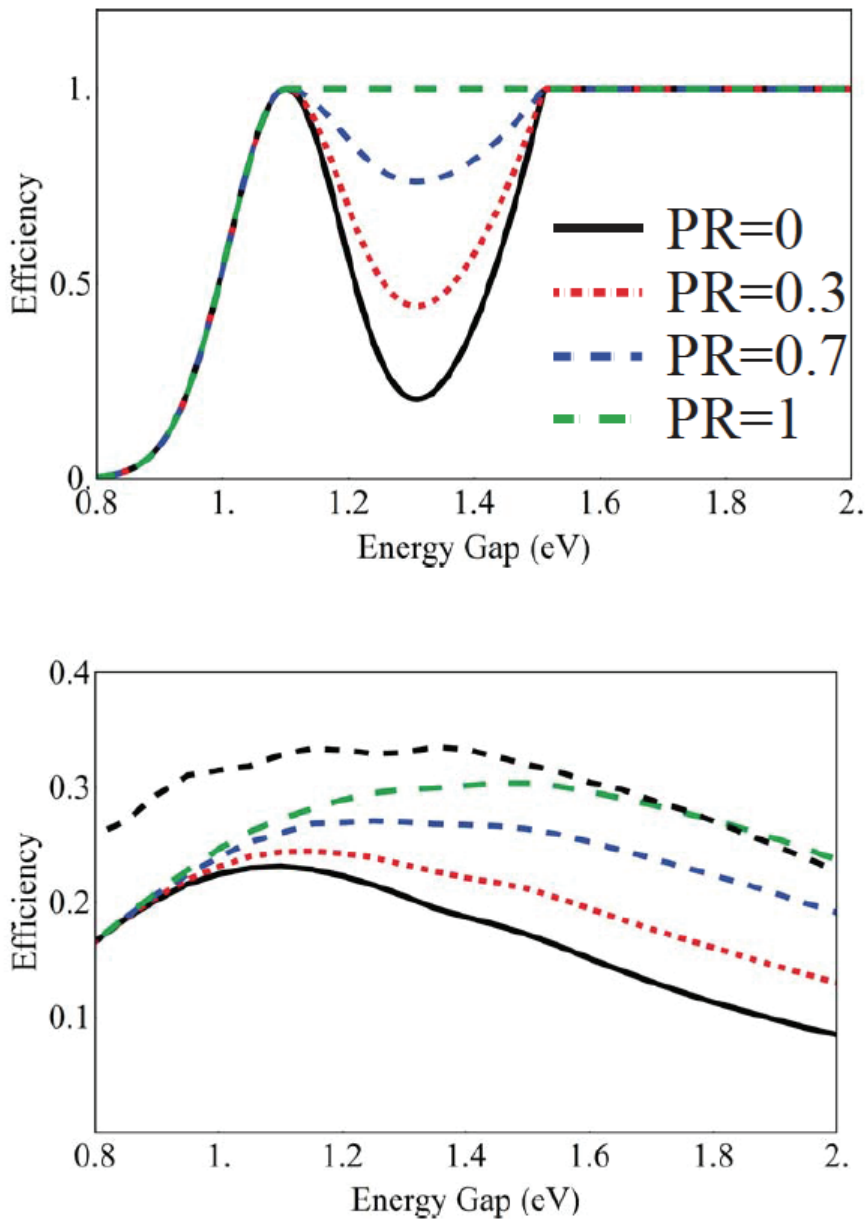

Figure 2.7: Absorption profiles (top) and maximum efficiency (bottom) for different peak-to-valley ratios (PR). PR ratio are arbitrary and range from 0, for no change to the modeled absorption and, 1 for complete absorption. For comparison, The dotted black line in the bottom plot shows the basic SQ limit.

2.6.4 *The nature of the low energy absorption tail*

The nature of the low energy absorption tail has important implications on the detailed balance limit of the NC solar cells. In our basic absorption profile, the excitonic transitions were modeled as a Gaussian peak in the form of:

$$\alpha_{1(E)} = \exp\left(\frac{-\left(E - E_g\right)^2}{2w^2}\right) \tag{2.7}$$

As discussed in the main text, we investigated the relationship between the nature of the tail edge and the detailed balance limit. The exponential or hybrid exponential peak has the form.

$$\alpha_{1(E)} = \exp\left(\frac{-\left(E - E_g\right)^n}{2w^2}\right) \tag{2.8}$$

, where the exponent n=1 in the case of a purely exponential peak, n=1.5 for a hybrid peak, and n=2 for a Gaussian peak.

2.6.5 *Conversion efficiency limits in the tandem NC solar cell*

Conversion efficiency limits in the tandem NC solar cell were calculated as follows. For a given energy gap and exciton peak width of the NC in the top and bottom layers, the short circuit current densities were calculated from:

$$J_{sc_top} = q\int_0^\infty \left\{\left(\Phi_{S(E)}\alpha_{top(E_{gt},w_t)}\right)_G - \left(\Phi_{C(E_{gt})}\varepsilon_{top(E_{gt},w_t)}\right)_R\right\}dE \tag{2.9}$$

$$J_{sc_bottom} = q\int_0^\infty \left\{\left(\Phi_{S(E)}\alpha_{btm(E_b,w_b)}\left(1-\alpha_{top(E_{gt},w_t)}\right)\right)_G - \left(\Phi_{C(E_{gt})}\varepsilon_{btm(E_{gb},w_b)}\right)_R\right\}dE \tag{2.10}$$

, where q is the fundamental charge of an electron and $\alpha_{top(E_t,w_t)}$ and $\alpha_{btm(E_b,w_b)}$ are the absorption profile of the top and bottom cell, respectively. The first term in the

integral refers to the generation and the second term refer to the recombination current density. Note, quantum efficiency (QE) was set equal to unity in the tandem efficiency calculations. Moreover, the mutual irradiance (i.e. blackbody emission from the top on the bottom cell and vice versa) was neglected from these calculations. De Vos showed that the electroluminescent contribution from the complementary cell is negligible.

In the case of the two-terminal tandem cell, the maximum power point is found under the constraint that the current density from the top and bottom cells is equal. Numerical iterations were applied to determine how the total cell voltage distributes across the top and bottom cell to meet the current matching constraint for a given combination of $\alpha_{top(E_t,w_t)}$ and $\alpha_{btm(E_b,w_b)}$.

2.6.6 Choice of Spectrum

To determine the impact of the alignment of the valley with "valleys" in the AM1.5G spectrum we ran the calculations for efficiency as a function of energy gap and Width using blackbody radiation. The results are in figure 2.8 and show little dependence, both qualitatively and quantitatively, on the choice of spectrum in term

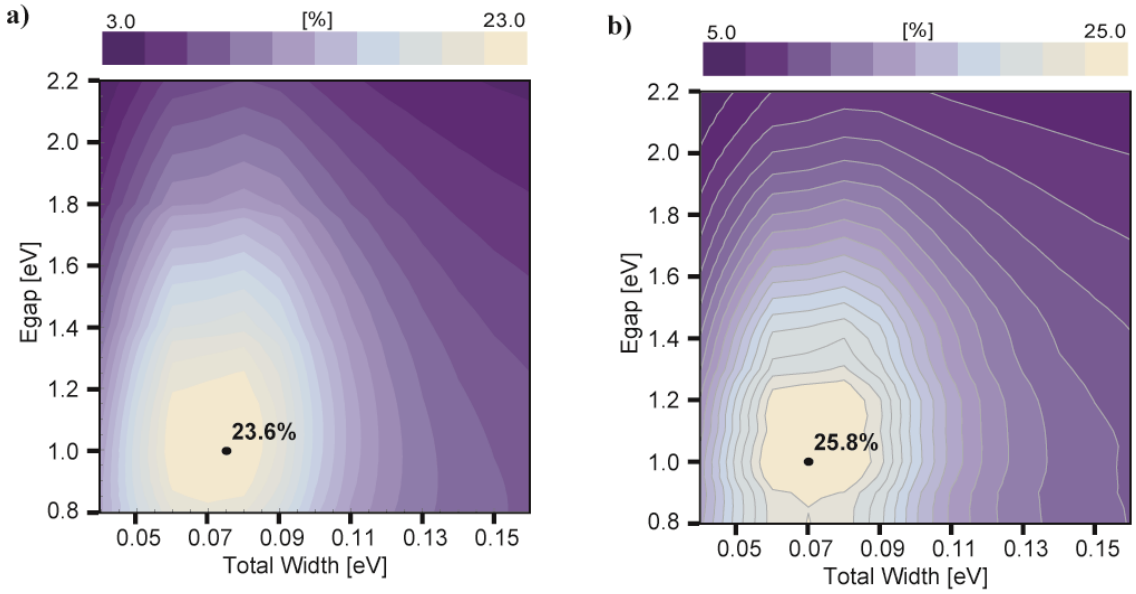

Figure 2.8: Efficiency plots for the maximum efficiency with Een fixed at 15meV for (a) blackbody spectrum, and (b) AM1.5G spectrum (same as plot 1c).

2.6.7 *Modeling of quantum yield in the case of multiexciton generation*

The basic relationships between multiexciton generation (MEG), electron-hole pair multiplication and quantum yield (QY) were detailed in a recent paper by Beard et al. Our detailed balance analysis accounted for MEG effects reflected in the quantum yield as follows.

The basic thermodynamic limit for QY for MEG is given by the staircase function:

$$QY = \begin{cases} 0 \text{ for } \dfrac{h\nu}{E_g} < 1 \\ \left\lfloor \dfrac{h\nu}{E_g} \right\rfloor \text{ for } \dfrac{h\nu}{E_g} \geq 1 \end{cases} \tag{2.11}$$

, where the staircase operator $\lfloor \ \rfloor$ signifies rounding down to the nearest integer.

The linear MEG QY model introduces a slope, m and threshold Θ to account for experimentally observed MEG efficiencies

$$QY = \begin{cases} 0 \quad \text{for } \dfrac{h\nu}{E_g} < 1 \\ 1 \quad \text{for } 1 \leq \dfrac{h\nu}{E_g} < \Theta \\ m\left(\dfrac{h\nu}{E_g}\right) \text{ for } \dfrac{h\nu}{E_g} \geq \Theta \end{cases} \tag{2.12}$$

We compared three QE models as illustrated in Fig. 2.9a: a staircase model and two linear models with specific MEG onset and efficiency. Fig. 2.9b compares the conversion efficiency of MEG NC solar cells with exciton absorption features and three MEG QE models. Fig. 2.9c illustrates the calculated conversion efficiency limits as a function of Egap and W. Interestingly, the conversion efficiency continuously increases with decreasing peak width, W. We interpret this trend as an indication that high Voc can be achieved with narrow excitonic peaks while the Jsc enhancements are realized due to MEG. Consistent with earlier results for step-function absorption

functions, MEG considerations increase conversion efficiency (up to 30% in the staircase model), for optimum energy gaps near 1.0eV.

a)

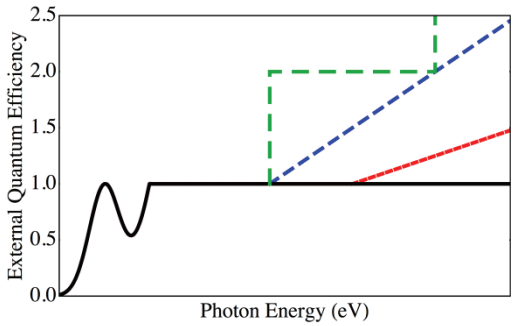

b)

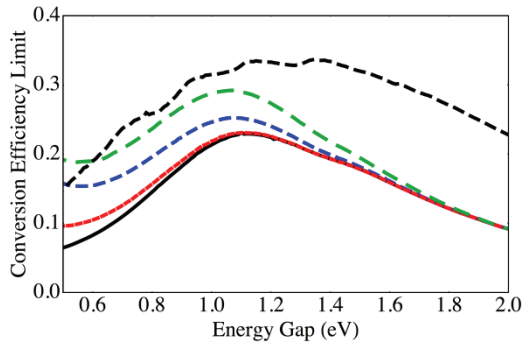

c)

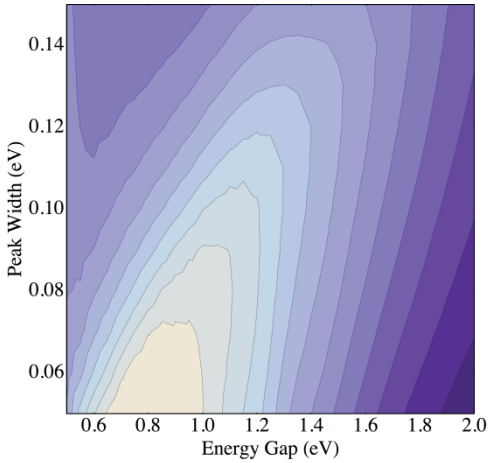

Figure 2.9: (a) absorption functions used for calculating efficiencies, for energies below MEG onset we use the modeled function (black, solid) with complete absorption at the primary excitation energy and MEG models for a step function (green, dash), a continuous function with onset at $2*E_{gap}$ (blue, dash), and continuous with onset at $2.5*E_{gap}$ (b) corresponding maximum efficiencies as a function Egap, SQ limit (black, dash) is shown for comparison (c) maximum efficiency with varied E_{gap} and total Width for a profile with a completely filled valley and a step function for MEG at $2*E_{gap}$ onset.

CHAPTER 3 THERMALLY INDUCED STRUCTURAL EVOLUTION AND PERFORMANCE OF MESOPOROUS BLOCK COPOLYMER-DIRECTED ALUMINA PEROVSKITE SOLAR CELLS

3.1 Abstract

Structure control in solution-processed hybrid perovskites is crucial to design and fabricate highly efficient solar cells. Here, we utilize in situ grazing incidence wide-angle X-ray scattering and scanning electron microscopy to investigate the structural evolution and film morphologies of methylammonium lead tri-iodide/chloride ($CH_3NH_3PbI_{3-x}Cl_x$) in mesoporous block copolymer derived alumina superstructures during thermal annealing. We show the $CH_3NH_3PbI_{3-x}Cl_x$ material evolution to be characterized by three distinct structures: a crystalline precursor structure not described previously, a 3D perovskite structure, and a mixture of compounds resulting from degradation. Finally, we demonstrate how understanding the processing parameters provides the foundation needed for optimal perovskite film morphology and coverage, leading to enhanced block copolymer-directed perovskite solar cell performance.

3.2 Introduction

Harnessing sunlight to generate photovoltaic electricity based on thin film solar cell technologies is desirable to deliver green, sustainable energy at reduced materials and fabrication cost.[1,2] Thin film hybrid solar cells using solution-processable materials[2] such as semiconductor nanocrystals,[3,4] organic polymers,[5,6] or dye-sensitized solar cells[7–9] have achieved 7-12% power conversion efficiencies (PCEs). Recently, a new class of highly efficient solid-state hybrid perovskite solar cells has been reported pushing PCEs above 15%.[10–34]

Organic-inorganic hybrid materials enable the combination of both organic and inorganic qualities into a single molecular composite. These hybrid materials have been studied extensively for their electrical, mechanical, and optical functional properties and have been applied, for example, in field-effect transistors,

optoelectronic devices and hybrid solar cells.[35–38] Another area of intense scientific research and commercial interest is utilizing the methylammonium lead trihalide ($CH_3NH_3PbX_3$; X = I, Br, Cl) semiconducting perovskite in thin film photovoltaics.[10–34] The $CH_3NH_3PbX_3$ perovskite semiconductor material is highly attractive due to the ease of solution processing and excellent absorption properties in the near-infrared spectrum to generate charge carriers.[10,12,13,18] Moreover, ambipolar charge transport properties and long carrier lifetimes enable the direct transport of both photogenerated electron and hole charge carriers to the respective collecting electrodes.[14,15,18,19,28,29,34] The photovoltaic device architecture provides an alternative approach to enhance device performance.[39–41] In particular, block copolymer (BCP) self-assembly-directed materials have improved charge transport and light management of mesoscopic solar cells via control of morphology,[37,38,41–46] porosity and pore size,[46–50] material crystallinity,[51,52] electronic[37,52] and optical[47,53] properties. For example, well-ordered bicontinuous BCP gyroid morphologies enable easy backfilling of the hole transport materials and complete mesopore interconnectivity in solid-state dye-sensitized solar cells.[37,38] Moreover, porous BCP nanostructures provide control over single crystal epitaxial nanostructures,[51] and may enable tuning the feature size and morphology of well-defined $CH_3NH_3PbX_3$ nanocrystallites within the BCP mesoporous heterojunction electrode to achieve excellent photovoltaic device performance.[19,24,32–34] Combining BCP structure control with the organic-inorganic hybrid perovskite, observation of structural evolution at multiple length scales is expected to be key to establishing structure-property correlations. To the best of our knowledge, such evolution of thermally annealed hybrid perovskites obtained via a single-step spin coating process has not been reported.

In this work we employed in situ time-resolved grazing incidence wide-angle x-ray scattering (GIWAXS) to probe the structure of methylammonium lead tri-iodide/chloride ($CH_3NH_3PbI_{3-x}Cl_x$) perovskites in mesoporous block copolymer-directed alumina (MBCP-Al_2O_3) during thermal annealing. Optimized structure and film morphology of the organic-inorganic hybrid perovskites resulted in enhanced meso-superstructured solar cell performance.

3.3 Results and Discussion

3.3.1 GIWAXS of $CH_3NH_3PbI_{3-x}Cl_x$ Perovskites

One of the key advantages of the $CH_3NH_3PbX_3$ hybrid perovskite photovoltaic devices is the ease of solution-processing. The organic (CH_3NH_3I) and inorganic precursors ($PbCl_2$) are dissolved in a common solvent (N,N-dimethylformamide), deposited on a substrate by spin coating, and annealed at relatively low temperatures of 90-100 °C for 5-120 min to induce perovskite crystallization.[12–23,25–27] However, crystallographic data obtained from one-dimensional (1D) powder X-ray diffraction provides only limited structural information, in particular for the highly oriented perovskite thin films.[12,13,18,19,22–26] To this end, we employed GIWAXS with 2D detection capability to probe the crystallographic orientations of planar $CH_3NH_3PbI_{3-x}Cl_x$ perovskite thin films.

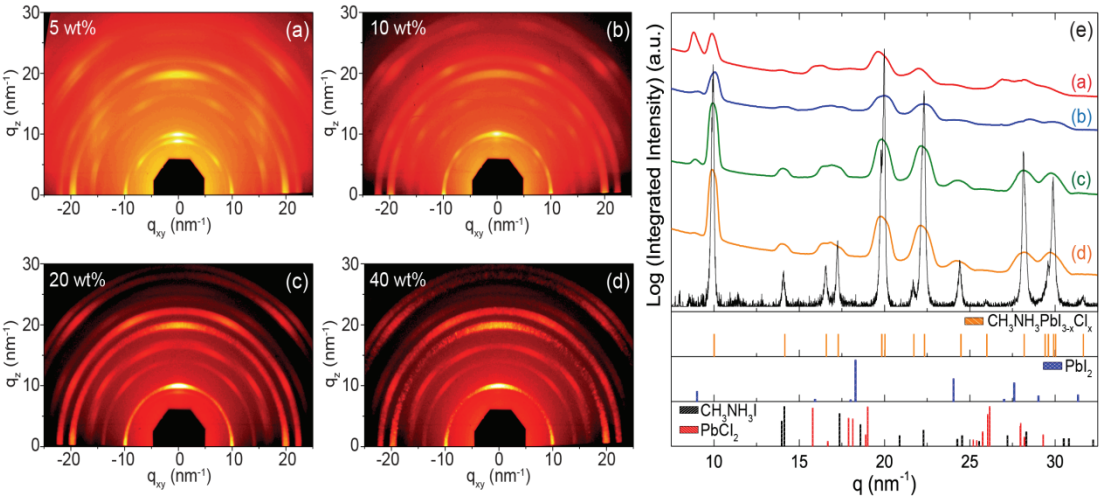

Figure 3.1: 2D GIWAXS profiles of $CH_3NH_3PbI_{3-x}Cl_x$ perovskite films on flat substrates prepared from (a) 5 wt%, (b) 10 wt%, (c) 20 wt%, (d) 40 wt% precursor solutions, and annealed at 100 °C for 45 min. (e) Azimuthally integrated intensity plots of the GIWAXS patterns. The bottom black curve is the XRD spectrum of the $CH_3NH_3PbI_{3-x}Cl_x$ perovskite measured in powdered form.

Figure 3.1 shows GIWAXS profiles of crystalline perovskite thin films on flat glass coverslips prepared from precursor solutions of different concentrations and annealed at 100 °C for 45 min in nitrogen atmosphere. We observe that the 5 wt% and 10 wt% perovskite films exhibit a mixture of scattered secondary spots and rings

(Figure 3.1a and 3.1b), indicating that crystalline domains are highly oriented in the in-plane direction. Similar GIWAXS profiles were observed for the thicker 20 wt% and 40 wt% perovskite films. The presence of strongly scattered rings in Figure 3.1c and 1d indicates that crystalline domains are predominantly polycrystalline (i.e. randomly oriented relative to the plane of the substrate). The azimuthally integrated scattering intensity of the different GIWAXS patterns is plotted against the scattering vector q in Figure 3.1e, where $q = 4\pi\sin\theta/\lambda$, θ is half of the total scattering angle, and λ is the X-ray wavelength (0.1161 nm). The 2D GIWAXS integrated intensity curves correspond well to the crystallographic peaks of the 1D X-ray diffraction pattern of a $CH_3NH_3PbI_{3-x}Cl_x$ powdered sample (black curve),[23] and are distinctly different from those of the CH_3NH_3I (PDF 00-10-0737) and $PbCl_2$ (PDF 00-050-0536) precursors (see bottom of Figure 3.1e). The lattice parameters for the tetragonal I4/mcm $CH_3NH_3PbI_{3-x}Cl_x$ powdered sample are a = 8.868(1) Å and c = 12.659(2) Å.[23,54–56] We note that while the broad GIWAXS scattering peaks do not allow precise structural assignments, distinct peaks observed for different species enable us to determine the predominant sample structure in real time. The scattering peak at $q = 10\ nm^{-1}$ was assigned to the (110) plane of $CH_3NH_3PbI_{3-x}Cl_x$ perovskite structure.[18,23] The scattering peak at $q = 9\ nm^{-1}$ assigned to the (001) plane of PbI_2 (PDF 00-007-0235) was present only in the 5 wt% perovskite film, suggesting thinner films underwent a more rapid degradation into PbI_2.[13,23]

3.3.2 Characterization of Mesoporous Block Copolymer-Directed Alumina Thin Films

In a solvent mixture of non-polar toluene and polar n-butanol, the structure directing polyisoprene-block-polystyrene-block-polyethylene oxide (PI-b-PS-b-PEO) triblock terpolymer forms micelles with the hydrophobic PI and PS in the core, and a hydrophilic PEO corona.[46–49] The added Al_2O_3 sol is selectively attracted to the PEO corona by hydrogen bonds.[42] Upon solvent evaporation, the organic-inorganic micelles self-assemble into a randomly packed arrangement. Mesoporous block copolymer-directed alumina (MBCP-Al_2O_3) thin films with interconnected porosity are generated when the organic components are removed by calcination as evidenced by the

scanning electron microscopy (SEM) and atomic force microscopy (AFM) images in Figures 3.2 and 3.6, respectively. The MBCP-Al_2O_3 pores are interconnected in both in-plane and out-of-plane directions. From SEM and AFM, the pore diameter is ~36 nm and the film thickness is 70-80 nm after calcination. In 2D grazing incidence small-angle X-ray scattering (GISAXS) patterns, we observe two intense diffraction peaks at qxy = ±0.157 nm^{-1} (Figure 3.2c) consistent with a disordered mesoporous material with a macroscopically homogenous in-plane d-spacing of $2\pi/qxy \approx 40$ nm.[49] The oscillations at the diffraction peaks are attributed to the form factor of the film thickness.[57] In contrast, the porosity of Al_2O_3 nanoparticulate films is macroscopically inhomogeneous as shown in Figure 3.7.[18–20]

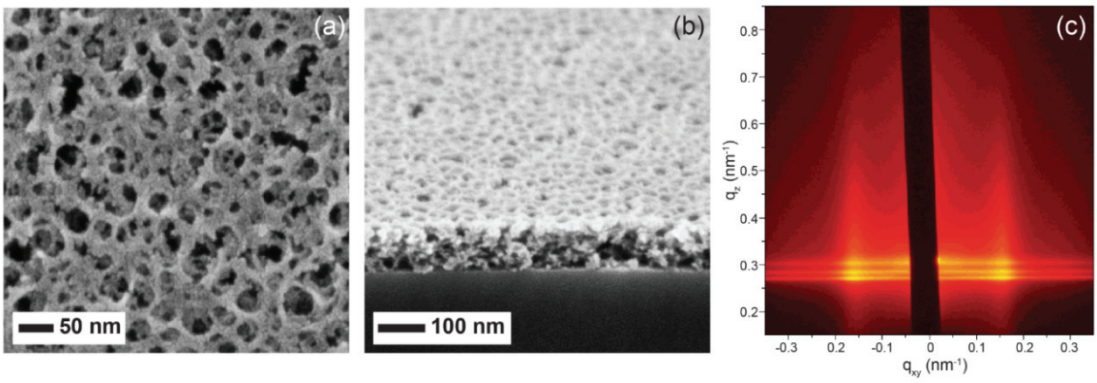

Figure 3.2 (a) Plan view and (b) cross-sectional SEM micrographs, and (c) 2D GISAXS profile at incidence angle of 0.16 °of MBCP-Al_2O_3 film after calcination.

3.3.3 In situ X-ray Characterization of MBCP-Al_2O_3 Perovskite Structural Evolution

The mesoporous support in solution-processed nanostructured $CH_3NH_3PbX_3$ perovskite solar cells fulfills multiple roles. For example, mesoporous TiO_2 acts as the distributed heterojunction with large surface areas for the generation of charges by the $CH_3NH_3PbI_3$ perovskite absorber, and collects and transports the electrons to the collecting electrode.[10–17,24,32–34] Moreover, mesoporous superstructures improve the coating of perovskite material to enhance coverage and light harvesting efficiency,[19] and act as a physical barrier to prevent the formation of "shunt paths" by direct contact of the hole transport material and electron selective layer.[18–22] We applied in situ GIWAXS to study the structural evolution of solution-processed $CH_3NH_3PbI_{3-x}Cl_x$ perovskite on MBCP-Al_2O_3 thin films during annealing in real time.

As mentioned earlier, we observed similar GIWAXS patterns for the 20 wt% and 40 wt% perovskite thin films (Figure 3.1c and 3.1d). Here we chose to deposit a 20 wt% perovskite precursor solution on the MBCP-Al_2O_3 thin film for isothermal-time-dependent (ITD) annealing in air and nitrogen, respectively. The precursor solution filled the interconnected mesopores and formed a "wet capping layer" on the superstructure scaffold with incomplete solvent removal. After deposition the sample was immediately loaded on a sample-stage held at 100 °C. It should be noted that in this way the ITD MBCP-Al_2O_3 perovskite samples underwent an immediate jump from ambient temperature to 100 °C. GIWAXS measurements were collected in real time over a dwell of 50 min. In the employed beam configuration, GIWAXS measured the perovskite material within the MBCP-Al_2O_3 scaffold and capping layer as the incidence angle of the incoming X-ray beam was above the critical angle of the silicon substrate. In situ 2D GIWAXS profiles and azimuthally integrated intensity plots of the ITD MBCP-Al_2O_3 perovskite structural evolution in nitrogen and air, respectively, are shown in Figure 3.3.

For the study of the ITD MBCP-Al_2O_3 perovskite behavior in nitrogen, the wet sample was loaded into a custom-made environmental chamber on the heated stage at 100 °C under flowing nitrogen.[58] Under these conditions, the wet sample exhibits multiple orders of scattering rings in the GIWAXS profile (Figure 3.3a), indicating the formation of crystalline material. Interestingly, from the integrated intensity plots in Figure 3.3c, at short times (3 min time point) we observe a distinct set of scattering peaks at lower q values (<9 nm-1) that are neither characteristic for CH_3NH_3I, $PbCl_2$, PbI_2, nor for the $CH_3NH_3PbI_{3-x}Cl_x$ perovskite structure. After 10 minutes the expected peaks for the mixed halide perovskite are observed (compare Figure 3.3c with Figure 3.1e). This observation suggests the formation of a distinct crystalline structure, which in the following discussion we will refer to as the "crystalline precursor structure". We assigned the peak at $q \approx 11$ nm^{-1} as the signature scattering peak for this crystalline precursor structure. Further investigation is currently underway to identify the structure of this crystalline precursor material. Somewhere between 3 and 10 min of annealing in nitrogen under the set conditions, the film underwent a transition to form

the mixed halide perovskite structure, at which point the intensity of the peak at q ≈ 11 nm^{-1} for the crystalline precursor in Figure 3.3c vanishes. The film started to degrade into PbI_2 after about 20-30 min of annealing, as indicated by the appearance of a scattering peak at q = 9 nm^{-1}. The degradation may be attributed to the presence of moisture in the chamber,[13,22,23,54,56] but at this point X-ray beam induced damage cannot be excluded either. For comparison, Figure 3.3b shows the GIWAXS profile of the MBCP-Al_2O_3 perovskite film after 50 min annealing in nitrogen at 100 °C.

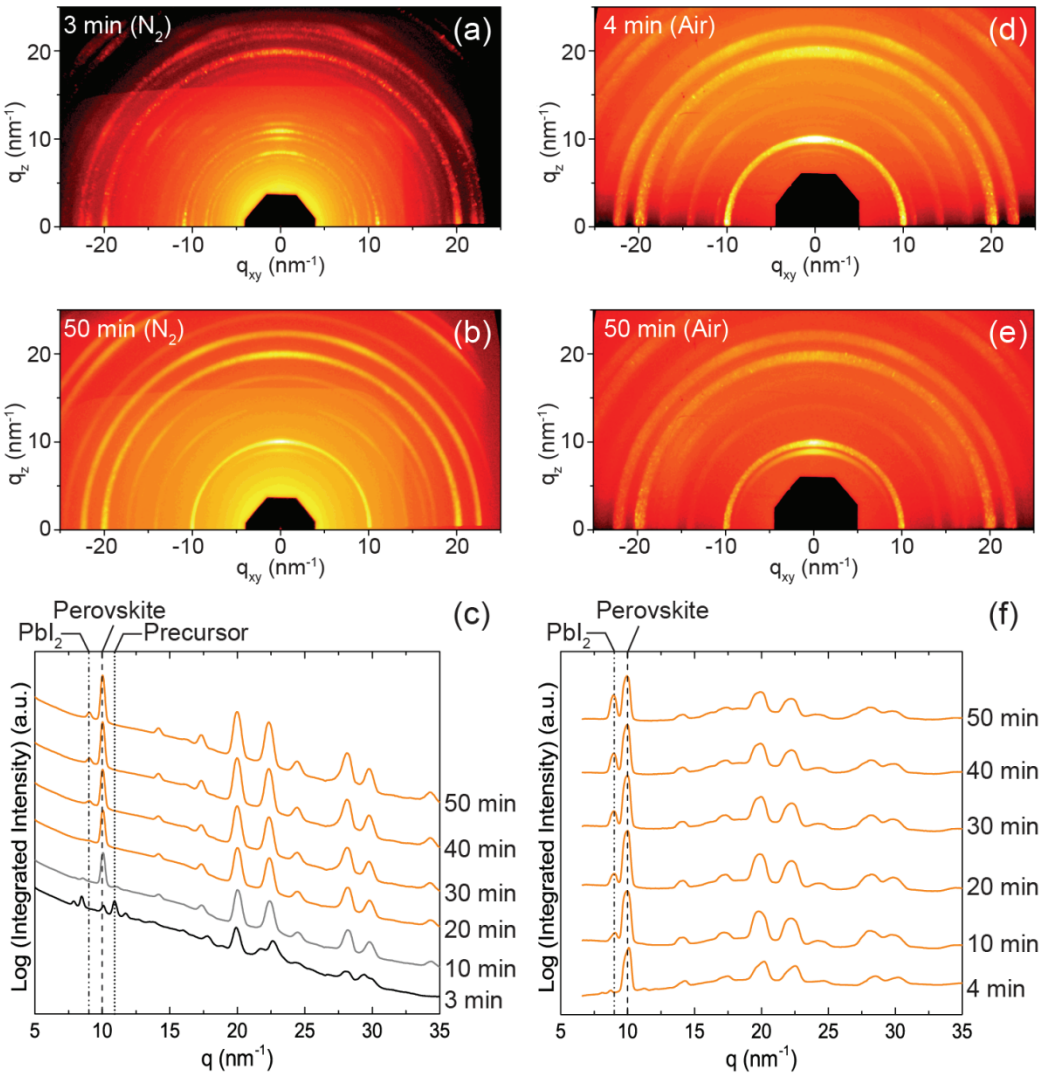

Figure 3.3: 2D GIWAXS profiles for ITD annealing of MBCP-Al_2O_3 perovskite films at 100 °C in (a, b) nitrogen and (d, e) air for different time points as indicated, together with (c, f) respective azimuthally integrated intensity plots. The dotted line at $q \approx 11$ nm^{-1}, dashed line at $q = 10$ nm^{-1}, and dash-dotted line at $q = 9$ nm^{-1} denote the signature scattering peaks for the crystalline precursor, perovskite, and PbI_2 structures, respectively.

From the beginning of ITD annealing at 100 °C in air, we observe multiple orders of scattering rings in the GIWAXS profile (Figure 3.3d), consistent with the rapid formation of a polycrystalline perovskite phase in the presence of MBCP-Al_2O_3. Figure 3.3f shows the azimuthally integrated intensity plot of the ITD experiments in air with the perovskite signature peak at q = 10 nm^{-1}. Within 10 min at 100 °C, the perovskite started to degrade to PbI_2 as signified by the new peak formed at q = 9 nm^{-1}. The degradation is likely to initiate from the perovskite film surface[56] and may be attributed to moisture in the air[13,22,23,54] and X-ray beam induced damage. Over the dwell of 50 min at 100 °C, the scattering peaks remained in the same positions as shown in Figure 3.3e and 3.3f, suggesting minimal reorientation changes to the perovskite structure. Under air the perovskite structure already showed first indications of degradation via the peak at q = 9 nm-1 by the 10 min time point. We suspect that the absence of the crystalline precursor structure may be due to a more rapid transition in air as compared to nitrogen. We observe similar behavior, i.e. the absence of the crystalline precursor for $CH_3NH_3PbI_{3-x}Cl_x$ on a MBCP-TiO_2 superstructure annealed in air, albeit with more severe degradation into PbI_2 (Figure 3.8).

To delineate how individual parameters contribute to the structural evolution of $CH_3NH_3PbI_{3-x}Cl_x$ on MBCP-Al_2O_3, we conducted time-temperature-dependent (TTD) GIWAXS measurements with a slow temperature ramp applied to the wet MBCP-Al_2O_3 perovskite sample in nitrogen. To that end, 20 wt% precursor solution was deposited on the MBCP-Al_2O_3 thin film and loaded into the environmental chamber held at 30 °C under flowing nitrogen. The temperature of the heating stage was raised by 10 °C at every 10 min time interval. It took approximately 2-3 min for the heated stage to reach the set temperature. Figure 3.4 displays four representative 2D GIWAXS profiles (a-d) while the integrated intensity plots (e) reveal the TTD structural evolution of the MBCP-Al_2O_3 perovskite sample from 30-100 °C over the dwell of 120 min.

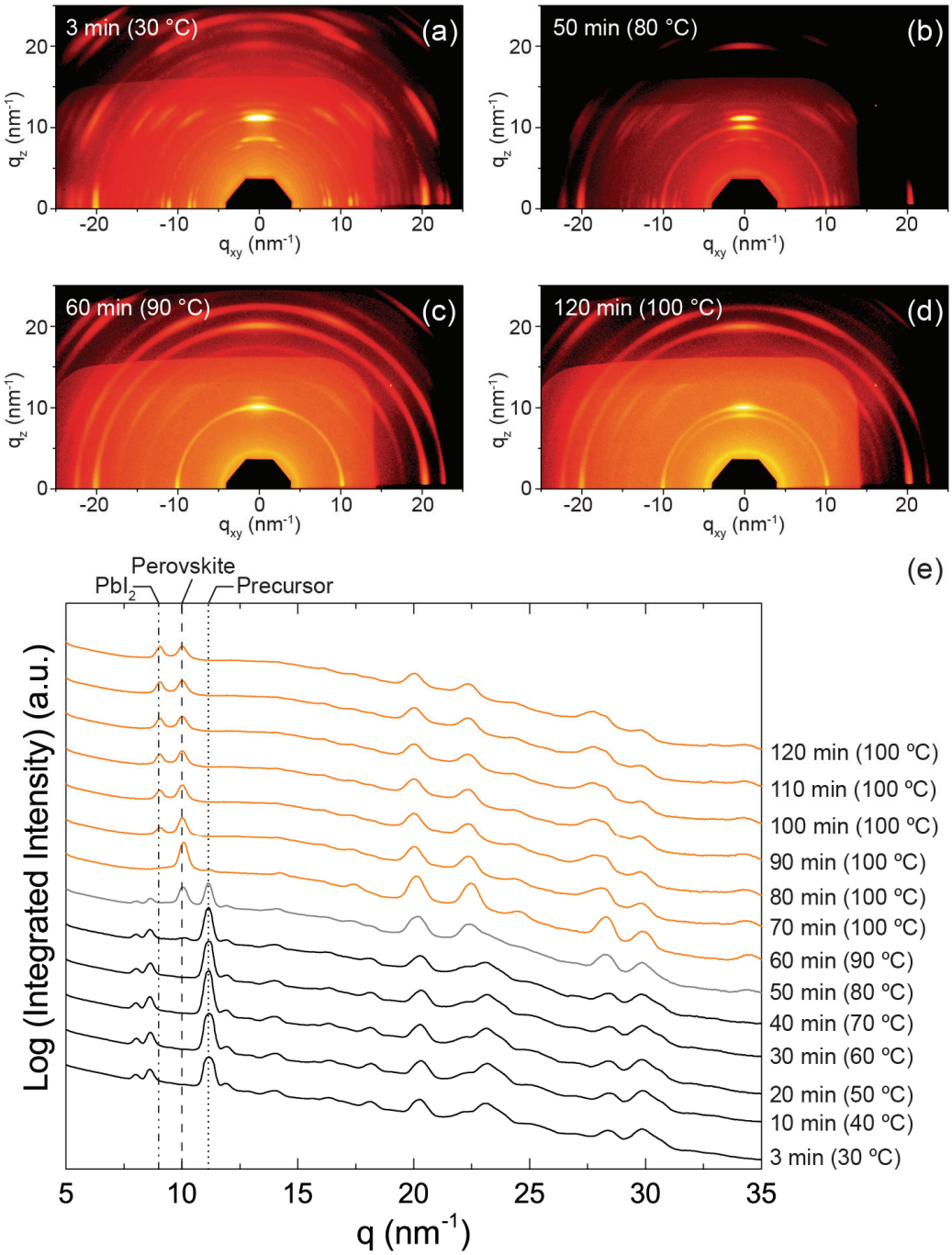

Figure 3.4: 2D GIWAXS profiles for TTD annealing of MBCP-Al_2O_3 perovskite films in nitrogen after (a) 3 min, (b) 50 min, (c) 60 min and (d) 120 min, together with (e) azimuthally integrated intensity plots. The dotted line at $q \approx 11$ nm^{-1}, dashed line at $q = 10$ nm^{-1}, and dash-dotted line at $q = 9$ nm^{-1} denote the signature scattering peaks for the crystalline precursor, perovskite, and PbI_2 structures, respectively. The difference in background brightness of the GIWAXS patterns is a shadow artifact of the experimental setup.

At the beginning of the experiment, the crystalline precursor was detected in the GIWAXS profile via the peak at q ≈ 11 nm^{-1}, see also GIWAXS pattern in Figure 3.4a showing results for the 3 min (30 °C) time point. At the 50 min time point (80 °C) a scattering ring appeared at q = 10 nm^{-1} (Figure 3.4b), indicating the transition from the crystalline precursor to polycrystalline perovskite. This structural transition was completed at the 60 min time point (90 °C, Figure 3.4c), similar to the 10 min time point for the ITD annealed MBCP-Al_2O_3 perovskite at 100 °C in nitrogen (compare with Figure 3.3c). Perovskite film degradation was observed at the 70 min time point after the temperature was raised to the final value of 100 °C, and progressed till the final time point at 120 min (Figure 3.4d). Similar to the ITD annealing in nitrogen, three distinct structures were identified during the TTD processing of $CH_3NH_3PbI_{3-x}Cl_x$ in MBCP-Al_2O_3 superstructures: (1) crystalline precursor, (2) perovskite, and (3) PbI_2 as a perovskite degradation product.

From the present and previous work, we conclude that transitions between these different structures are driven by a combination of annealing temperature, environmental atmosphere and film thickness.[22,26,27] A yet-to-be identified crystalline precursor structure was observed upon spin coating the $CH_3NH_3PbI_{3-x}Cl_x$ precursor solution on MBCP-Al_2O_3, and displayed noteworthy thermal stability during the TTD ramp annealing. We postulate that the crystalline precursor undergoes a solid-solid phase transformation to the 3D perovskite structure at 80 °C. This transition occurs relatively rapid (<10 min) and is largely completed at 90 °C. To the best of our knowledge, this is the first experimental observation of a transformation from a crystalline precursor to the perovskite crystal structure for methylammonium lead trihalide perovskite materials, suggesting a phase transformation pathway consistent with Ostwald's "Rule of Stages" in which a metastable precursor is first formed, followed by transformation into the more stable product.[59,60]

We further note that macroscopic coverage of the substrate with perovskite layers is largely affected by the heat treatment profile. In plan view SEM images (Figure 3.9a and 3.9b) we observe large (>2 μm) perovskite crystallite islands and pores in the capping layer on MBCP-Al_2O_3 under ITD annealing conditions. In

contrast, the discrete perovskite islands and pores are on the sub-micron length scale for the TTD annealed MBCP-Al_2O_3 perovskite film shown in Figure 3.9d and 3.9e. Since the only difference in the heat treatment profile is at the initial stage before perovskite formation, this result suggests that the crystalline precursor coverage and the subsequent phase transformation contributes significantly to the final film coverage, which in turn greatly affects device performance (vide infra).

3.3.4 MBCP-Al_2O_3 Perovskite Solar Cell Performance

Figure 3.5 shows SEM images of MBCP-Al_2O_3 perovskite films prepared from 40 wt% precursor solutions and annealed either instantaneously at 100 °C (ITD), or with a slow temperature ramp to 100 °C (TTD) in nitrogen. While the crystallite domain sizes are very similar for the ITD and TTD annealed films (Figure 3.5c and 3.5d), the capping film coverage is drastically different. Figure 3.5a shows that large pores (>1 μm) were formed in the capping layer of the MBCP-Al_2O_3 perovskite films annealed instantly at 100 °C (ITD). In contrast, when the MBCP-Al_2O_3 perovskite film was annealed with a slow temperature ramp of 5 °C / 5 min in nitrogen to 100 °C and held for 45 min at the final temperature (TTD), significantly better perovskite film coverage was achieved. The 40 wt% perovskite film morphology is highly similar to the 20 wt% perovskite films (Figure 3.9). We hypothesize that the crystalline precursor which is present for a longer dwell period during TTD annealing, promotes film formation with fewer macroscopic defects than in ITD annealed films.

We fabricated MBCP-Al_2O_3 perovskite solar cells annealed under ITD and TTD conditions. Comparing the best performing MBCP-Al_2O_3 perovskite solar cells in Figure 3.5e, the values of short-circuit current density (J_{SC}), open-circuit voltage (V_{OC}) and fill factor (FF) of the TTD-N_2 device increased by at least 15% relative to the ITD-air device. At the same time, the power conversion efficiency increased from 5.2% to 8.3%. We attribute the device performance improvement to the enhanced perovskite film morphology and coverage, enabling more uniform charge generation and collection, and reduced leakage with less available shunt paths.[19,22,26,27]

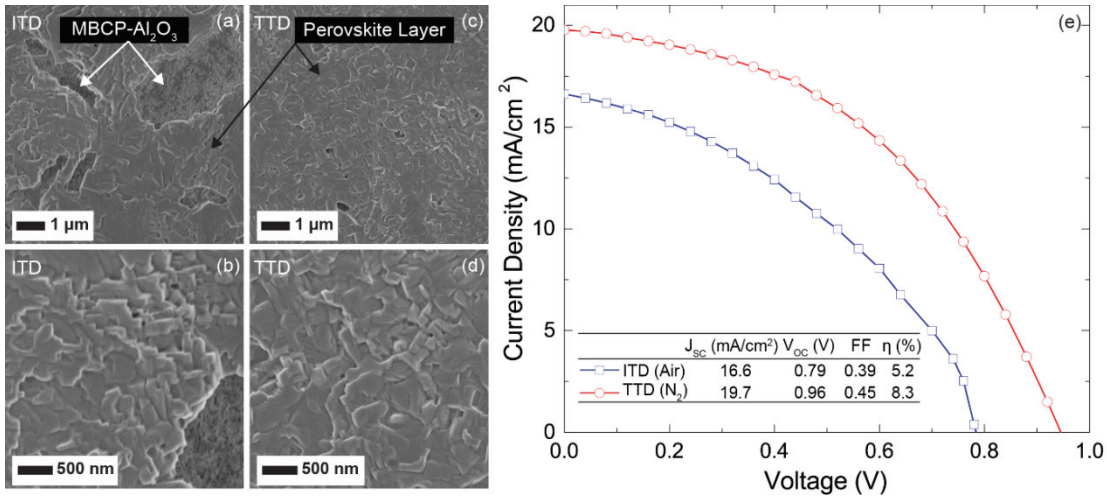

Figure 3.5: Plan view SEM micrographs of perovskite crystallization in MBCP-Al_2O_3 annealed under (a, b) ITD, and (c, d) TTD conditions in nitrogen. (e) Current density/voltage curves of best performing MBCP-Al_2O_3 perovskite solar cells measured under stimulated AM1.5 sunlight of 100 mW/cm^2 irradiation for different annealing conditions (ITD versus TTD).

3.4 Conclusion

In conclusion, we employed in situ 2D GIWAXS in combination with SEM to follow the structural evolution of $CH_3NH_3PbI_{3-x}Cl_x$ perovskite on mesoporous block copolymer Al_2O_3 thin films under thermal annealing. Solution-processed perovskite films underwent transitions between three distinct crystalline structures during thermal annealing: a crystalline precursor, a perovskite and a degradation product in the form of PbI_2. Finally, we demonstrated by annealing the MBCP-Al_2O_3 perovskite films with a well-controlled temperature ramp in a dry environment that the perovskite capping film coverage and the power conversion efficiency of block copolymer-directed alumina perovskite solar cells can be greatly improved. To the best of our knowledge, the crystalline precursor has not previously been described and its exact structure is currently unknown. We showed that the evolution between these structures markedly depends on the annealing conditions. A clear understanding of $CH_3NH_3PbX_3$ wet solution processing conditions in combination with bicontinuous BCP gyroidal titania electrodes[37,38] with an interconnecting pore network may allow complete perovskite infiltration, and enhance the photogenerated electron collection and transport for optimal solar cell performance.[24,32–34]

3.5 Methods

Materials

All materials were used as received. Anhydrous grades of toluene, n-butanol, tetrahydrofuran, chloroform, N,N-dimethylformamide and terpineol, 97% aluminum tri-sec-butoxide, >97% titanium isopropoxide, 20 wt% aluminum oxide nanoparticles in isopropanol (<50 nm, product number 702129), 57 wt% hydriodic acid in water, 33 wt% methylamine solution in ethanol, and lead chloride were obtained from Sigma-Aldrich. 70% nitric acid and 37% hydrochloric acid were obtained from Mallinckrodt Baker and EMD Millipore, respectively. 10 cP and 46 cP ethyl cellulose were obtained from TCI America.

Mesoporous block copolymer-directed alumina (MBCP-Al_2O_3) and titania (MBCP-TiO_2) films

MBCP-Al_2O_3 thin films were prepared using 50 mg of poly(isoprene)-block-poly(styrene)-block-poly(ethylene oxide) (ISO, Mn = 38.3 kg/mol, with a polydispersity index of 1.07 containing 68.4 wt% PI and 18.0 wt% PS) dissolved in 500 mg of toluene and n-butanol solvent mixture (1:1, w/w). In a separate vial, 104 mg of 97% aluminum tri-sec-butoxide, 478 mg of n-butanol and 478 mg of toluene were added sequentially. The white cloudy suspension was left undisturbed for 15 min, followed by vigorous stirring for 30 min to allow homogenization. 55 µL of 70% nitric acid was added and the mixture was stirred overnight (>12 h). The transparent alumina sol was added into the ISO solution and stirred for 45 min. The ISO-Al_2O_3 solution was processed by spin coating on silicon at 2000 rpm (45 sec) in a nitrogen drybox. The MBCP-Al_2O_3 hybrid thin films were baked at 50 °C (2 h), 100°C (2 h), and 130 °C (2 h) sequentially in the drybox, and calcined in a tube furnace at 450 °C (3 h) with a ramp rate of 1 °C/min.

MBCP-TiO_2 thin films were prepared using a modified method as described elsewhere.[38] Briefly, 50 mg of ISO was dissolved in 1.35 g of tetrahydrofuran and chloroform solvent mixture (4:5, w/w). In a separate vial, 53.9 µL of >97% titanium isopropoxide, 16.8 µL of 37% HCl acid, and 216 µL of tetrahydrofuran were mixed and stirred vigorously. The yellow-colored titania sol was added into the ISO solution

and stirred for 45 min. The ISO-TiO_2 solution was processed by spin coating on silicon at 2000 rpm (45 sec) in the drybox. The MBCP-TiO_2 hybrid thin films were baked at 50 °C (2 h), 100°C (2 h), and calcined in a tube furnace at 450 °C (3 h) with a ramp rate of 1 °C/min.

Mesoporous alumina nanoparticle (NP) films

Mesoporous Al_2O_3 nanoparticle (NP) thin films were prepared as described elsewhere.[18–20] The binder-free mesoporous Al_2O_3 NP film was prepared by spin coating 6.67 wt% Al_2O_3 NPs in isopropanol on silicon at 2500 rpm (60 sec), and baked at 150 °C (1 h). The 2 wt% Al_2O_3 NP-binder paste was prepared by mixing 1 g of Al_2O_3 NPs, 3.33 g terpineol, 1 g 10 cP ethyl cellulose and 1 g 46 cP ethyl cellulose in 43.67 g isopropanol. The mixture was stirred vigorously at 70 °C for 30 min. The mesoporous Al_2O_3 NP film with binder was prepared by spin coating the Al_2O_3 NP-binder mixture on silicon at 2500 rpm (60 sec), and calcined in a tube furnace at 500 °C (3 h) with a ramp rate of 1 °C/min.

Mesoporous alumina thin film characterization

Scanning electron microscopy (SEM) images were acquired on Au-Pd coated mesoporous alumina thin films using LEO 1550 and TESCAN MIRA3-LM field emission SEMs equipped with in-lens detectors. Atomic force microscopy (AFM) images were obtained on a Veeco Multimode II SPM with a Nanoscope III controller in tapping mode at ambient conditions. GISAXS was measured at the G1 beamline of the Cornell High Energy Synchrotron Source (CHESS). The G1 beamline setup consists of a multilayer monochromator of wavelength $\lambda = 0.1225$ nm with a CCD area detector with a 71.73 μm pixel size and a total of 1024 × 1024 pixels. The sample-to-detector distance was 2.745 m. The incident angle of the beam was varied between 0.1 ° and 0.3 ° with typical exposure times <2 sec. GISAXS patterns were analyzed with an in-house software[61] and the FIT2D program.[62]

Wide-angle X-ray scattering measurements of methylammonium lead tri-iodide/chloride hybrid perovskite

Methylammonium iodide (CH_3NH_3I) was prepared using 57 wt% hydriodic acid (HI) in water and 33 wt% methylamine solution (CH_3NH_2) in ethanol as reported

elsewhere.[18] 5-40 wt% of methylammonium iodide (CH_3NH_3I) and lead chloride ($PbCl_2$) (3:1 by molarity) dissolved in N,N-dimethylformamide was dispensed on the MBCP-Al_2O_3 and flat glass coverslip substrates by spin coating at 3000 rpm (45 sec) in air. For ex situ measurements, the hybrid perovskite samples were annealed by a slow temperature ramp of 10 °C / 10 min and held at 100 °C for 45 min in a nitrogen atmosphere. The annealed perovskite films were carefully scratched from the substrate and powdered for X-ray diffraction (XRD) analysis. The XRD characterization was performed on a Rigaku Ultima IV multipurpose X-ray diffraction system using Cu-Kα radiation (40 kV, 44 mA, wavelength λ = 1.5418 Å) and unit cell refinement analysis with the MDI Jade 9 software.

For in situ GIWAXS measurements, after spin coating the sample was immediately loaded on a temperature-controlled stage at the D1 beamline of CHESS. The D1 beamline setup consists of a multilayer monochromator of wavelength λ = 0.1161 nm. GIWAXS patterns were collected on Fuji image plates placed in a holder at a distance of 177 mm from the sample. The incident beam angle was above the silicon critical angle (~0.25 °) with exposure times <5 sec. The direct beam was blocked with lead tape. The exposed plates were scanned for digital processing with a GE Healthcare Typhoon FLA-7000 image plate reader. Digital images were analyzed using the FIT2D program.[62] The resolution of the letter-sized image plate is 2000 x 2500 pixels with a 100 μm pixel size. The measurements in nitrogen were conducted in a custom-made environmental chamber mounted on the temperature-controlled stage.[58]

Isothermal-time-dependent (ITD) perovskite crystallization

A 20 wt% precursor solution was dispensed on the MBCP-Al_2O_3 substrate by spin coating and immediately loaded on the temperature-stage held at 100 °C at the D1 beamline. GIWAXS measurements were taken at different time intervals over a dwell of 50 min. The measurements were conducted in ambient air and nitrogen.

Time-temperature-dependent (TTD) perovskite crystallization

A 20 wt% precursor solution was dispensed on the MBCP-Al_2O_3 substrate by spin coating and loaded on the temperature-stage held at 30 °C at the D1 beamline. The stage was slowly heated at a ramp rate of 10 °C / 10 min to the final temperature of 100 °C. The MBCP-Al_2O_3 perovskite sample was held at 100 °C for 60 min. The GIWAXS measurements were taken at different time intervals in nitrogen.

MBCP-Al_2O_3 hybrid perovskite solar cell assembly.

MBCP-Al_2O_3 perovskite solar cells (>20 cells for each annealing history) were fabricated as reported elsewhere.[18] Briefly, HCl-etched FTO glass substrates were coated with a dense TiO_2 compact layer prepared by spin coating a mildly HCl-acidified solution of titanium isopropoxide in ethanol, and sintered at 500 °C for 45 min. The MBCP-Al_2O_3 hybrid films were prepared by spin coating on the TiO_2/FTO substrates at 2000 rpm (45 sec). The substrates were baked at 50 °C (2 h), 100°C (2 h), and 130 °C (2 h) sequentially in the drybox and calcined at 450 °C (3 h) with a ramp rate of 1 °C/min.

A 40 wt% perovskite precursor solution was dispensed on the MBCP-Al_2O_3 scaffold by spin coating at 2000 rpm (45 sec). For the ITD-air processed MBCP-Al_2O_3 perovskite solar cells, the devices were fabricated in ambient air and heated in a conventional oven at 100 °C for 45 min. For the TTD-nitrogen processed MBCP-Al_2O_3 perovskite solar cells, the devices were fabricated in a nitrogen glovebox. After drying at ambient temperature for at least 20 min, the samples were slowly heated on a hotplate from ambient temperature to 100 °C at a ramp rate of 5 °C / 5 min, and held at 100 °C for 45 min. The electron blocking layer was formed by spin coating 80 mM 2,2',7,7'-tetrakis-(N,N-di-p-methoxyphenylamine)-9,9'-spirobifluorene (spiro-OMeTAD) in chlorobenzene solution with 68.3 mM tert-butylpyridine and 22.6 mM lithium bis(trifluoromethanesulfonyl)imide additives (170 mg/mL in acetonitrile) and aged overnight in a dessicator (in air). Silver contact electrodes of 150 nm were thermally evaporated to complete the devices.

MBCP-Al_2O_3 hybrid perovskite solar cell characterization

More than 20 solar cells were measured for each annealing condition (ITD versus TTD) with a Keithley 2400 under AM 1.5G 100 mW/cm^2 simulated sunlight (Abet Technologies Sun 2000) calibrated against an NREL certified KG5 filtered silicon reference diode. The cells were masked with a square aperture defining an active area of typically 0.07 cm^2 and measured in a light-tight sample holder.

3.6 References

(1) Cho, A. Energy's Tricky Tradeoffs. *Science* **2010**, *329*, 786–787.

(2) Graetzel, M.; Janssen, R. A. J.; Mitzi, D. B.; Sargent, E. H. Materials Interface Engineering for Solution-Processed Photovoltaics. *Nature* **2012**, *488*, 304–312.

(3) Ip, A. H.; Thon, S. M.; Hoogland, S.; Voznyy, O.; Zhitomirsky, D.; Debnath, R.; Levina, L.; Rollny, L. R.; Carey, G. H.; Fischer, A.; *et al.* Hybrid Passivated Colloidal Quantum Dot Solids. *Nat. Nanotechn.* **2012**, *7*, 577–582.

(4) Ning, Z.; Zhitomirsky, D.; Adinolfi, V.; Sutherland, B.; Xu, J.; Voznyy, O.; Maraghechi, P.; Lan, X.; Hoogland, S.; Ren, Y.; *et al.* Graded Doping for Enhanced Colloidal Quantum Dot Photovoltaics. *Adv. Mater.* **2013**, *25*, 1719–1723.

(5) Service, R. F. Outlook Brightens for Plastic Solar Cells. *Science* **2011**, *332*, 293–293.

(6) You, J.; Dou, L.; Yoshimura, K.; Kato, T.; Ohya, K.; Moriarty, T.; Emery, K.; Chen, C.-C.; Gao, J.; Li, G.; *et al.* A Polymer Tandem Solar Cell with 10.6% Power Conversion Efficiency. *Nat. Commun.* **2013**, *4*, 1446.

(7) Yella, A.; Lee, H.-W.; Tsao, H. N.; Yi, C.; Chandiran, A. K.; Nazeeruddin, M. K.; Diau, E. W.-G.; Yeh, C.-Y.; Zakeeruddin, S. M.; Grätzel, M. Porphyrin-Sensitized Solar Cells with Cobalt (II/III)–Based Redox Electrolyte Exceed 12 Percent Efficiency. *Science* **2011**, *334*, 629–634.

(8) Han, L.; Islam, A.; Chen, H.; Malapaka, C.; Chiranjeevi, B.; Zhang, S.; Yang, X.; Yanagida, M. High-Efficiency Dye-Sensitized Solar Cell with a Novel Co-Adsorbent. *Energy Environ. Sci.* **2012**, *5*, 6057–6060.

(9) Chung, I.; Lee, B.; He, J.; Chang, R. P. H.; Kanatzidis, M. G. All-Solid-State Dye-Sensitized Solar Cells with High Efficiency. *Nature* **2012**, *485*, 486–489.

(10) Kojima, A.; Teshima, K.; Shirai, Y.; Miyasaka, T. Organometal Halide Perovskites as Visible-Light Sensitizers for Photovoltaic Cells. *J. Am. Chem. Soc.* **2009**, *131*, 6050–6051.

(11) Im, J.-H.; Lee, C.-R.; Lee, J.-W.; Park, S.-W.; Park, N.-G. 6.5% Efficient Perovskite Quantum-Dot-Sensitized Solar Cell. *Nanoscale* **2011**, *3*, 4088–4093.

(12) Kim, H.-S.; Lee, C.-R.; Im, J.-H.; Lee, K.-B.; Moehl, T.; Marchioro, A.; Moon, S.-J.; Humphry-Baker, R.; Yum, J.-H.; Moser, J. E.; *et al.* Lead Iodide Perovskite Sensitized All-Solid-State Submicron Thin Film Mesoscopic Solar Cell with Efficiency Exceeding 9%. *Sci. Rep.* **2012**, *2*, 591.

(13) Noh, J. H.; Im, S. H.; Heo, J. H.; Mandal, T. N.; Seok, S. I. Chemical Management for Colorful, Efficient, and Stable Inorganic–Organic Hybrid Nanostructured Solar Cells. *Nano Lett.* **2013**, *13*, 1764–1769.

(14) Etgar, L.; Gao, P.; Xue, Z.; Peng, Q.; Chandiran, A. K.; Liu, B.; Nazeeruddin, M. K.; Grätzel, M. Mesoscopic $CH_3NH_3PbI_3/TiO_2$ Heterojunction Solar Cells. *J. Am. Chem. Soc.* **2012**, *134*, 17396–17399.

(15) Heo, J. H.; Im, S. H.; Noh, J. H.; Mandal, T. N.; Lim, C.-S.; Chang, J. A.; Lee, Y. H.; Kim, H.; Sarkar, A.; Nazeeruddin, M. K.; *et al.* Efficient Inorganic-Organic Hybrid Heterojunction Solar Cells Containing Perovskite Compound and Polymeric Hole Conductors. *Nat. Photonics* **2013**, *7*, 486–491.

(16) Crossland, E. J. W.; Noel, N.; Sivaram, V.; Leijtens, T.; Alexander-Webber, J. A.; Snaith, H. J. Mesoporous TiO_2 Single Crystals Delivering Enhanced Mobility and Optoelectronic Device Performance. *Nature* **2013**, *495*, 215–219.

(17) Kim, H.-S.; Mora-Sero, I.; Gonzalez-Pedro, V.; Fabregat-Santiago, F.; Juarez-Perez, E. J.; Park, N.-G.; Bisquert, J. Mechanism of Carrier Accumulation in Perovskite Thin-Absorber Solar Cells. *Nat. Commun.* **2013**, *4*, 2242.

(18) Lee, M. M.; Teuscher, J.; Miyasaka, T.; Murakami, T. N.; Snaith, H. J. Efficient Hybrid Solar Cells Based on Meso-Superstructured Organometal Halide Perovskites. *Science* **2012**, *338*, 643–647.

(19) Ball, J. M.; Lee, M. M.; Hey, A.; Snaith, H. J. Low-Temperature Processed Meso-Superstructured to Thin-Film Perovskite Solar Cells. *Energy Environ. Sci.* **2013**, *6*, 1739–1743.

(20) Edri, E.; Kirmayer, S.; Cahen, D.; Hodes, G. High Open-Circuit Voltage Solar Cells Based on Organic–Inorganic Lead Bromide Perovskite. *J. Phys. Chem. Lett.* **2013**, 897–902.

(21) Zhang, W.; Saliba, M.; Stranks, S. D.; Sun, Y.; Shi, X.; Wiesner, U.; Snaith, H. J. Enhancement of Perovskite-Based Solar Cells Employing Core–Shell Metal Nanoparticles. *Nano Lett.* **2013**, *13*, 4505–4510.

(22) Eperon, G. E.; Burlakov, V. M.; Docampo, P.; Goriely, A.; Snaith, H. J. Morphological Control for High Performance, Solution-Processed Planar Heterojunction Perovskite Solar Cells. *Adv. Funct. Mater.* **2014**, *24*, 151–157.

(23) Colella, S.; Mosconi, E.; Fedeli, P.; Listorti, A.; Gazza, F.; Orlandi, F.; Ferro, P.; Besagni, T.; Rizzo, A.; Calestani, G.; *et al.* $MAPbI_{3-x}Cl_x$ Mixed Halide Perovskite for Hybrid Solar Cells: The Role of Chloride as Dopant on the Transport and Structural Properties. *Chem. Mater.* **2013**, *25*, 4613–4618.

(24) Burschka, J.; Pellet, N.; Moon, S.-J.; Humphry-Baker, R.; Gao, P.; Nazeeruddin, M. K.; Grätzel, M. Sequential Deposition as a Route to High-Performance Perovskite-Sensitized Solar Cells. *Nature* **2013**, *499*, 316–319.

(25) Liu, M.; Johnston, M. B.; Snaith, H. J. Efficient Planar Heterojunction Perovskite Solar Cells by Vapour Deposition. *Nature* **2013**, *501*, 395–398.

(26) Conings, B.; Baeten, L.; De Dobbelaere, C.; D'Haen, J.; Manca, J.; Boyen, H.-G. Perovskite-Based Hybrid Solar Cells Exceeding 10% Efficiency with High Reproducibility Using a Thin Film Sandwich Approach. *Adv. Mater.* **2013** [Early View]. DOI: 10.1002/adma.201304803. Published online: December 12, 2013.

(27) Jeng, J.-Y.; Chiang, Y.-F.; Lee, M.-H.; Peng, S.-R.; Guo, T.-F.; Chen, P.; Wen, T.-C. $CH_3NH_3PbI_3$ Perovskite/Fullerene Planar-Heterojunction Hybrid Solar Cells. *Adv. Mater.* **2013**, *25*, 3727–3732.

(28) Stranks, S. D.; Eperon, G. E.; Grancini, G.; Menelaou, C.; Alcocer, M. J. P.; Leijtens, T.; Herz, L. M.; Petrozza, A.; Snaith, H. J. Electron-Hole Diffusion Lengths Exceeding 1 Micrometer in an Organometal Trihalide Perovskite Absorber. *Science* **2013**, *342*, 341–344.

(29) Xing, G.; Mathews, N.; Sun, S.; Lim, S. S.; Lam, Y. M.; Grätzel, M.; Mhaisalkar, S.; Sum, T. C. Long-Range Balanced Electron- and Hole-Transport Lengths in Organic-Inorganic $CH_3NH_3PbI_3$. *Science* **2013**, *342*, 344–347.

(30) Liu, D.; Kelly, T. L. Perovskite Solar Cells with a Planar Heterojunction Structure Prepared Using Room-Temperature Solution Processing Techniques. *Nat. Photonics* **2014**, *8*, 133–138.

(31) You, J.; Hong, Z.; Yang, Y. (Michael); Chen, Q.; Cai, M.; Song, T.-B.; Chen, C.-C.; Lu, S.; Liu, Y.; Zhou, H.; *et al.* Low-Temperature Solution-Processed Perovskite Solar Cells with High Efficiency and Flexibility. *ACS Nano* **2014**, *8*, 1674–1680.

(32) Edri, E.; Kirmayer, S.; Henning, A.; Mukhopadhyay, S.; Gartsman, K.; Rosenwaks, Y.; Hodes, G.; Cahen, D. Why Lead Methylammonium Tri-Iodide Perovskite-Based Solar Cells Require a Mesoporous Electron Transporting Scaffold (but Not Necessarily a Hole Conductor). *Nano Lett.* **2014**, *14*, 1000–1004.

(33) Gonzalez-Pedro, V.; Juarez-Perez, E. J.; Arsyad, W.-S.; Barea, E. M.; Fabregat-Santiago, F.; Mora-Sero, I.; Bisquert, J. General Working Principles of $CH_3NH_3PbX_3$ Perovskite Solar Cells. *Nano Lett.* **2014**, *14*, 888–893.

(34) Marchioro, A.; Teuscher, J.; Friedrich, D.; Kunst, M.; van de Krol, R.; Moehl, T.; Grätzel, M.; Moser, J.-E. Unravelling the Mechanism of Photoinduced Charge Transfer Processes in Lead Iodide Perovskite Solar Cells. *Nat. Photonics* **2014**, 8, 250-255.

(35) Kagan, C. R.; Mitzi, D. B.; Dimitrakopoulos, C. D. Organic-Inorganic Hybrid Materials as Semiconducting Channels in Thin-Film Field-Effect Transistors. *Science* **1999**, *286*, 945–947.

(36) Mitzi, D. B.; Chondroudis, K.; Kagan, C. R. Organic-Inorganic Electronics. *IBM J. Res. Dev.* **2001**, *45*, 29–45.

(37) Crossland, E. J. W.; Kamperman, M.; Nedelcu, M.; Ducati, C.; Wiesner, U.; Smilgies, D.-M.; Toombes, G. E. S.; Hillmyer, M. A.; Ludwigs, S.; Steiner, U.; *et al.* A Bicontinuous Double Gyroid Hybrid Solar Cell. *Nano Lett.* **2009**, *9*, 2807–2812.

(38) Docampo, P.; Stefik, M.; Guldin, S.; Gunning, R.; Yufa, N. A.; Cai, N.; Wang, P.; Steiner, U.; Wiesner, U.; Snaith, H. J. Triblock-Terpolymer-Directed Self-Assembly of Mesoporous TiO_2: High-Performance Photoanodes for Solid-State Dye-Sensitized Solar Cells. *Adv. Energy Mater.* **2012**, *2*, 676–682.

(39) Polman, A.; Atwater, H. A. Photonic Design Principles for Ultrahigh-Efficiency Photovoltaics. *Nat. Mater.* **2012**, *11*, 174–177.

(40) Lunt, R. R.; Osedach, T. P.; Brown, P. R.; Rowehl, J. A.; Bulović, V. Practical Roadmap and Limits to Nanostructured Photovoltaics. *Adv. Mater.* **2011**, *23*, 5712–5727.

(41) Orilall, M. C.; Wiesner, U. Block Copolymer Based Composition and Morphology Control in Nanostructured Hybrid Materials for Energy Conversion and Storage: Solar Cells, Batteries, and Fuel Cells. *Chem. Soc. Rev.* **2011**, *40*, 520–535.

(42) Templin, M.; Franck, A.; Chesne, A. D.; Leist, H.; Zhang, Y.; Ulrich, R.; Schädler, V.; Wiesner, U. Organically Modified Aluminosilicate Mesostructures from Block Copolymer Phases. *Science* **1997**, *278*, 1795–1798.

(43) Guo, C.; Lin, Y.-H.; Witman, M. D.; Smith, K. A.; Wang, C.; Hexemer, A.; Strzalka, J.; Gomez, E. D.; Verduzco, R. Conjugated Block Copolymer Photovoltaics with near 3% Efficiency through Microphase Separation. *Nano Lett.* **2013**, *13*, 2957–2963.

(44) Kuemmel, M.; Grosso, D.; Boissière, C.; Smarsly, B.; Brezesinski, T.; Albouy, P. A.; Amenitsch, H.; Sanchez, C. Thermally Stable Nanocrystalline γ-Alumina Layers with Highly Ordered 3D Mesoporosity. *Angew. Chem. Int. Ed.* **2005**, *44*, 4589–4592.

(45) Oveisi, H.; Jiang, X.; Imura, M.; Nemoto, Y.; Sakamoto, Y.; Yamauchi, Y. A Mesoporous γ-Alumina Film with Vertical Mesoporosity: The Unusual Conversion from a $Im\bar{3}m$ Mesostructure to Vertically Oriented γ-Alumina Nanowires. *Angew. Chem. Int. Ed.* **2011**, *50*, 7410–7413.

(46) Jiang, X.; Suzuki, N.; Bastakoti, B. P.; Wu, K. C.-W.; Yamauchi, Y. Synthesis of Continuous Mesoporous Alumina Films with Large-Sized Cage-Type Mesopores by Using Diblock Copolymers. *Chem. Asian J.* **2012**, *7*, 1713–1718.

(47) Guldin, S.; Kolle, M.; Stefik, M.; Langford, R.; Eder, D.; Wiesner, U.; Steiner, U. Tunable Mesoporous Bragg Reflectors Based on Block-Copolymer Self-Assembly. *Adv. Mater.* **2011**, *23*, 3664–3668.

(48) Rauda, I. E.; Buonsanti, R.; Saldarriaga-Lopez, L. C.; Benjauthrit, K.; Schelhas, L. T.; Stefik, M.; Augustyn, V.; Ko, J.; Dunn, B.; Wiesner, U.; *et al.* General Method for the Synthesis of Hierarchical Nanocrystal-Based Mesoporous Materials. *ACS Nano* **2012**, *6*, 6386–6399.

(49) Buonsanti, R.; Pick, T. E.; Krins, N.; Richardson, T. J.; Helms, B. A.; Milliron, D. J. Assembly of Ligand-Stripped Nanocrystals into Precisely Controlled Mesoporous Architectures. *Nano Lett.* **2012**, *12*, 3872–3877.

(50) Nedelcu, M.; Lee, J.; Crossland, E. J. W.; Warren, S. C.; Orilall, M. C.; Guldin, S.; Hüttner, S.; Ducati, C.; Eder, D.; Wiesner, U.; *et al.* Block Copolymer Directed Synthesis of Mesoporous TiO_2 for Dye-Sensitized Solar Cells. *Soft Matter* **2009**, *5*, 134–139.

(51) Arora, H.; Du, P.; Tan, K. W.; Hyun, J. K.; Grazul, J.; Xin, H. L.; Muller, D. A.; Thompson, M. O.; Wiesner, U. Block Copolymer Self-Assembly–Directed Single-Crystal Homo- and Heteroepitaxial Nanostructures. *Science* **2010**, *330*, 214–219.

(52) Guldin, S.; Hüttner, S.; Tiwana, P.; Orilall, M. C.; Ülgüt, B.; Stefik, M.; Docampo, P.; Kolle, M.; Divitini, G.; Ducati, C.; *et al.* Improved Conductivity in Dye-Sensitised Solar Cells through Block-Copolymer Confined TiO_2 Crystallisation. *Energy Environ. Sci.* **2010**, *4*, 225–233.

(53) Hur, K.; Francescato, Y.; Giannini, V.; Maier, S. A.; Hennig, R. G.; Wiesner, U. Three-Dimensionally Isotropic Negative Refractive Index Materials from Block Copolymer Self-Assembled Chiral Gyroid Networks. *Angew. Chem. Int. Ed.* **2011**, *50*, 11985–11989.

(54) Baikie, T.; Fang, Y.; Kadro, J. M.; Schreyer, M.; Wei, F.; Mhaisalkar, S. G.; Graetzel, M.; White, T. J. Synthesis and Crystal Chemistry of the Hybrid Perovskite $(CH_3NH_3)PbI_3$ for Solid-State Sensitised Solar Cell Applications. *J. Mater. Chem. A* **2013**, *1*, 5628–5641.

(55) Poglitsch, A.; Weber, D. Dynamic Disorder in Methylammoniumtri-halogenoplumbates (II) Observed by Millimeter□wave Spectroscopy. *J. Chem. Phys.* **1987**, 87, 6373–6378.

(56) Stoumpos, C. C.; Malliakas, C. D.; Kanatzidis, M. G. Semiconducting Tin and Lead Iodide Perovskites with Organic Cations: Phase Transitions, High

Mobilities, and Near-Infrared Photoluminescent Properties. *Inorg. Chem.* **2013**, *52*, 9019–9038.

(57) Busch, P.; Rauscher, M.; Smilgies, D.-M.; Posselt, D.; Papadakis, C. M. Grazing-Incidence Small-Angle X-Ray Scattering from Thin Polymer Films with Lamellar Structures – the Scattering Cross Section in the Distorted-Wave Born Approximation. *J. Appl. Crystallogr.* **2006**, *39*, 433–442.

(58) Bian, K.; Choi, J. J.; Kaushik, A.; Clancy, P.; Smilgies, D.-M.; Hanrath, T. Shape-Anisotropy Driven Symmetry Transformations in Nanocrystal Superlattice Polymorphs. *ACS Nano* **2011**, *5*, 2815–2823.

(59) D. Yoreo, J.; Vekilov, P. G. Principles of Crystal Nucleation and Growth. In *Biomineralization*; Dove, P. M.; De Yoreo, J.; Weiner, S.; Mineralogical Society of America: Washington, DC, 2003; Vol. 54, pp 57-93.

(60) Vekilov, P. G. Nucleation. *Cryst. Growth Des.* **2010**, *10*, 5007–5019.

(61) Smilgies, D.-M.; Blasini, D. R. Indexation Scheme for Oriented Molecular Thin Films Studied with Grazing-Incidence Reciprocal-Space Mapping. *J. Appl. Crystallogr.* **2007**, *40*, 716–718.

(62) Hammersley, A. P.; Svensson, S. O.; Hanfland, M.; Fitch, A. N.; Hausermann, D. Two-Dimensional Detector Software: From Real Detector to Idealised Image or Two-Theta Scan. *High Pressure Res.* **1996**, *14*, 235–248.

3.7 Supporting Information

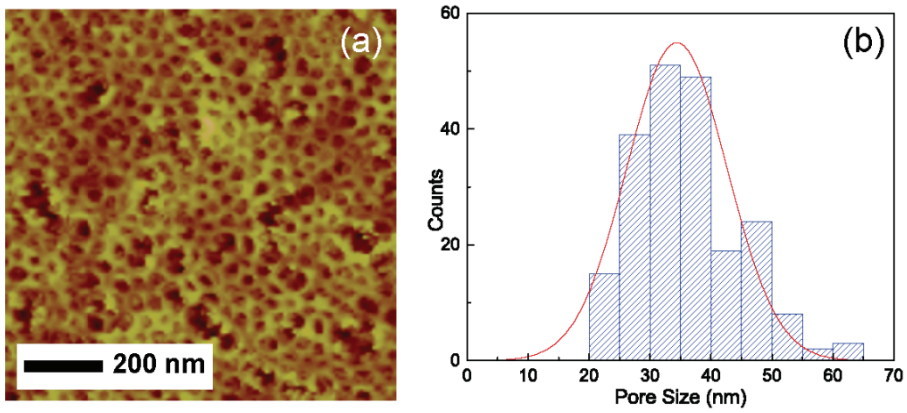

Figure 3.6: (a) AFM surface profile of the MBCP-Al_2O_3 film. (b) Histogram of the MBCP-Al_2O_3 pore size distribution. A Gaussian fitting curve is added to guide the eye.

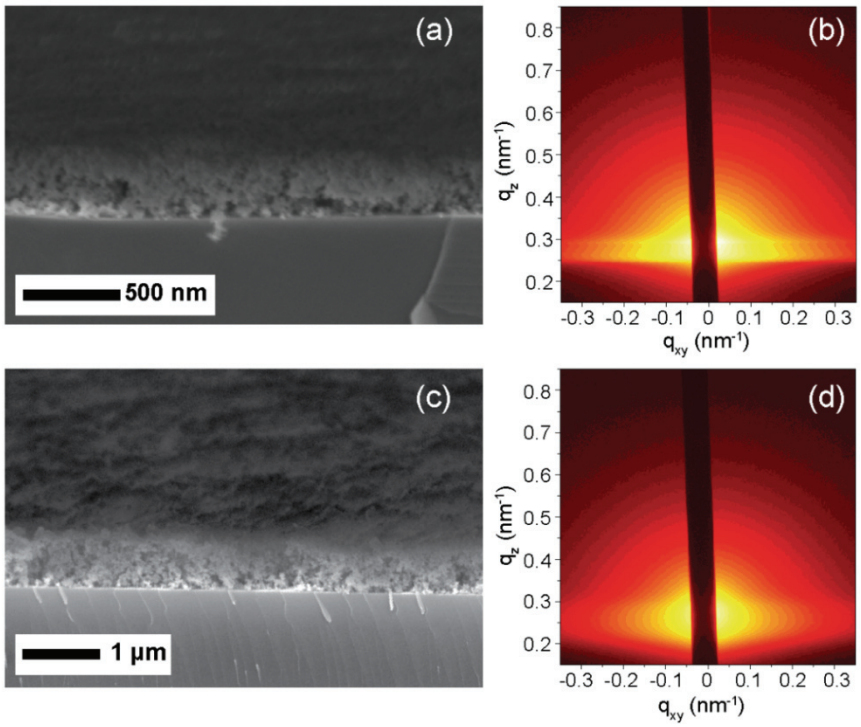

Figure 3.7: Cross-sectional SEM micrographs and GISAXS profiles of (a, b) binder-free Al_2O_3 and (c, d) Al_2O_3 with binder nanoparticulate (NP) films measured at incidence angle of 0.18 °. The in-plane porosity in the Al_2O_3 NP films is macroscopically inhomogeneous.

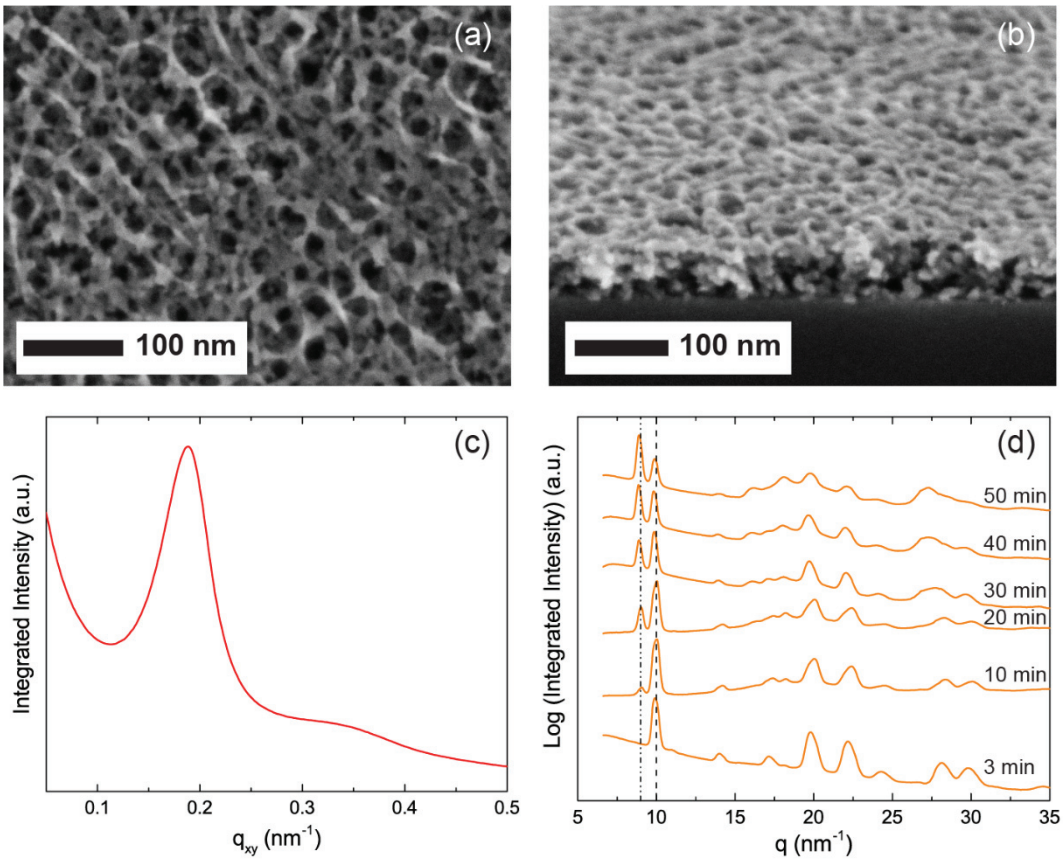

Figure 3.8: (a) Plan view and (b) cross-sectional SEM micrographs of MBCP-TiO_2 film. (c) Integrated intensity plot of GISAXS profile of MBCP-TiO_2 measured at an incidence angle of 0.16 °. The first scattering peak at q_{xy} = 0.189 nm^{-1} provides a macroscopically homogeneous in-plane d-spacing of $2\pi/q_{xy} \approx 33$ nm. (d) *In situ* GIWAXS azimuthally integrated intensity plots of $CH_3NH_3PbI_{3-x}Cl_x$ perovskite on MBCP-TiO_2 as observed under ITD annealing at 100 °C in air.

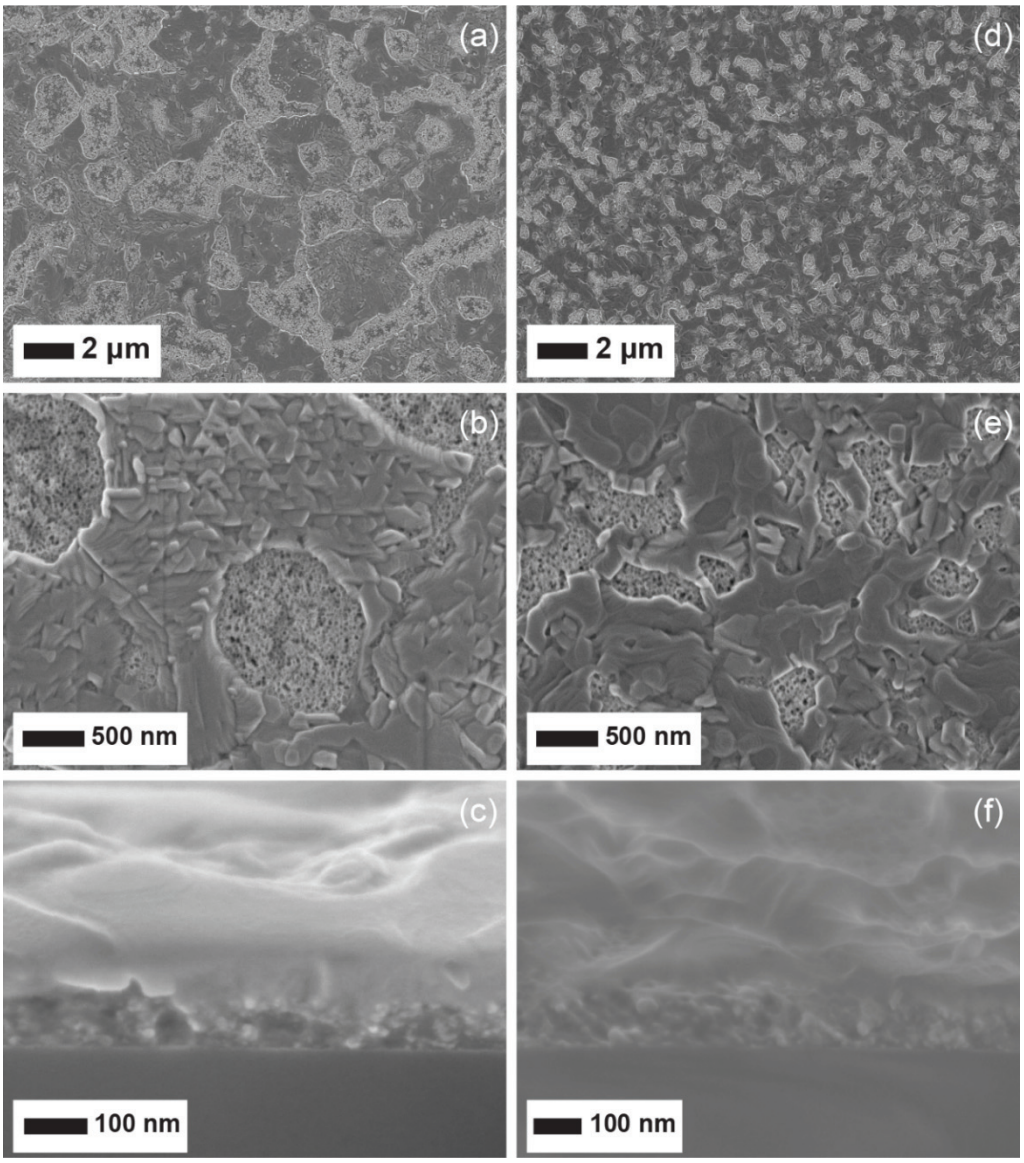

Figure 3.9: Plan view and cross-sectional SEM micrographs of 20 wt% perovskite on MBCP-Al_2O_3 prepared by (a-c) ITD (100 °C for 45 min), and (d-f) TTD (5 °C / 5 min ramp rate, 100 °C for 45 min) annealing in nitrogen. Large perovskite crystallite islands and pore regions were observed for the ITD annealed MBCP-Al_2O_3 perovskite films compared to the TTD annealed samples.

Table 3.1: MBCP-Al_2O_3 perovskite solar cell performance parameters averaged over a batch of at least 20 devices measured under 100 mW/cm^2 stimulated AM1.5 sunlight irradiation.

	Short-circuit density current (mA/cm^2)	Open-circuit voltage (V)	Fill factor	Power conversion efficiency (%)
ITD-annealed in air	13.7 ± 1.7	0.73 ± 0.08	0.36 ± 0.06	3.6 ± 1.0
TTD-annealed in N_2	15.7 ± 2.9	0.94 ± 0.02	0.44 ± 0.05	6.3 ± 1.2

CHAPTER 4

IMPACT OF THE ORGANIC HALIDE SALT ON FINAL PEROVSKITE COMPOSITION FOR PHOTOVOLTAIC APPLICATIONS

4.1 Abstract

The methylammonium lead halide perovskites have shown significant promise as a low-cost, second generation, photovoltaic material. Despite recent advances, however, there are still a number of fundamental aspects of their formation as well as their physical and electronic behavior that are not well understood. In this letter we explore the mechanism by which these materials crystallize by testing the outcome of each of the reagent halide salts. We find that components of both salts, lead halide and methylammonium halide, are relatively mobile and can be readily exchanged during the crystallization process when the reaction is carried out in solution or in the solid state. We exploit this fact by showing that the perovskite structure is formed even when the lead salt's anion is a non-halide, leading to lower annealing temperature and time requirements for film formation. Studies into these behaviors may ultimately lead to improved processing conditions for photovoltaic films.

4.2 Introduction

For many crystalline semiconductors, the ability to grow large, oriented grains is essential for high performance. This ability is enabled, in part, by a fundamental understanding of the mechanisms by which the crystal forms. The methylammonium lead halide perovskites ($MAPbX_3$, where $MA=NH_3CH_3^+$, $X=I^-$ or Cl^-) have recently shown great promise as a class of photovoltaic materials that can yield high efficiency devices using low cost processing methods.[1-21] Power conversion efficiencies of these devices are enhanced by the control of perovskite film coverage and crystallinity.[12,17,19–24] We have previously reported three stages of structural evolution in the perovskite formation via a one-step solution-processing route: an unidentified crystalline precursor structure, the perovskite structure, and decomposition products.[23] Specifically the transition from the precursor structure to the perovskite structure is

intriguing since it indicates a solid-state transformation. In this letter we show that the perovskite structure forms via complete dissociation and rearrangement of all reagent halide salts under both solution and solid state conditions. Based on this knowledge we explore alternative synthetic routes with the ultimate goal of finding more favorable processing conditions for the formation of the desired perovskite structure.

4.3 Results and Discussion

The formation of thin films of $MAPbX_3$ can be accomplished through several processing routes as shown schematically in Figure 4.1. Various groups have reported a one-step deposition method (Fig. 4.1a) that consists of mixing a lead halide salt (PbX_2, X=I^-, Cl^-) and a methylammonium halide salt (MAX, X=I^-, Cl^-) in a common solvent and depositing the solution on a substrate. Upon thermal annealing, the solvent is removed and the perovskite structure is formed.[3,4,9,14,15,17,20,22–29] A common pathway for this type of crystallization from solution is by the rearrangement of constituent ions; however, for solid-state transitions there are other viable pathways to consider, such as the topotactic transformation of one or more of the constituent salts.[30–35] Determining the pathway by which the perovskite forms has implications both in terms of potential processing conditions, as well as providing a means by which the role of other components, such as spectator species, can be explored.

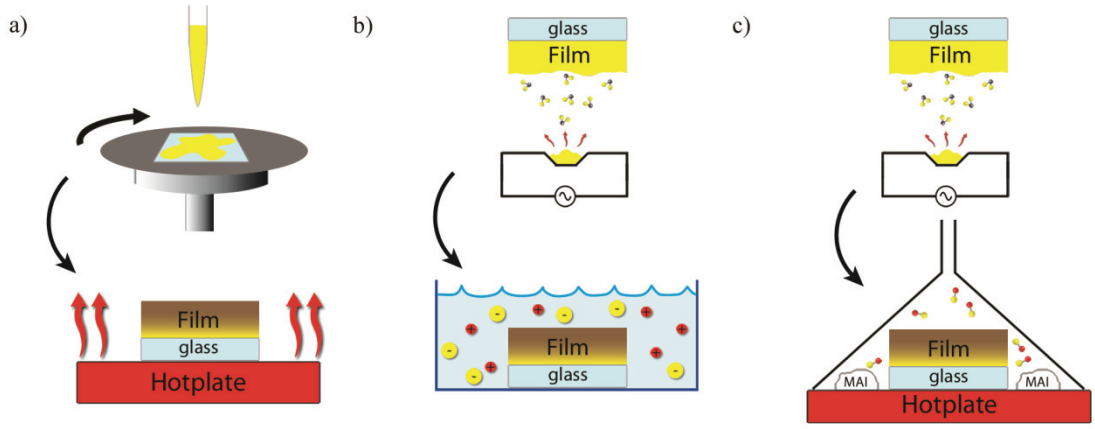

Figure 4.1: Schematic of perovskite thin film processing pathways: a) One-step solution deposition from both halide salts in a common solvent via spin coating followed by thermal annealing; b) Two-step process by soaking a thermally evaporated film of lead halide in a solution of MA halide dissolved in an anti-solvent for the perovskite; c) Two-step process using a thermally evaporated film of lead halide followed by sublimation of the MA halide salt.

In order to decouple the disposition of the reagent salts, we adopted a two-step process,[12] in which we deposited the lead salt by thermal evaporation followed by soaking the films in a solution of methylammonium halides dissolved in isopropanol (Fig. 4.1b). Due to the minimal solubility of lead halides in isopropanol, this processing route has the lead halide in the solid state during the crystallization; it is important to note the solubility of the resulting perovskite is negligible in IPA but quite high in water mandating the use of a water free environments for this experimental path. We varied the deposited lead halide species and the molar ratios of the methylammonium halides (MAI and MACl) as summarized in Table 4.1. We note that given the lead salt film thickness and the volume of solution used, there is an approximately 3,000-fold excess of methylammonium halide in the solution compared to the lead halide on the substrate, leaving lead as the only limiting reagent in the reaction. Preliminary experiments on thin lead halide films (25-100 nm) showed that delamination from the substrate occurred prior to complete formation of the perovskite. To mitigate this effect, 1 μm thick lead halide films were used, thereby simultaneously avoiding delamination and ensuring thick enough perovskite layers for characterization. In order to maintain the structure, as formed in the thin film, without excluding structural elements due to texturing, we performed grazing incidence wide-angle X-ray scattering (GIWAXS) directly on those films. Figure 4.2 shows the azimuthally integrated intensity plots of the resulting two-dimensional (2D) data sets. Previous studies, including EDX[25] and XPS[15], have shown that Cl can only be incorporated into the iodide structure at very low concentrations; additionally, for the mixed halide systems that do form a continuous solid solution (I/Br and Cl/Br)[3,36] there is a systematic shift in both the lattice parameter and the optical band gap. Given these facts we used the x-ray patterns and/or absorption data to determine the primary structure formed; although this does not determine the purity of the structure, small inclusions of the secondary halide do not impact the assessment of the extent of the dissociation/rearrangement of the reagent salts. As summarized in Table 4.1, the scattering patterns reveal that the final perovskite structure contains the halide species dominant in the solution, regardless of the starting lead halide film. This result

suggests that the lead halide needs to dissociate and exchange freely with the methylammonium halide ions during the process of the perovskite formation. Based on the observed behavior of ion rearrangement, as well as results of an earlier study in which we reported the existence of a structurally unidentified precursor phase prior to the perovskite,[23] it is clear that the pathway of the system to the final perovskite structure is rather complex and deserves further study.

Table 4.1: Experimental parameters of $MAPbX_3$ perovskite formation studies.

Sample Label	Lead Halide[a]	[MAI] / mM[b]	[MACl] / mM[b]	Perovskite Formed[c]
I-120	PbI_2	120	0	$MAPbI_n$
C-120	$PbCl_2$	120	0	$MAPbI_n$
I-80	PbI_2	80	40	$MAPbI_n$
C-80	$PbCl_2$	80	40	$MAPbI_n$
I-40	PbI_2	40	80	$MAPbCl_n$
C-40	$PbCl_2$	40	80	$MAPbCl_n$
I-0	PbI_2	0	120	$MAPbCl_n$
C-0	$PbCl_2$	0	120	$MAPbCl_n$

(a) 1 μm thick lead salt films were thermally evaporated.
(b) MA halide solutions were prepared in isopropyl alcohol.
(c) $MAPbX_n$ denotes $MAPbX_{3-m}Y_m$ where $m<<1$.

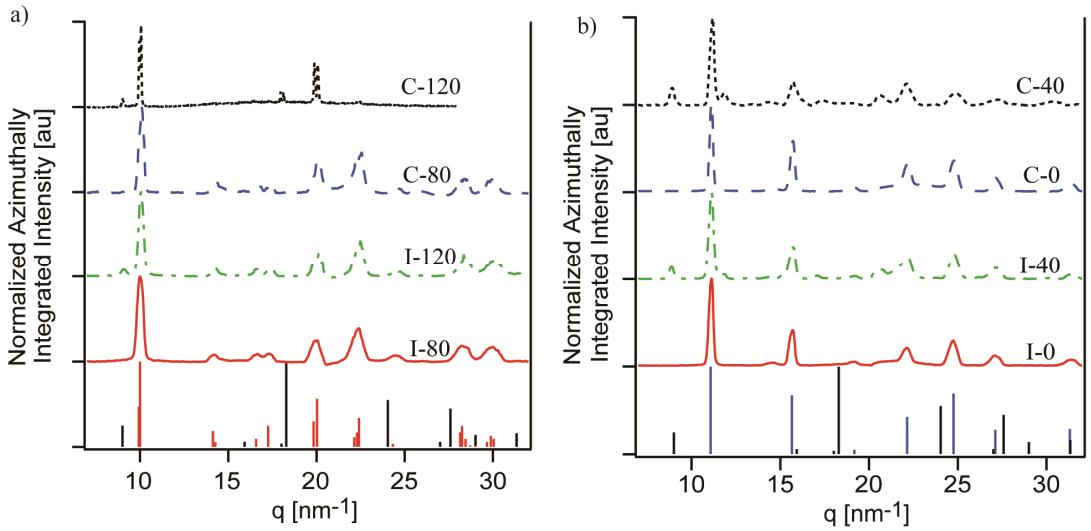

Figure 4.2: Azimuthally integrated GIWAXS data, for evaporated lead halide films soaked in various methylammonium halide solutions, plotted against the scattering vector q, where $q = 4\pi\sin\theta/\lambda$. (a) Films in which MAI was in higher concentration and (b) films in which MACl was in higher concentration. Stick markers at the bottom of the plots indicate calculated peak locations for the tetragonal iodide perovskite (red),[36] the cubic chloride perovskite (blue),[37] and lead iodide (black).[38] Note: Sample C-120 was damaged prior to GIWAXS collection; the data shown is a 2-theta scan of an equivalently prepared film.

We note that the crystallization times and crystal morphologies vary with the lead halide source. For lead chloride films the soaking time required to obtain the perovskite was 4 hours, compared to 2 hours for the lead iodide films. SEM and 2D GIWAXS data (see Supplementary Materials)[39] show that lead iodide films lead to perovskite structures with much smaller crystals, better coverage, and a higher degree of crystallographic orientation. The most highly textured films, based on the GIWAXS data, are samples I-120 and I-80, both of which start with PbI_2 and transform to $MAPbI_3$ (Fig. 4.5a,c).[39] From the SEM image (Fig. 4.6a)[39] of I-80 this texture appears to be the result of the homogeneity of both the size and shape of the crystallites, which leads to better packing and orientational order of the individual grains. The slower growth of the corresponding $PbCl_2$ sample, C-80, leads to crystals that are larger and more polydisperse in both size and shape. The SEM image (Fig. 4.6b)[39] shows sparse coverage and a random orientation of the individual crystals, causing a less textured scattering pattern (Fig. 4.5d).[39]

We next turned our attention to the outcome of the MA salt and the question of whether the individual ions of the MA halide stay associated or not. The reverse version of the above soaking experiment, *i.e.* soaking solid state MAX films in PbX_2 solutions, is impractical as the lead halides are only appreciably soluble in solvents that will also solvate the perovskite. However, we can explore the disposition of the MA salt in the solid state by using a two-step sublimation process similar to that reported by Chen *et al.*[19] in which the lead salt is deposited first and the MA salt introduced by sublimation. For many ionic salts, specifically ammonium salts, it has been shown that sublimation at lower temperatures produces molecular units in the vapor phase as opposed to dissociated ions.[40,41] We therefore assume that the sublimed species is e.g. molecular MAI which then condenses onto the lead salt film followed by the crystallization of the perovskite. This process is a solid state reaction with no background solvent present. Thin films (~50 nm) of lead chloride were first evaporated onto glass substrates. The films were placed on a hotplate at 150 ºC, together with a small volume of MAI salt and covered with a funnel to allow for saturation with MAI vapor (see Fig. 4.1c). The films began to turn brown at the edges in ~1 hour and were completely brown after 7 hours. Comparison of the XRD spectrum (Fig. 4.3) to the known peak positions for $MAPbI_3$ confirm that the iodide perovskite structure was formed. The inset of Figure 4.3 presents the absorption spectrum of the final film, exhibiting a band gap also consistent with the iodide perovskite.[2,3] Given that the lead halide was $PbCl_2$, the stoichiometry dictates that the MAI must have dissociated to form the resulting perovskite. The results therefore suggest that all ions dissociate, not only when the reaction is performed in solution, but also when both salts are present in the solid state, with no solvent present.

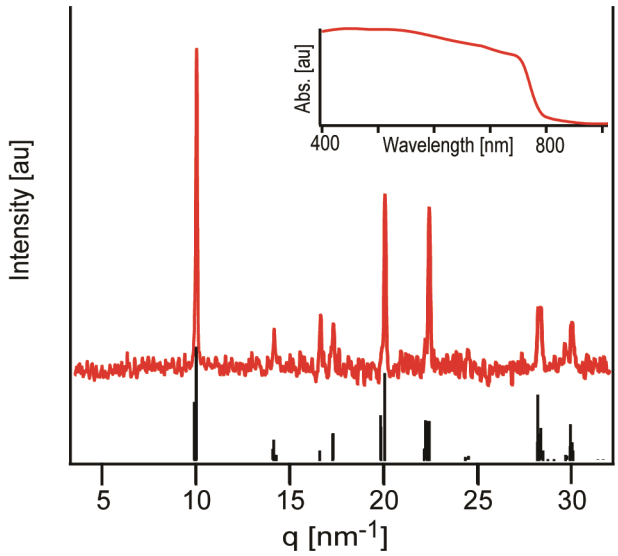

Figure 4.3: XRD pattern (red) of evaporated $PbCl_2$ thin film transformed by sublimation of MAI at 150 ºC; stick markers (black) indicate expected peak positions for the iodide perovskite. Inset shows the absorbance spectrum of the same film.

The crystallization pathway reported here raises several interesting questions. These questions include, among others: Are there possible routes to templating the crystal growth via the individual, constituent ions? Does this pathway help elucidate the role of spectator species in mediating the dissociation of the reagents? How sensitive is the formation of the final perovskite to the source of the constituent ions? We explore one of these ideas as further validation of our findings and to demonstrate the application of these results to finding alternative processing pathways. If the lead cation loses all association with its corresponding anions during the crystallization process, then the crystallization should be insensitive to the lead source. To verify the insensitivity to the lead counter-ions and to test the impact of the lead source on processing conditions, we prepared a film using lead nitrate, $Pb(NO_3)_2$, a non-halide lead source. A 40 wt% solution of $Pb(NO_3)_2$ and MAI in a 1:3 stoichiometric ratio was prepared in *N,N*-dimethylformamide (DMF) and spin-cast onto a glass substrate at 2500 rpm for 45 seconds. After spin-casting, the substrate was placed on a hotplate and ramped from room temperature to 100 ºC at 1 ºC/min. These are the same conditions that we have previously reported for the mixed halide of $PbCl_2$:MAI in DMF,[22,23] except that in the mixed halide system the total post-deposition treatment

consisted of the ramp to 100 ºC followed by 45 minutes of annealing at that temperature. In our tests with $Pb(NO_3)_2$-based solutions, the films turned brown at ~20 minutes into the temperature ramp, corresponding to a temperature of only 45 ºC.

Figure 4.4 shows the XRD pattern, absorption data and optical images of perovskite films with $Pb(NO_3)_2$ as the lead source. The x-ray diffraction and absorbance data (Fig. 4.4a) confirm that $MAPbI_3$ is formed. The faster formation of the perovskite at lower temperatures is likely the result of the spectator species, $MANO_3$, the excess component that exists as a result of the non-stoichiometric reagents in solution. In the mixed halide system used by several groups,[15,17,24,25,42] with $PbCl_2$:MAI in a 1:3 ratio, the excess component is MACl (m.p.≈230 ºC), which is less volatile then $MANO_3$ (m.p.≈110 ºC). Although the relationship between volatility and lower annealing temperatures is unclear, it does provide potential alternate processing paths, such as spray coating. The optical images in Fig. 4.4b-d were taken from spray coated films prepared in identical ways at different times. These micrographs reveal two important features: (1) a high sensitivity of the resulting film morphology to subtle changes in the growth conditions like environmental humidity, which was not controlled in these experiments; (2) the various morphologies that can be achieved, including spherulites (4b), dendrites (4c) and large faceted crystals (4d). Because the annealing temperature was well below that used for films made from $PbCl_2$ (in which the excess salt has been reported to be removed by sublimation during annealing)[20] we checked to ensure that the excess salt ($MANO_3$) was completely removed. To that end additional films were made and the presence of NO_3 probed by FTIR, after which the films were soaked for 3 minutes in IPA, then rinsed thoroughly with IPA, and probed again. The resulting spectra (Supplementary Materials, Figure 4.7)[39] show that NO_3 is still present in the films after annealing but that it is completely removed by washing. These results suggest that crystallization of the perovskite can occur in the presence of excess organic salt.

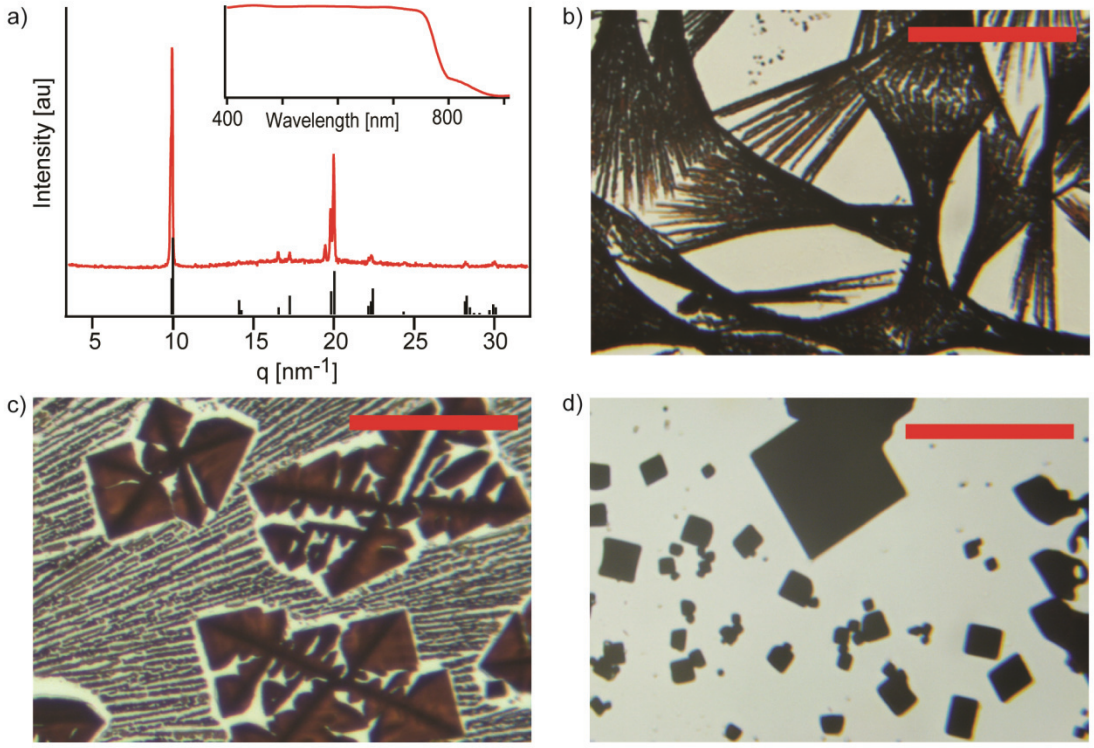

Figure 4.4: Characterization of perovskite films with $Pb(NO_3)_2$ as the Pb source. a) XRD pattern and absorbance spectrum (inset) of the spin coated film. Vertical markers (black) indicate expected peak positions of the iodide perovskite. b-d) Optical micrographs of spray coated films. Scale bars in all images are 50 μm.

4.4 Conclusions

In conclusion, we have probed the disposition of both reagent salts used in the processing of $MAPbX_3$ thin films and showed that the crystallization occurs via rearrangement of all constituent ions, irrespective of whether the reaction is performed in solution or in the solid state. We have noted several implications of this crystallization mechanism and demonstrated that one of those, the choice of the lead counter-ion, can be exploited to effect the annealing time and temperature necessary to form the final product. The results suggest that fundamental materials research as shown here, targeted at understanding the crystallization mechanisms, may ultimately help elucidate improved processing conditions leading to thin films of perovskites with optimized crystal size and orientation, which, in turn, may give rise to enhanced opto-electronic properties.

4.5 References

1 M.M. Lee, J. Teuscher, T. Miyasaka, T.N. Murakami, and H.J. Snaith, Science **338**, 643 (2012).

2 H.-S. Kim, C.-R. Lee, J.-H. Im, K.-B. Lee, T. Moehl, A. Marchioro, S.-J. Moon, R. Humphry-Baker, J.-H. Yum, J.E. Moser, M. Grätzel, and N.-G. Park, Sci. Rep. **2**, 591 (2012).

3 J.H. Noh, S.H. Im, J.H. Heo, T.N. Mandal, and S. Il Seok, Nano Lett. **13**, 1764 (2013).

4 L. Etgar, P. Gao, Z. Xue, Q. Peng, A.K. Chandiran, B. Liu, M.K. Nazeeruddin, and M. Grätzel, J. Am. Chem. Soc. **134**, 17396 (2012).

5 I. Chung, B. Lee, J. He, R.P.H. Chang, and M.G. Kanatzidis, Nature **485**, 486 (2012).

6 J. Qiu, Y. Qiu, K. Yan, M. Zhong, C. Mu, H. Yan, and S. Yang, Nanoscale **5**, 3245 (2013).

7 O. Malinkiewicz, A. Yella, Y.H. Lee, G.M. Espallargas, M. Grätzel, M.K. Nazeeruddin, and H.J. Bolink, Nat. Photonics **8**, 128 (2013).

8 M. Liu, M.B. Johnston, and H.J. Snaith, Nature **501**, 395 (2013).

9 D. Liu and T.L. Kelly, Nat. Photonics **8**, 133 (2013).

10 W.A. Laban and L. Etgar, Energy Environ. Sci. **6**, 3249 (2013).

11 J.H. Heo, S.H. Im, J.H. Noh, T.N. Mandal, C.-S. Lim, J.A. Chang, Y.H. Lee, H. Kim, A. Sarkar, M.K. Nazeeruddin, M. Grätzel, and S. Il Seok, Nat. Photonics **7**, 486 (2013).

12 J. Burschka, N. Pellet, S.-J. Moon, R. Humphry-Baker, P. Gao, M.K. Nazeeruddin, and M. Grätzel, Nature **499**, 316 (2013).

13 J.M. Ball, M.M. Lee, A. Hey, and H.J. Snaith, Energy Environ. Sci. **6**, 1739 (2013).

14 A. Abrusci, S.D. Stranks, P. Docampo, H.-L. Yip, A.K.-Y. Jen, and H.J. Snaith, Nano Lett. **13**, 3124 (2013).

15 J. You, Z. Hong, Y.M. Yang, Q. Chen, M. Cai, T. Song, C. Chen, S. Lu, Y. Liu, H. Zhou, and Y. Yang, ACS Nano **8**, 1674 (2014).

16 Y. Ogomi, A. Morita, S. Tsukamoto, T. Saitho, N. Fujikawa, Q. Shen, T. Toyoda, K. Yoshino, S.S. Pandey, T. Ma, and S. Hayase, J. Phys. Chem. Lett. **5**, 1004 (2014).

17 P.-W. Liang, C.-Y. Liao, C.-C. Chueh, F. Zuo, S.T. Williams, X.-K. Xin, J. Lin, and A.K.-Y. Jen, Adv. Mater. (2014) DOI: 10.1002/adma.201400231.

18 G.E. Eperon, V.M. Burlakov, A. Goriely, and H.J. Snaith, ACS Nano **8**, 591 (2014).

19 Q. Chen, H. Zhou, Z. Hong, S. Luo, H.-S. Duan, H.-H. Wang, Y. Liu, G. Li, and Y. Yang, J. Am. Chem. Soc. **136**, 622 (2014).

20 A. Dualeh, N. Tétreault, T. Moehl, P. Gao, M.K. Nazeeruddin, and M. Grätzel, Adv. Funct. Mater. (2014) DOI: 10.1002/adfm.201304022.

21 T. Leijtens, B. Lauber, G.E. Eperon, S.D. Stranks, and H.J. Snaith, J. Phys. Chem. Lett. **5**, 1096 (2014).

22 M. Saliba, K.W. Tan, H. Sai, D.T. Moore, T. Scott, W. Zhang, L.A. Estroff, U. Wiesner, and H.J. Snaith, J. Phys. Chem. C (2014) DOI: 10.1021/jp500717w.

23 K.W. Tan, D.T. Moore, M. Saliba, H. Sai, L.A. Estroff, T. Hanrath, H.J. Snaith, and U. Wiesner, ACS Nano 8, 4730 (2014).

24 G.E. Eperon, V.M. Burlakov, P. Docampo, A. Goriely, and H.J. Snaith, Adv. Funct. Mater. **24**, 151 (2014).

25 Y. Zhao and K. Zhu, J. Phys. Chem. C **118**, 9412 (2014).

26 E. Edri, S. Kirmayer, M. Kulbak, G. Hodes, and D. Cahen, J. Phys. Chem. Lett. **5**, 429 (2014).

27 J.-Y. Jeng, K.-C. Chen, T.-Y. Chiang, P.-Y. Lin, T.-D. Tsai, Y.-C. Chang, T.-F. Guo, P. Chen, T.-C. Wen, and Y.-J. Hsu, Adv. Mater. (2014) DOI: 10.1002/adma.201306217.

28 M.M. Lee, J. Teuscher, T. Miyasaka, T.N. Murakami, and H.J. Snaith, Science **338**, 643 (2012).

29 J.-H. Im, C.-R. Lee, J.-W. Lee, S.-W. Park, and N.-G. Park, Nanoscale **3**, 4088 (2011).

30 D.H. Son, S.M. Hughes, Y. Yin, and A. P. Alivisatos, Science **306**, 1009 (2004).

31 L. Li, N. Sun, Y. Huang, Y. Qin, N. Zhao, J. Gao, M. Li, H. Zhou, and L. Qi, Adv. Funct. Mater. **18**, 1194 (2008).

32 H. Jeen, W.S. Choi, J.W. Freeland, H. Ohta, C.U. Jung, and H.N. Lee, Adv. Mater. **25**, 3651 (2013).

33 K. Nakajima, Y. Oaki, and H. Imai, Chempluschem **78**, 1379 (2013).

34 P. Wen, Y. Ishikawa, H. Itoh, and Q. Feng, J. Phys. Chem. C **113**, 20275 (2009).

35 H. Uchiyama and H. Imai, Langmuir **24**, 9038 (2008).

36 N. Kitazawa, Y. Watanabe, and Y. Nakamura, J. Mater. Sci. **7**, 3585 (2002).

37 S. Colella, E. Mosconi, P. Fedeli, A. Listorti, F. Gazza, F. Orlandi, P. Ferro, T. Besagni, A. Rizzo, G. Calestani, G. Gigli, F. De Angelis, and R. Mosca, Chem. Mater. **25**, 4613 (2013).

38 A. Poglitsch and D. Weber, J. Chem. Phys. **87**, 6373 (1987).

39 See supplementary material at [URL] for full experimental methods, 2D GIWAXS images, additional SEM micrographs, and FTIR spectra.

40 M. Olszak-Humienik, Thermochim. Acta **378**, 107 (2001).

41 O. Yamamuro, M. Oguni, T. Matsuo, and H. Suga, Thermochim. Acta **98**, 327 (1986).

42 V. Roiati, E. Mosconi, A. Listorti, S. Colella, G. Gigli, and F. De Angelis, Nano Lett. **14**, 2168 (2014).

4.6 *Supporting Information*

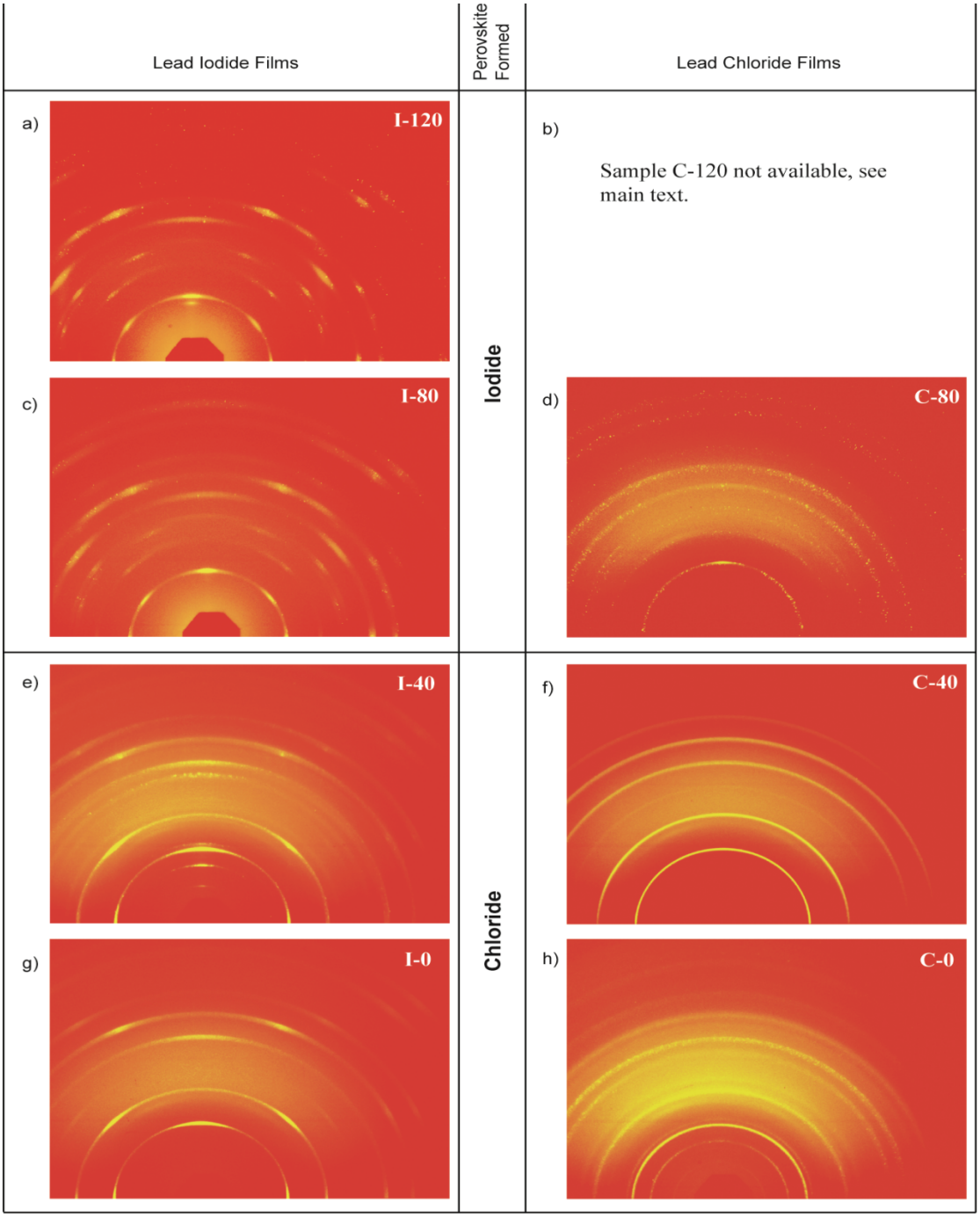

Figure 4.5: 2D GIWAXS images of perovskite films made by soaking lead halide films (parameters and sample designations given in main text) in MA halide salts; (a and c) lead iodide films resulting in $MAPbI_3$, (d) lead chloride film resulting in $MAPbI_3$, (e and g) lead iodide films resulting in $MAPbCl_3$, and (f and h) lead chloride films resulting $MAPbCl_3$

a)

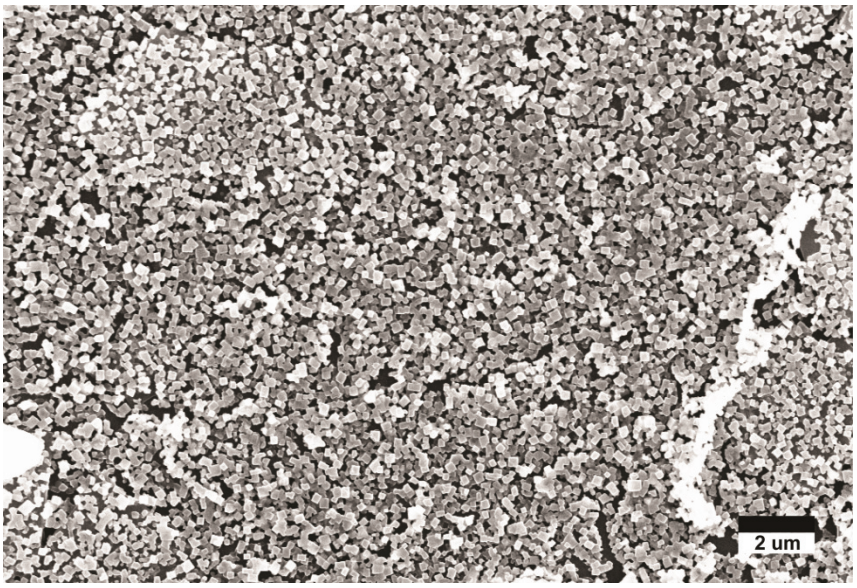

b)

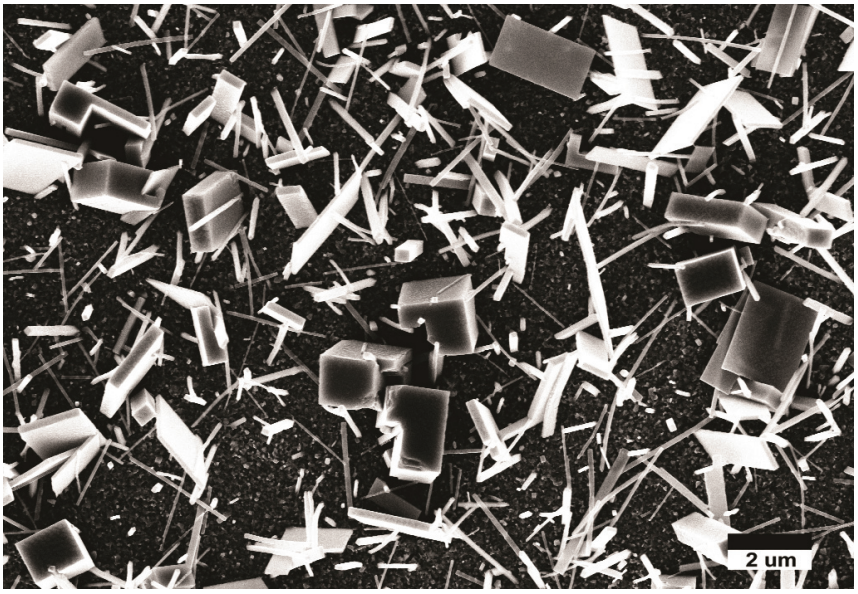

Figure 4.6: SEM images of $MAPbI_3$ made by soaking lead halide films in MA halide solution, I-80 (a) soaked for 2 hours, and C-80 (b) soaked for 4 hours.

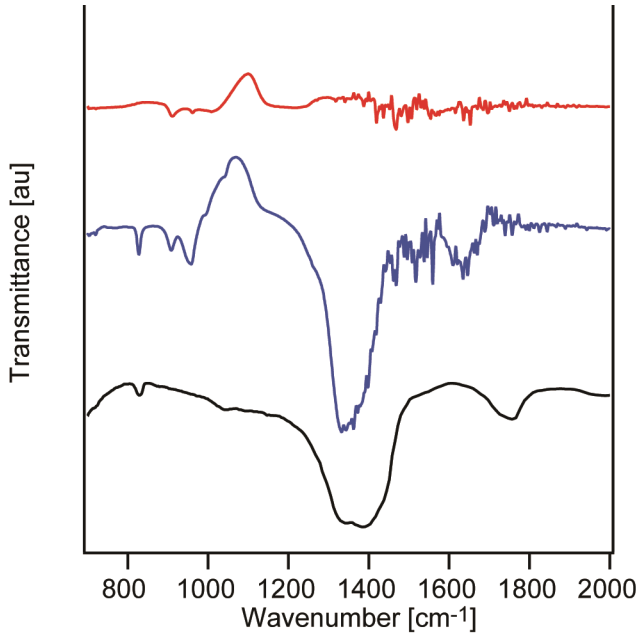

Figure 4.7: FTIR spectra of films made by spincoating with solution prepared with $Pb(NO_3)_2$ as the lead source: film as cast and annealed (blue, middle); film after rinsing with IPA (red,top). For comparison the bottom shows NIST data for ammonium nitrate (black) showing the characteristic NO peaks at 1300-1400 cm^{-1} and 830 cm^{-1}, respectively.

4.6.1 Experimental Methods

Materials

Isopropyl alcohol (ACS grade, Macron Fine Chemicals), acetone (ACS grade, Macron Fine Chemicals), ethanol (200 proof, KOPTEC), *N,N*-dimethylformamide (anhydrous, Sigma-Aldrich), hydriodic acid (57 wt% in water, Sigma-Aldrich), methylamine (33 wt% solution in ethanol, Sigma-Aldrich), methylammonium chloride (Sigma-Aldrich), lead(II) iodide (99%, Sigma-Aldrich), lead(II) chloride (98%, Sigma-Aldrich), and lead(II) nitrate (ACS reagent, Sigma-Aldrich) were used as received.

Substrate preparation

Glass or Si substrates were cleaned by sequential sonication in Alconox solution, acetone, and isopropyl alcohol (IPA) followed by thorough rinsing with IPA and distilled water and subsequent drying under nitrogen. Just prior to deposition, substrates were cleaned by air plasma for 5 minutes.

Lead halide film preparation

The lead halide films were made by thermal evaporation in a custom made evaporation chamber inside a nitrogen glovebox. Base pressure was typically 10^{-7} torr at the start of the deposition and the power was adjusted to achieve a deposition rate of 2.0 Å/s with a final film thickness of 1 μm for the soaked films and 50 nm for films used for sublimation.

Methylammonium halide solution preparation

Methylammonium (MA) iodide was prepared by precipitation from hydroiodic acid and methylamine solution in ethanol as previously reported. Methylammonium chloride and anhydrous IPA were purchased from Sigma-Aldrich and used as received. MA solutions were prepared by dissolving the MA salt in IPA in a nitrogen glovebox at 120mM concentrations. Molarity of the different MA solutions listed in Table 4.1 of the main text was achieved by mixing MAI solution and MACl solution prior to dipping the substrates and stirring briefly.

Perovskite formation by soaking

Lead halide films were transformed to perovskite by soaking in methylammonium halide solutions in a nitrogen glovebox. Lead iodide films were soaked for a total of 2 hours while lead chloride films were soaked for 4 hours. After soaking the films were removed and thoroughly rinsed with IPA.

Film preparation by sublimation

Lead halide films were placed in a Petri dish, on a hotplate, with a small amount (~200-500 mg) of MAI salt and covered with a filter funnel; the films were heated to 150 ºC and annealed for 7 hours. After annealing, the films were rinsed with IPA and allowed to dry; all sublimation preparation was done in a nitrogen glovebox.

$Pb(NO_3)_2$ solution and film preparation

$Pb(NO_3)_2$ based films were prepared by dissolving $Pb(NO_3)_2$ and MAI in a 1:3 molar ratio in anhydrous DMF (40 wt% total solid content) and stirring overnight in a nitrogen glovebox. Films were prepared on glass by spin coating at 2500 rpm for 45 seconds. Immediately after spin coating, substrates were placed on a hotplate at 25 ºC and the temperature increased at a rate of 1 ºC/min. The temperature ramp was

stopped when the films turned brown by visual inspection, which occurred at 45 ºC, and then held at 45 ºC for an additional 10 minutes. Spray coated films were prepared by spraying a 20 wt% solution onto substrates preheated to 60 ºC using a commercial airbrush with nitrogen gas at a delivery pressure of 25 psi.

Grazing incident wide-angle X-ray scattering (GIWAXS)

GIWAXS data was collected at beamline G1 at the Cornell High Energy Synchrotron Source (CHESS) using Fuji image plates, 2500x2000 pixels with 100 μm/pixel resolution, placed in a holder at a distance of 179.83 mm and digitized using a GE Healthcare Typhoon FLA-7000 image plate reader. The X-ray wavelength was 0.1225 nm. The incident beam angle was above the substrate critical angle with exposure times <5 seconds. All samples were prepared within 72 hours of data collection and stored in a nitrogen glovebox until used.

X-ray Diffraction (2-theta scans)

X-ray diffraction patterns were collected using a Scintag Theta-Theta X-ray Diffractometer using Cu-Kα radiation (λ=1.5405 Å). Scan speeds were adjusted such that the complete scan time was no more then 20 minutes to minimize X-ray damage to the films.

Absorption spectroscopy

UV-vis absorption spectra were taken on a Cary 5000 UV-Vis-NIR spectrometer in transmission mode with the integrating sphere accessory to eliminate scattering.

CHAPTER 5
A KINETIC STUDY OF THE ORGANIC-INORGANIC TRIHALIDE PEROVSKITES: DETERMINATION OF THE PRECURSOR MATERIAL AND THE ROLE OF THE LEAD ANION IN CRYSTALLIZATION

5.1 Abstract

Methylammonium lead halide perovskite solar cells continue to excite the research community due to their rapidly increasing performance which, in large part, is due to improvements in film morphology. The next step in this progression is control of the crystal morphology which requires a better fundamental understanding of the crystal growth. In this study we use in situ x-ray scattering data to determine the activation energy for the perovskite crystallization and show how it changes as a function of the lead salt reagent used in the synthesis. This data allows us to discern the composition of the precursor material and establish the general pathway of the crystallization.

5.2 Introduction

The rapid rate of increase in device performance reported for organic-inorganic trihalide perovskites, *e.g.* $CH_3NH_3PbI_3$, has energized the photovoltaic communities' efforts to create low cost solar cells from inexpensive and abundant constituents.[1,2,3] Over the last year many researchers have been moving from a mesoscopic cell architecture to planar devices, with planar cells now exceeding the efficiency of mesoscopic cells with an uncertified report of 19.3% efficiency.[4] The use of a planar architecture is predicated on the ability to fabricate continuous, conformal layers. The ability to make high efficiency planar devices is dependant on a variety of factors, however, there have been several reports which correlate both the film and crystal morphology (e.g. grain size and/or orientation) to device performance.[5,6,7] Thus, the control of the final film and crystal morphology is a critical parameter in achieving consistent, high performance devices; and this control usually begins with a

fundamental understanding of the crystal growth, both its mechanism and kinetics. Our goal in this work is to elucidate the crystallization process of the organic-inorganic halide perovskites by an in-situ X-ray scattering study of the crystal growth dynamics.

The initial application of these perovskites was as a dye replacement in dye-sensitized solar cells (DSSC) and utilized a mesoporous transport material of TiO_2; in the last two years device efficiencies based on this architecture have increased from ~10% to over 17%.[,8,9,10] Recent reports have shown equal or better performance in planar devices, while noting that one of the barriers to further performance enhancement is the film morphology, specifically film coverage and conformity to the underlying substrate.[11,12] Holes in the active layer, due to incomplete coverage, reduce the generation of photocurrent and, more importantly, create shunt paths for photoexcited carriers. In 2013 alone there were multiple studies that investigated film processing parameters to improve the total film coverage by changing the annealing conditions,[13] co-evaporation of both salts,[11] spincoating the metal halide salt followed by soaking in the organic halide salt,[14] and spincoating the metal halide salt followed by vapor deposition of the organic halide.[15] In spite of the positive impact these studies have had on film uniformity, there is still a lack of a fundamental understanding of the mechanisms leading to the final film and crystal morphology.

In studies of film evolution in both mesoporous and planar electrode configurations, we previously reported three distinct structure transitions including solution-to-precursor, precursor-to-perovskite, and perovskite-to-PbI_2.[5,16] The observation of a crystalline structure prior to the perovskite formation, as well as the perovskite decomposition to lead iodide has also been noted by others.[10,17] These observations indicate that understanding the nature of the precursor material, and those factors that cause its transition to the perovskite, are keys to being able to predictably control the crystal and film growth.

Here, we turn our attention to the underlying kinetics of the precursor-to-perovskite transition. We begin by developing an appropriate methodology to analyze in-situ X-ray data to quantify the degree of perovskite formation when crystallizing in

thin films. We verify our method by applying it to time/temperature structural evolution data and compare this analysis to a general model to validate its applicability. We use our validated method to analyze the crystallization dynamics of the perovskite when using different lead salts, in non-stoichiometric solutions, to extract the activation energy (E_a) for the transition. Finally, we use the E_a and WAXS patterns for the different systems we tested to determine the composition of the precursor and the role of the spectator species in the crystallization dynamics.

5.3 Results and Discussion

5.3.1 Quantifying the precursor-to-perovskite transformation

A kinetics study requires tracking the extent to which a transformation occurs in time; doing so requires both a qualitative and quantitative measure of both the starting and ending points of the transformation. In previous publications we have established these transitions qualitatively and refer the reader to Ref. 5 and 16 for complete details. Briefly, there are three distinct solid state structures that occur (in order, temporally): (1) a metastable, crystalline intermediate which we refer to as the precursor, (2) the desired perovskite, and (3) PbI_2, the decomposition product. *In situ*, wide angle X-ray scattering (WAXS) patterns, using conditions equivalent to those used to make working devices, were recorded and analyzed to establish the overall crystal evolution. Figure 5.1 shows representative 2D WAXS images for these three structures from thin films made from a non-stoichiometric solution of $PbCl_2$ and CH_3NH_3I ((MA)I), as well as a waterfall plot that demonstrates the overall evolution.

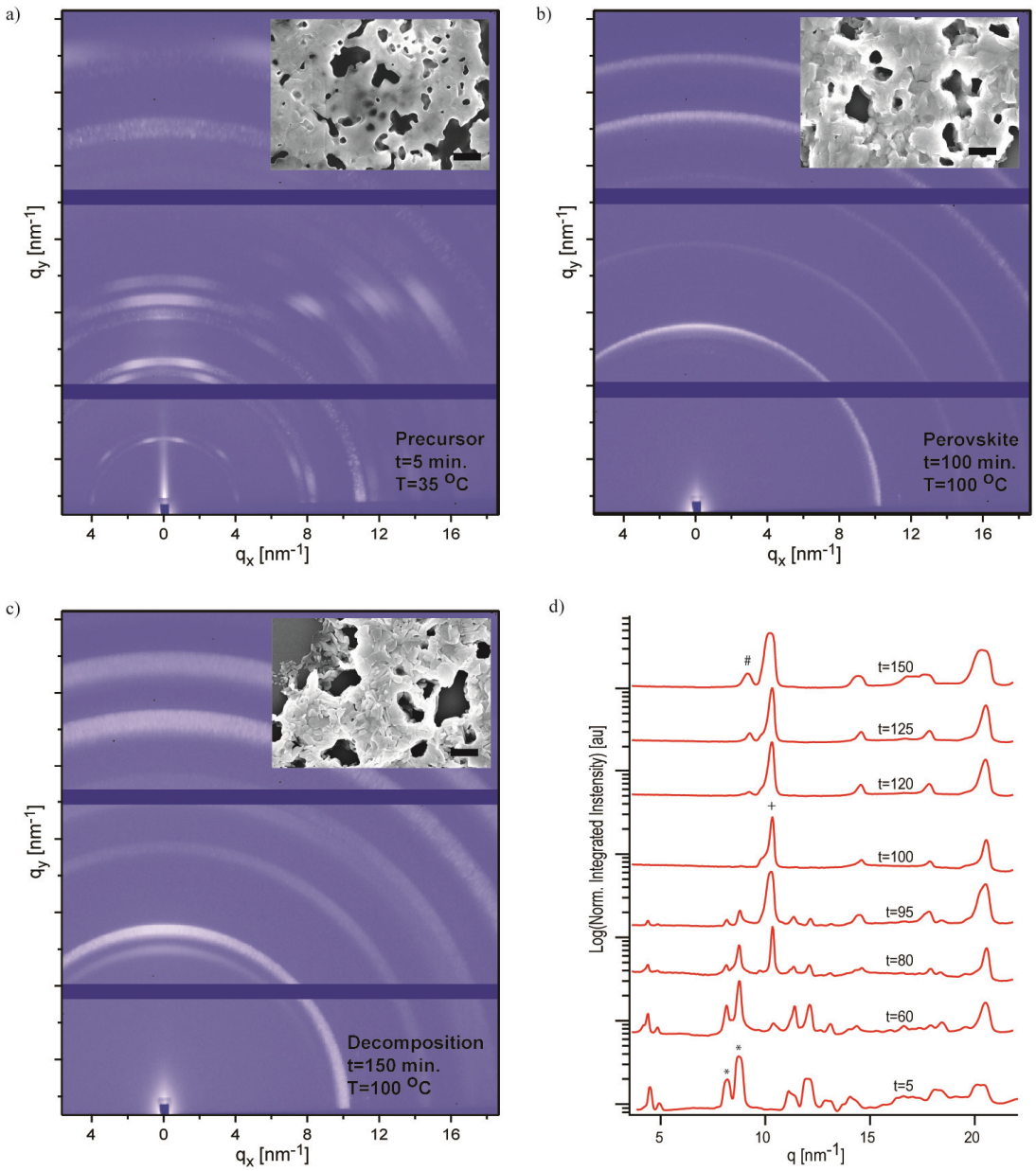

Figure 5.1: WAXS images (a, b, and c) for 40 wt% solution of $PbCl_2$/(MA)I on Si thermally annealed from ambient temperature to 100ºC: (a) precursor at t=5 min. and T=35 ºC, (b) perovskite at t=100 min. and T=100 ºC, and (c) PbI_2 (decomposition) at t=150 min. and T=100 ºC. Insets in (a-c) are corresponding SEM images with a 1 µm scale bar. (d) Corresponding azimuthally integrated 1D plots at key time points showing the overall evolution, the markers above the traces at 5, 100, and 150 minutes are the strong peak locations for the precursor (*), perovskite (+), and PbI_2 (#) that are used to track the transformations.[18,19]

In the course of our previous work, and in this study, several different processing parameters were explored including different deposition methods, varying temperature profiles, and changes to the lead salt reagent; in all cases the overall evolution is the same: precursor → perovskite → PbI_2. Regardless of the reagent salt used, we find the scattering pattern of the perovskite in excellent agreement with the tetragonal iodide perovskite; the agreement with the known peak locations of the iodide perovskite, along with elemental analysis recently published, confirm that we are making the iodide perovskite in all cases.[PbAc] Furthermore, we established key scattering peaks associated with the precursor that are unique to its structure; given that the perovskite and PbI_2 structures are known, identification of scattering peaks unique to the precursor allows us to distinguish each of the structures qualitatively. For the perovskite and PbI_2 the key peaks are located at q=10 nm^{-1} and q=9 nm^{-1} respectively, where q denotes the magnitude of the scattering vector and is defined as $q = 4\pi\sin\theta/\lambda$ where θ is half of the total scattering angle and λ is the x-ray wavelength. These peaks are chosen because they are strong, easily distinguishable, and in the low q range where they are not obscured by higher order reflections. The key peaks for the precursor structure change depending on the lead salt used, this is discussed in detail below, however, in all cases there are key peaks below q=9 nm^{-1}; since the smallest q vector for either the perovskite or PbI_2 is at q=9 nm^{-1}, any peak below this allows us to distinguish the precursor. These previous results provide the qualitative measure we need to identify each structure uniquely. In this study we are concerned with the precursor-to-perovskite transition, and the kinetic analysis requires an appropriate quantitative measure of the extent of the transformation.

The kinetic analysis of solid state transformations is commonly accomplished by determining the transformed fraction of a material, x, by tracking some property (e.g. conductivity, magnetism, modulus) that has different and known values for both the starting and ending states of the transformation.[20] In the present experiments, the WAXS data contain a direct measure of the quantity of diffracting planes with a specific orientation; this quantity is a measurable property that can be used to determine $x(t)$. The bottommost trace in Figure 5.1D shows that the strong reflection

of the tetragonal perovskite structure (110) plane at q = 10 nm^{-1} is not present in the precursor, hence, we track the (110) peak to determine x. Defining the integrated scattering intensity of the (110) peak as A_{10}, and given that this peak does not exist in the precursor, we can set $A_{10}(0) = 0$; this is the known value for the starting state. To define a known value for A_{10} for the pure perovskite we note from Fig. 5.1D (trace at t=100 min.) that there are no peaks below q = 9 nm^{-1} for the perovskite structure. We define a time, t_{end}, as the point in time when the peaks below q = 9 nm^{-1} completely disappear and use the measured value, $A_{10}(t_{end})$, to denote the property's value for the ending state. Mathematically, this gives the following definition for $x(t)$:

$$x(t) \equiv \frac{A_{10}(t)}{A_{10}(t_{end})}, \tag{5.1}$$

so that $x(0) = 0$ and $x(t_{end}) = 1$. The validity of the definition of $x(t)$ used here is based on a few assumptions:

1. The disappearance of the precursor peaks is due to the transformation to a different material (the perovskite) and not due to re-orientation of the precursor grains such that the tracked peaks are no longer incident with the Ewald sphere. If the latter were true we would expect the appearance of new peaks not associated with the perovskite; there are no new peaks that appear during the transformation and, thus, we assume the former is true.
2. The transformation is a direct transition from the solid state precursor to the perovskite, as opposed to dissolution and recrystallization. In the case of dissolution there would be an increased volume of amorphous material, leading to an increase in the background scattering. We see no evidence of increased background scattering during the transformation (Supporting, Fig. 5.7) and take the assumption of a solid state transformation to be valid. It should be noted that there is some possibility that dissolution and recrystallization occurs at a temporal resolution finer than that used in the current experiments; although we cannot discount this possibility, it would not change the analysis or conclusions reached here.
3. There is no appreciable change in the crystallographic orientation of the perovskite crystals during the transformation. If the perovskite grains rotate

during the transformation the resulting plots of *x(t)* would not be monotonic; the data presented below shows monotonic, sigmoidal plots as expected for a solid state transformation. The goodness of fit to the mathematical model (discussed below), particularly in the linear portion of the plots, indicates that this assumption is also reasonable. We point out that a fixed orientation is only required for the perovskite and only during the transformation. The fact that the precursor and perovskite structures have different crystallographic orientations relative to each other, as well as different textures (Fig. 5.1A and 5.1C), does not matter so long as they don't change relative to themselves. Additionally, after the initial point when *x(t)* = 1, i.e. the precursor is completely gone, the perovskite can coarsen and it does not effect the results as we are only concerned with the transition itself.

The initial system studied was the mixed halide system using $PbCl_2$ and (MA)I, which we will refer to as the chloride system, with full composition, deposition, and annealing details given in the experimental section. Given the above assumptions, we apply Eqn. 5.1 to *in situ* WAXS data taken at ~3 minute intervals until ~10-15 minutes after the precursor completely disappears; for the chloride system the precursor pattern shows clear peaks centered at q~7.9 and 8.5 nm^{-1} (Fig. 5.2A) and we use both in our analysis. This process yields the required time-dependent data to construct an *x(t)* plot (Fig. 5.2B), which is the quantitative measure of the transformation needed for a kinetics study.

5.3.2 Kinetic modeling of the precursor-to-perovskite transformation

Once a valid Once a valid measure for *x(t)* has been determined, kinetic parameters can be extracted by applying an appropriate model for the transformation. Mittemeijer and co-workers have done extensive work on the mathematical analysis of kinetic data for solid-state transformations for a wide variety of both nucleation and growth modes.[21,22,23] In addition to providing specific models for different systems, they also derive formulas for either isothermal or isochronal data that make no

assumptions about the type of nucleation or growth; we use their formula for isothermal data here and refer the reader to Ref. 22 for detailed derivations:

$$\ln(t_{x2} - t_{x1}) = \frac{E_a}{RT} - \ln k_0 + \ln(\beta_{x2} - \beta_{x1}) \tag{5.2}$$

where t_{xn} is the time at which the transformed fraction is x_n, E_a is the effective activation energy, R is the gas constant, T is the temperature, k_0 is the rate constant prefactor, and β_{xn} is a state property that is invariant to the time/temperature path. The introduction of β_{xn} assumes that there is some state property that is monotonically related to the physical property being measured, ergo, it is also related to the transformed fraction of the film, i.e. $x=F(\beta)$ where the form of F need not be known. To apply equation 5.2, data is plotted as $\ln(t_{x2}-t_{x1})$ versus $1/RT$ and the slope of the line taken as E_a; it should be noted that the extracted E_a is an effective activation energy for the transformation as a whole, where the activation energies for nucleation and growth are still coupled. Although the present data is insufficient to determine specific nucleation and growth modes, an effective E_a can still provide key insight into the crystallization process and the extent to which it can be affected by changes to the reaction chemistry.

Several films were prepared using the chloride system while changing only the annealing temperature. Isothermal data was taken at 80 °C, 90 °C, 100 °C, and 110 ºC and $x(t)$ extracted from the resulting WAXS data; the temperature range was chosen based on previous reports that substantial crystallization does not occur below 80 °C and that a morphological change takes place at 130 °C.[6,17] Figure 5.2A shows representative 1D plots, at several key time points, taken from the 90 °C sample; with $x(t)$ for all four isothermal samples plotted in Figure 5.2B. As noted in the experimental section, data was taken at several locations on each film, the resulting plots of $x(t)$ are the average of all sampled regions; as expected, the plots are sigmoidal and the rate of the transformation (the time axis in Fig. 5.2b is log scale for clarity) increases with higher temperatures. Starting and ending fractions of x_1=0.2 and x_2=0.9 were chosen and the corresponding times used in equation 5.2 to construct the plot in Figure 5.2C, which yields an effective activation energy of 86 +/-6 kJ/mol.

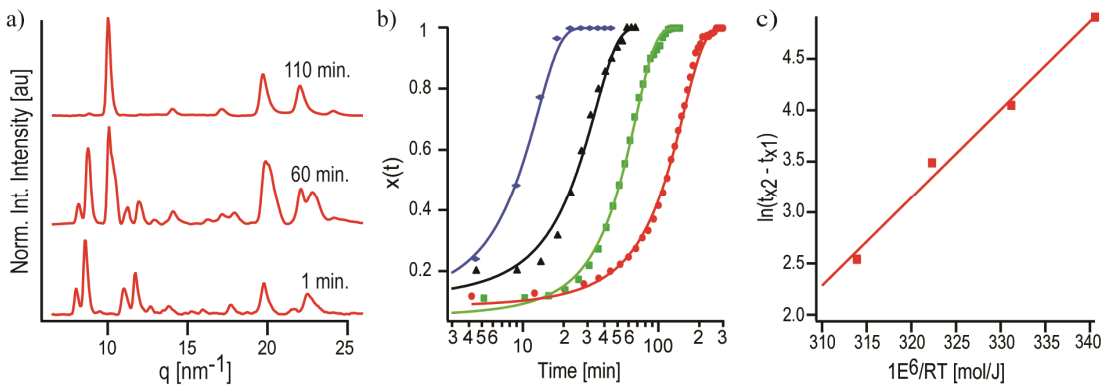

Figure 5.2: Kinetic data for isothermally annealed samples made from 40 wt% in DMF using $PbCl_2$ as the lead salt. (a) Azimuthally integrated WAXS data for the 90 °C sample showing the precursor (1 min.), transition (60 min.) and perovskite (110 min.) stages of the transformation. (b) *x(t)* plot for isothermal samples at 80 °C (red, circles), 90 °C (green, square), 100 °C (black, triangle), and 110 ºC (blue, diamond) with the JMA model fit (Eqn. 5.5, solid line of the same color); *x(t)* is defined in the text. (c) Plot constructed from Eqn. 5.2 to extract E_a, slope of the line is 86 +/- 6 kJ/mol.

The nature of the *x(t)* plots, their change with increasing temperature, and the goodness of the linear fit line in Fig. 5.2C confirms that the methodology used is reasonable. We can further extend our kinetic analysis, then, by using the extracted E_a in an appropriate kinetic model. The Johnson-Mehl-Avrami (JMA) model has been widely used to describe solid state transformations and we apply it here in the well known form: [24]

$$x(t) = 1 - \exp(-\beta^n) \tag{5.3}$$

where n is the growth exponent, which describes the dimensionality of the growth and should be between 1 and 4. Due to the Arrhenius behavior of the system, we assume a simple rate equation for β in the form of:

$$\beta = k(T)t = k_0 \exp\left(\frac{-E_a}{RT}\right)t \tag{5.4}$$

where the variables used are the same as in eqn. (5.2), and plugging (5.4) into (5.3):

$$x(t) = 1 - \exp\left[-\left(k_0 \exp\left(\frac{-E_a}{RT} \right) t \right)^n \right] \tag{5.5}$$

Equation 5.5 assumes that β follows Arrhenius behavior, E_a is not time dependent, and n is neither time nor temperature dependent. Fitting this model against our data, with E_a fixed at 86 kJ/mol, should yield constant values for k_0 and n. The best fits of Eqn. 5.5 describe the data well, as shown in Figure 5.2B, with k_0=4.1x10^{10} +/- 9.3x10^{9} and n=2.43 +/- 0.06; it should be noted that the fits were performed with those data points where $x(t) \geq 0.2$ heavily weighted as the signal-to-noise ratio increases dramatically at higher values of x. The extracted values are not only effectively constant for all temperatures, but the value of the growth exponent is reasonable for 2D thin films in the context of the JMA model. We point out that these fits were done in two steps, with E_a calculated using Eqn. 5.2 and the resulting value used in Eqn. 5.5; as such, we have not decoupled the nucleation and growth modes. Therefore, in spite of the agreement between the model and the data, we take the JMA model to be a good mathematical description of the system, but only phenomenologically; the values of k_0 and n should be taken as empirical fit parameters.

5.3.3 Application of the model

In order to apply a purely mathematical description at least one additional system needs to be analyzed, this would establish that a change in the crystallization time is due to a change in E_a versus a change in k_0 and/or n. Experimentally, it would be most efficient to have a methodology by which processing conditions (e.g. changing the lead salt reagent) could be altered at a single, random temperature, and a qualitative assessment made as to the impact on the crystallization kinetics. Since Eqn. 5.5 represents only a mathematical description of the film evolution, and because the current dataset provides no information about specific nucleation and growth modes, k_0 and n remain coupled. Therefore, we repeated a complete isothermal analysis on a second system to verify that n remains constant when changing the lead salt reagent, allowing us to apply Eqn. 5.5 to any additional system at a single temperature.

In a previous report we examined perovskite films crystallized from a non-halide lead source, $Pb(NO_3)_2$,[25] and found that the crystallization occurred much faster and at lower temperatures than either the iodide or chloride system. We chose the nitrate system, as a second system to analyze, due to the fact that the resulting data points would be widely disparate in both their temperature and time. Samples were prepared using identical conditions to the chloride samples shown in Figure 5.2 with only the following changes: (1) the solution was 1:3 molar ratio of $Pb(NO_3)_2$:MAI, and (2) the temperatures used were 30 °C, 35 °C, and 45 °C. The dataset was collected and analyzed using the same methodology and yielded the plots in Figure 5.3. Due to the speed with which the nitrate based films formed and the constraints of the chosen experimental setup, capturing the entire transformation was difficult, particularly at higher temperatures. In spite of a lower signal-to-noise ratio (temporally), Figure 5.3 shows that the nitrate system is similarly well described by the analysis method used.

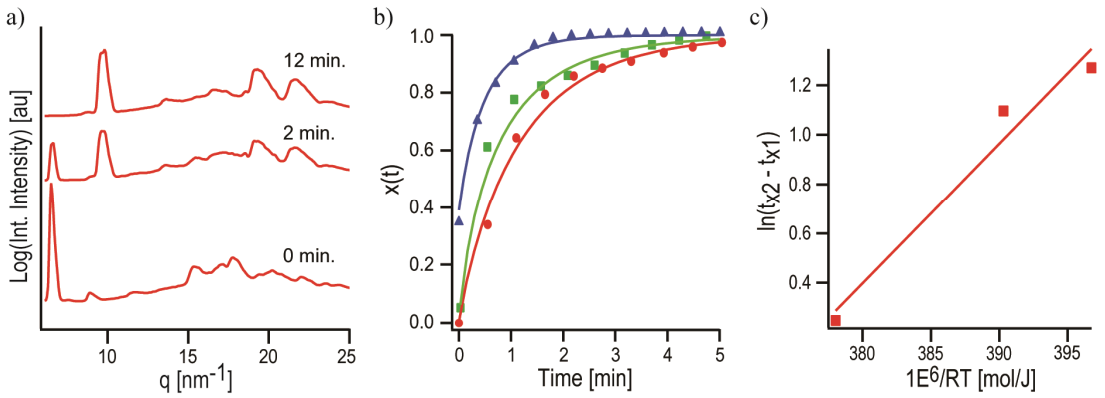

Figure 5.3: Kinetic data for isothermally annealed samples made from 40 wt% in DMF using $Pb(NO_3)_2$ as the lead salt. (a) Azimuthally integrated WAXS data for the 30 °C sample showing the precursor (0 min.), transition (2 min.) and perovskite (12 min.) stages of the transformation. (b) *x(t)* plot for isothermal samples at 30 °C (red, circles), 35 °C (green, square), and 45 ºC (blue, triangle) with the JMA model fit (Eqn. 5.5, solid line of the same color); *x(t)* is defined in the text. (c) Plot constructed from Eqn. 5.2 to extract E_a, the slope of the line was found to be 56.6 +/- 10 kJ/mol.

For the nitrate system our analysis yields E_a = 56.6 +/- 10 kJ/mol, with k_0 = 2.0×10^9 +/- 8.1×10^8 and n = 2.34 +/- 0.09; these values change as expected confirming that the JMA model is appropriate and inferring that the overall crystallization process

is not changed by a change to the lead salt. To the extent that the time/temperature required for complete transformation of the nitrate system is a kinetic effect, and not the result of a fundamentally different crystallization mechanism, we expect E_a and k_0 to be different while n should be the same. In terms of applying the methodology to changing the lead salt, the results indicate that the difference between the chloride and nitrate systems lies in the effective E_a. This approach allows for a qualitative comparison of different systems whose processing can not be accomplished at the same temperatures used for the complete isothermal data sets.

Mathematically, the determination of the kinetic parameters required a two-step approach; Eqn. 5.2 to extract Ea, followed by Eqn. 5.5 for k_0 and n, this was due to the coupling of parameters noted above. The application of the model to a second, complete, isothermal data set confirms that n is a constant. Based on the assumption that a change in the lead salt does not change the overall crystallization process, we can now fit Eqn. 5.5 by fixing n and using k_0 and E_a as the two free parameters which allows the extraction of E_a for additional systems at a single temperature as it only requires a single $x(t)$ plot.

5.3.4 Dependency of activation energy on the lead salt

We complete our kinetic study by looking at the evolution of two additional systems, made using lead acetate and lead iodide, at a single temperature. We chose to explore changes to the lead salt because its role in non-stoichiometric systems remains open and relevant to increased device performance based on the enhanced transport properties of films made using the chloride system.[26] In those cases where some or all of the lead salt anion is not incorporated into the perovskite, there is a spectator salt ((MA)Sp) remaining due to the non-stoichiometric salt ratios used,

$$PbSp_2 + 3(MA)I \rightarrow (MA)PbI_3 + 2(MA)Sp \qquad (5.6)$$

therefore, exploring different lead sources is synonymous with exploring the role of the spectator salt. The acetate system was developed by Zhang et al.;[27] the complete data set can be found in Ref. 27 and we only present the extracted kinetic data for that system in this paper. The iodide films were prepared from a non-stoichiometric solution, using a 3:1 molar ratio of (MA)I:PbI_2 and annealed at 150 °C. The annealing

temperatures used for the iodide and acetate systems correspond to the temperature which yielded the best device performance, also reported in Ref. 27.

The Δt between x=0.2 and x=0.9 for the acetate system, annealed at 100 °C, was found to be 1.14 minutes (the same Δt for the chloride system at 100 °C is 12.7 min.); by direct comparison this sets the kinetics of the acetate faster than those for the chloride system, and, by extrapolation of the nitrate to 100 °C, slower than the nitrate. Fitting Eqn. 5.5 to the single $x(t)$ plot, black diamonds in Figure 5.4A, with n constrained to 2.4 +/- 0.1, results in the solid black fit line in Fig. 5.4A and a value of E_a = 67.5 kJ/mol; this value for E_a is between that of the chloride and nitrate systems as expected. The Δt between x=0.2 and x=0.9 for the iodide system, annealed at 150 °C, was found to be 11.6 minutes; given that Δt for the same transformed fraction of the chloride system at 110 °C is 12.7 minutes, it is obvious that the iodide system is slower. We repeat the same analysis as for the acetate system, and the resulting plots of $x(t)$ and the fit to Eqn. 5.5, is shown in Fig. 5.4A (red, circles). Figure 5.4B shows the Arrhenius plots for both the chloride and nitrate systems with their best fit lines as solid lines; for the acetate and iodide systems the single data point has been added and the line (dashed) constructed using the slope determined by Eqn. 5.5. The complete results, for all four systems, are tabulated in Table 5.1.

Table 5.1: Extracted parameters from Eqn. 5.5 for all four systems based on the global fit shown in Fig. 5.4A

System	Temp. [°C]	E_a [kJ/mol]	k_0 [au]	n [au]
Iodide	150	97.3	6.8×10^{10}	2.4
Chloride	90	86.6	4.1×10^{10}	2.4
Acetate	100	67.5	2.1×10^{9}	2.4
Nitrate	45	56.6	2.3×10^{9}	2.4

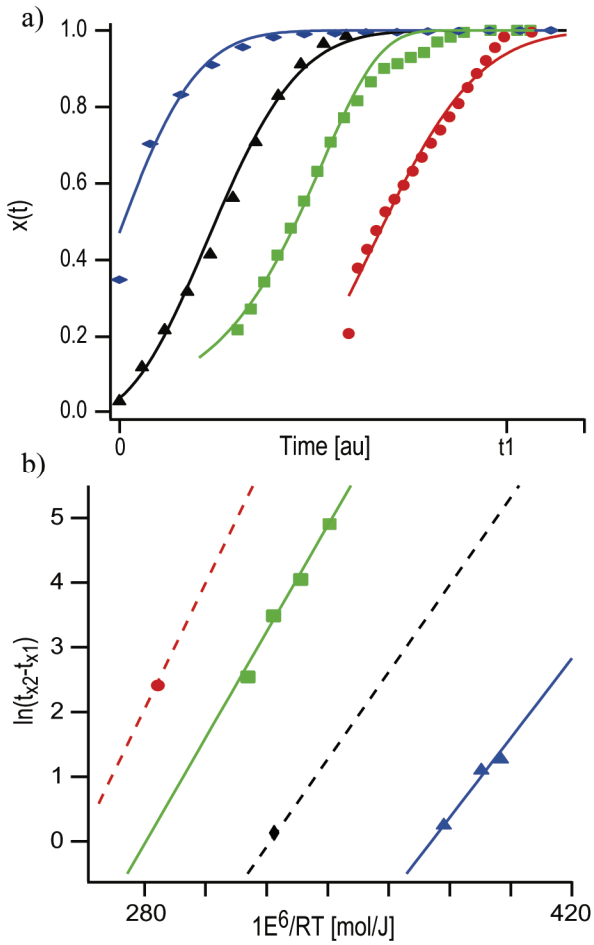

Figure 5.4: Kinetic data for all four systems prepared from a 40 wt% solution in DMF using different lead salts. (a) *x(t)* plots for the nitrate (blue,diamond), acetate (black, triangle), chloride (green, square), and iodide (red, circle) systems annealed at 45 °C, 100 °C, 100 °C, and 150 °C, respectively; data is scaled on the abscissa so that t_{end} (defined in text) is coincident for all traces, then offset for clarity. Solid lines are the best fit lines of a global fit to Eqn. 5.5. (b) Arrhenius plots for the same four systems (same colors/shapes as above) with best fit lines (solid) and calculated fit lines using E_a extracted from (a) (dashed).

As previously noted, our own data, and reports by others, continue to confirm that chloride is not substantially incorporated into the iodide structure and we assume that we are making the iodide perovskite in all cases presented here.[28,29] Given that $(MA)PbI_3$ is the structure we are forming in all cases, the change in E_a for the different systems is only a function of the change in the lead salt used. The fact that changing the lead salt effects E_a for the crystallization provides key insight into the nature of the precursor structure as well as the overall crystallization process.

5.3.5 The precursor phase and the role of the spectator salt

As previously stated, understanding the nature of the precursor is an important step to controlling the final film morphology. In this section, we use the scattering patterns along with the kinetic data derived above, to determine the composition for the precursor and the process by which the transformation to the perovskite occurs.

The kinetic analysis performed in this study was facilitated by the fact that each system has a precursor scattering pattern distinguishable from the final perovskite structure. The 2D WAXS patterns (Supporting info, Fig. 5.8) of the precursor structures clearly show that the precursor is a crystalline structure with a high degree of orientation in the film normal direction. Figure 5.5A shows the 1D patterns, in the low q range where the distinctive precursor peaks appear, for all four systems prepared using identical processing with the exception of the lead salt. The fact that the precursor scattering pattern is different for each lead salt used is clear evidence that the precursor structure contains the spectator salt. The only other component in the film is the solvent, and to check for incorporation of the solvent we prepared films using the chloride system with identical processing while changing only the solvent. Figure 5.5B shows the resulting 1D scattering patterns; the excellent agreement in the scattering patterns of films made from DMF and DMSO demonstrates that the resulting structure has no dependence on the solvent used and, therefore, we discern that there is no incorporated solvent in the precursor structure. These results tell us that the precursor structure is composed of Pb^{2+}, $(MA)^{+}$, I^{-}, and Sp^{-} ions where Sp^{-} denotes the anion of the spectator salt. Although we can not assign a structure or stoichiometry to the precursor, the composition alone provides insight into the kinetic data derived above as well as the overall process by which the perovskite forms.

We note that Seok, et al, recently published a paper in which they postulate that the precursor structure is due to incorporated solvent.[10] In their study the films were made with stoichiometric ratios of PbI_2 and (MA)I and so there is no spectator salt in the way that we have defined it here. Because the systems studied were different, and because we do not have sufficient detail on their characterization

methods, we can not comment on the difference in our results other than to say we see no evidence of solvent incorporation in the scattering data.

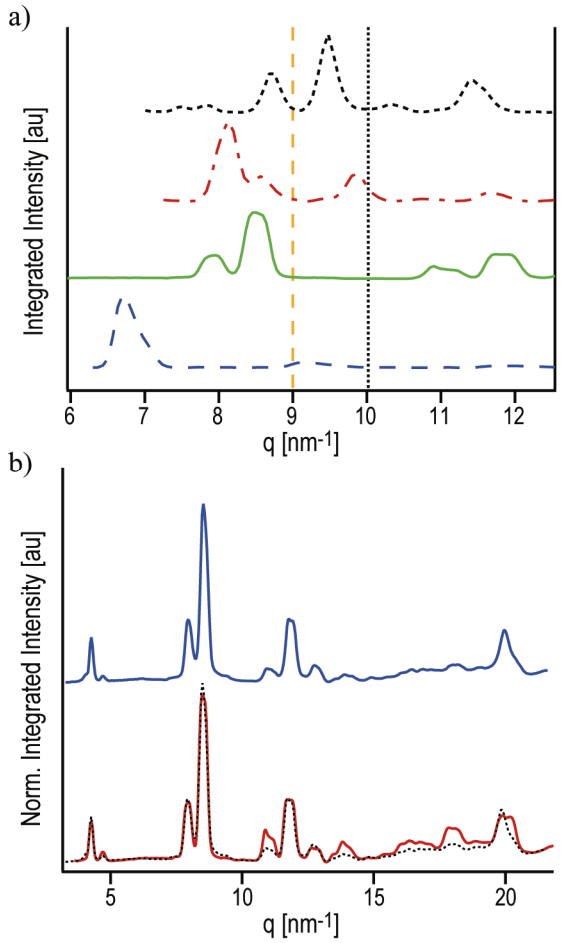

Figure 5.5: 1D, normalized, integrated WAXS data for thin films within 3 minutes of spin coating (a) using the same solvent but a different lead salt including acetate (black, dot), iodide (red, dot-dash), chloride (green, solid) and nitrate (blue, dash); vertical markers are the lowest q-vector reflection positions for PbI_2 (yellow, dash) and $(MA)PbI_3$ (black, dot) (b) Using the same lead salt (chloride) but different solvents, DMF (red, solid) and DMSO (blue, solid); the DMSO trace is shown a second time as a black dotted line superimposed on top of the DMF trace for easy comparison.

The composition of the precursor, taken with the activation energy for each system, tell us that the precursor-to-perovskite transition includes, and is dominated by, the removal of the excess spectator salt from the precursor. At this point we can make no assignment of cause and effect, i.e. does the migration of the spectator ions cause the perovskite transition or does the perovskite transition cause the migration of the

spectator ions. Additionally, any mechanistic insight is beyond the scope of this work although certainly determination of the cause and effect, as well as the mechanism by which it occurs, is a logical next step to a better fundamental understanding of these systems. In spite of these unanswered questions, the current insight is valuable in that it tells us that the crystallization process can be mediated by changes to the lead salt.

As a final step in our analysis, we use the extracted E_a, along with a variety of published and internal data, to propose a crystallization path and explain some of the results of this and previous studies. Figure 5.6 is a schematic representation of the crystallization pathway along with the corresponding scattering plots for key points in the crystal evolution. The supporting information contains a complete description of how the start time and length were determined for each process bar shown; although we have taken great care to be as accurate as possible the diagram shown is intended to be schematic in nature. The important point of this diagram is to identify the key processes, both advantageous and disadvantageous, and show how they are coupled in time. Knowledge of the precursor composition allows us to identify these processes as: evaporation of the solvent ("Evap. Solvent", brown), diffusion of the excess spectator salt out of the precursor structure ("Diffuse MASp", red), removal of the spectator salt from the film ("Sublime MASp", yellow), and removal of stoichiometric (MA)I from the perovskite lattice ("Diffuse MAI", blue). The diffusion of the spectator salt from the precursor is, effectively, the transition measured in this study, with its start and end points coinciding with the start and end of the precursor-perovskite transition. The diffusion of MAI from the perovskite lattice is a disadvantageous process which is the decomposition to PbI_2.

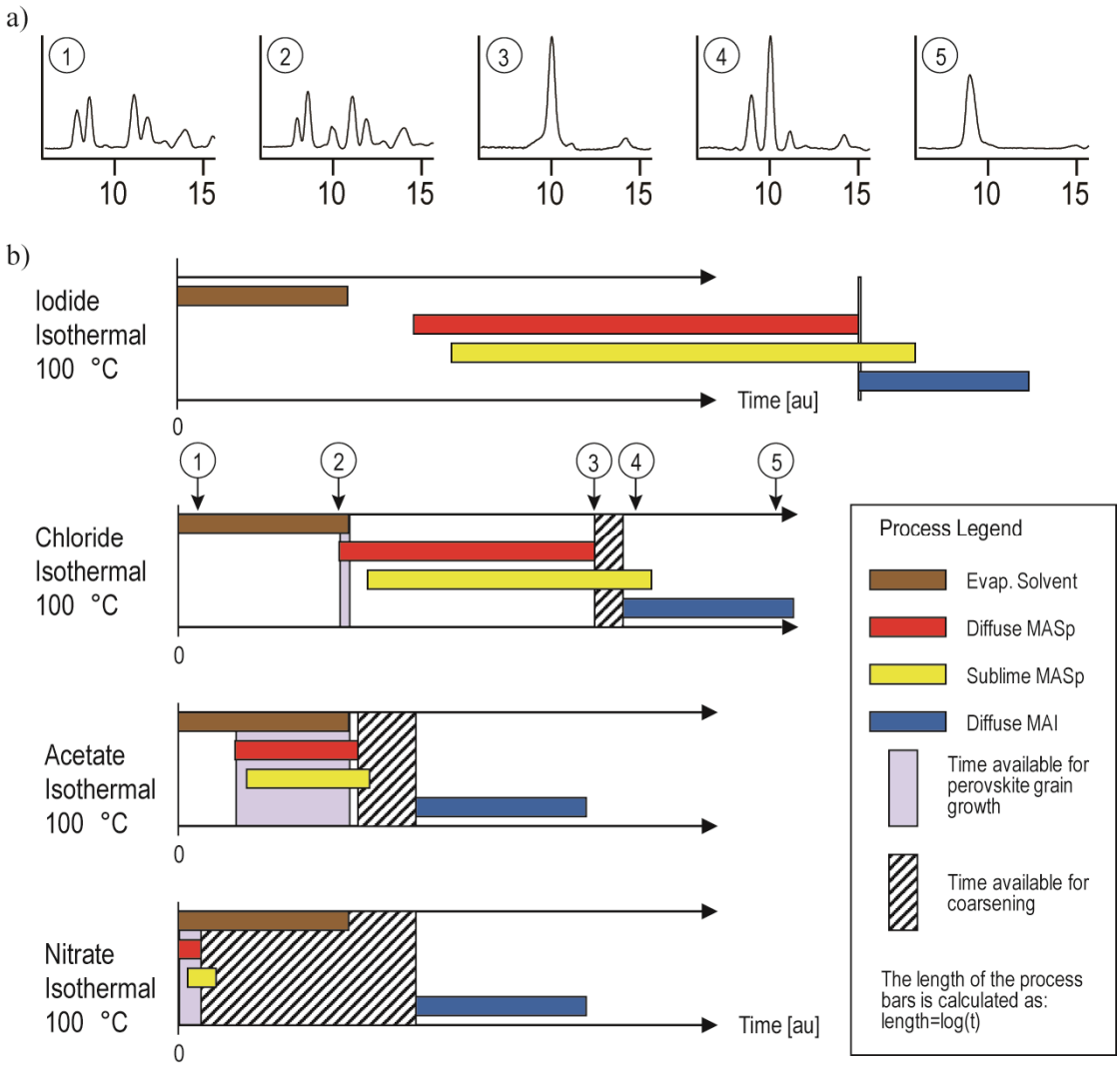

Figure 5.6: Schematic representation of the perovskite crystallization and growth pathway. (a) Scattering data for key time points for the chloride system (same sample as Fig. 5.1) with the normalized, integrated intensity plotted against q [nm^{-1}]; the correlation of each image to the schematic timeline is shown in (b) for the chloride system. (b) Schematic timelines for the four lead salt systems used in this study. The legend shows the title for each colored bar with the full explanation of the process given in the text. Although the pathway timeline is intended to be schematic, the start time and length for each process are calculated from data (see supporting information for details) to be as accurate as our data allows.

For the iodide system, the high E_a, and the low volatility of the spectator salt, require processing times and temperatures longer than those needed to evaporate the solvent but similar to those needed for decomposition. As a result, grain growth time is negligible and coarsening time is limited by the decomposition process. This elucidates one key role of the chloride, which is to advantageously affect the

crystallization kinetics. When chloride is used the crystallization process can proceed at lower temperatures; Graetzel's group and our previous reports fix the onset of crystallization at ~75-80 °C, versus ~100-110 °C for the iodide.[16,17] TGA data from our lab (not shown) shows that there is still some solvent remaining at the onset of the transition when using the chloride system, Fig. 5.6 reflects that and, as a result, there is some time available for grain growth. Additionally, the lower E_a for the chloride system expands the coarsening window by extending the time between the end of the transition and the onset of decomposition. The acetate system has a low enough E_a that the crystallization occurs much faster and is complete with appreciable solvent still in the film and well before the onset of decomposition. Even though the annealing temperature used is the same as the chloride, the crystal growth is decoupled from both the salt removal and decomposition in time. In the previously referenced acetate report we provide evidence that the acetate is the only system we studied that shows coarsening of the crystal domains after complete crystallization and we refer the reader to that paper for details on the advantageous impact on both film morphology and the resulting device performance. Finally, in the nitrate system the three processes are decoupled in both time and temperature; the crystallization can occur in minutes and at room temperature. In fact, these three processes are so well decoupled that the salt removal can be accomplished by rinsing with a good anti-solvent for the perovskite rather than by heat. Unfortunately, the nitrate system has such a low E_a that the driving force for crystal growth, even at room temperature, is high enough to cause spherulitic growth which results in poor film morphology.[25]

Although Figure 5.6 is only intended to be a schematic representation of the crystallization process, it elucidates several key aspects of the film and crystal growth. First, the most widely reported systems, iodide and chloride, have very narrow processing windows and there is a high likelihood that films made at different times or in different labs would have a large deviation in their crystal properties and the film composition (e.g. the amount of remaining spectator salt). Secondly, Fig. 5.6 highlights the importance of decoupling the desired and undesired processes from each other and the impact that has on broadening the windows for grain growth and

coarsening. Decoupling these two processes can not be accomplished by temperature alone and a second experimental parameter is needed to fully tune the growth; one principal result of this study is the use of E_a as a second parameter. The kinetic effects of the lead salt provide a manner in which the desired processes can be decoupled from the undesired processes independent of the temperature.

5.4 Conclusions

We developed a method to extract the transformed fraction of methylammonium lead trihalide perovskite films by analysis of in situ WAXS data and used *x(t)* to select an appropriate kinetic model. We applied this model to extract E_a for the precursor-to-perovskite transition in thin films when depositing non-stoichiometric ratios of lead and methylammonium salts in DMF and show that the change in E_a is strongly dependent on the lead salt used. Finally, we added this knowledge of E_a to previously reported data to discern the composition for the precursor and show that controlling E_a, by changing the lead salt, allows for better crystal growth and has measurable and advantageous effects on the film morphology.

5.5 Experimental

Materials

All materials were used as received. Chloroform (anhydrous), *N,N*-dimethylformamide (DMF, anhydrous), ethanol (absolute), titanium(IV) isopropoxide (>97%), hydriodic acid (57 wt% in water), methylamine (33 wt% in ethanol), lead(II) nitrate ($Pb(NO_3)_2$) and lead(II) chloride ($PbCl_2$) were obtained from Sigma-Aldrich (St. Louis, MO) and used as received.

Salt and solution preparation

Methylammonium iodide (MAI) was prepared as previously published and stored in a desiccator.[11] Both organic and inorganic salts were pumped down in the glovebox antechamber overnight to remove any residual water. A 40 wt% solution of PbX_2 (where X=Cl, I, or NO_3) and MAI in a 1:3 molar ratio was prepared in a nitrogen glovebox by dissolving in DMF and stirring at low speed overnight. An

appropriate volume of the mother solution was removed in a sealed container and only exposed to ambient air at the time of film preparation.

Substrate Preparation

Films were made on silicon or glass substrates that had been cleaned by sequential sonication in acetone then isopropyl alcohol (IPA) for 5 minutes followed by rinsing with IPA and deionized (DI) water then UV-ozone (UVO) cleaning for 5 minutes. Just prior to spin coating the substrates were rinsed with IPA and DI water, dried under nitrogen flow and cleaned with UVO for 1-2 minutes.

Film Preparation

Perovskite films were made by depositing ~60 μL of 40 wt% solution and spinning at 2500 rpm for 30 s. Upon removal from the spincoater the substrates were placed on a heating stage in air that had been preheated to the annealing temperature noted in the text. The transfer time from the spincoater to the heating stage was typically 2-3 minutes; the time between placing the substrate on the preheated stage and the first image was typically 30-90 seconds.

GIWAXS Characterization

Samples were spin-coated at the Cornell High Energy Synchrotron Source (CHESS) and loaded on a custom-built temperature-controlled grazing incidence stage at the D1 beamline,[30] with a typical transfer period of 2-3 minutes. Two different detectors were used during the different runs: (a) Fuji image plates, 2500×2000 pixels with 100 μm/pixel resolution, placed in a holder at a distance of 177 mm and digitized using a GE Healthcare Typhoon FLA-7000 image plate reader, and (b) Pilatus 300 K high speed pixel array detector, 487×619 pixels with 172 μm/pixel resolution, at a distance of 107.5 mm from the sample. The x-ray wavelengths were set at 0.1161 nm and 0.1155 nm, respectively, for the different detectors. In both runs the incident beam angle was about 0.5°, well above the substrate critical angle. Typical exposure times were <2 seconds. To avoid beam induced damage in the perovskite films at higher beam flux, the sample was moved perpendicular to the beam in 0.5 mm increments

(the nominal beam width), and data collected from 16 to 28 different locations on the same substrate depending on the exact dimensions of the substrate used.

2D WAXS images were integrated using the Fit2D software package from ESRF; background substraction, the integrated peak areas and the calculation of *x(t)* were performed using IGOR, a commercially available software product.

5.6 References

1. McGehee, M. D. Fast-track solar cells. *Nature* **501,** 323–325 (2013).

2. Snaith, H. J. Perovskites: The Emergence of a New Era for Low-Cost, High-Efficiency Solar Cells. *J. Phys. Chem. Lett.* **4,** 3623–3630 (2013).

3. Kazim, S., Nazeeruddin, M. K., Grätzel, M. & Ahmad, S. Perovskite as light harvester: a game changer in photovoltaics. *Angew. Chem. Int. Ed. Engl.* **53,** 2812–24 (2014).

4. Zhou, H. *et al.* Interface engineering of highly efficient perovskite solar cells. *Science (80-.).* **345,** 542–546 (2014).

5. Saliba, M. *et al.* Influence of Thermal Processing Protocol upon the Crystallization and Photovoltaic Performance of Organic–Inorganic Lead Trihalide Perovskites. *J. Phys. Chem. C* **118,** 17171–17177 (2014).

6. Xiao, Z. *et al.* Solvent Annealing of Perovskite-Induced Crystal Growth for Photovoltaic-Device Efficiency Enhancement. *Adv. Mater.* n/a–n/a (2014). doi:10.1002/adma.201401685

7. Im, J.-H., Jang, I.-H., Pellet, N., Grätzel, M. & Park, N.-G. Growth of CH3NH3PbI3 cuboids with controlled size for high-efficiency perovskite solar cells. *Nat. Nanotechnol.* 1–6 (2014). doi:10.1038/nnano.2014.181

8. Kim, H.-S. *et al.* Lead iodide perovskite sensitized all-solid-state submicron thin film mesoscopic solar cell with efficiency exceeding 9%. *Sci. Rep.* **2,** 591 (2012).

9. Lee, M. M., Teuscher, J., Miyasaka, T., Murakami, T. N. & Snaith, H. J. Efficient hybrid solar cells based on meso-superstructured organometal halide perovskites. *Science* **338,** 643–7 (2012).

10. Jeon, N. J. *et al.* Solvent engineering for high-performance inorganic-organic hybrid perovskite solar cells. *Nat. Mater.* (2014). doi:10.1038/nmat4014

11. Liu, M., Johnston, M. B. & Snaith, H. J. Efficient planar heterojunction perovskite solar cells by vapour deposition. *Nature* **501,** 395–398 (2013).

12. Conings, B. *et al.* Perovskite-based hybrid solar cells exceeding 10% efficiency with high reproducibility using a thin film sandwich approach. *Adv. Mater.* **26,** 2041–6 (2014).

13. Eperon, G. E., Burlakov, V. M., Docampo, P., Goriely, A. & Snaith, H. J. Morphological Control for High Performance, Solution-Processed Planar Heterojunction Perovskite Solar Cells. *Adv. Funct. Mater.* **24,** 151–157 (2014).

14. Liu, D. & Kelly, T. L. Perovskite solar cells with a planar heterojunction structure prepared using room-temperature solution processing techniques. *Nat. Photonics* **8,** 133–138 (2013).

15. Chen, Q. *et al.* Planar heterojunction perovskite solar cells via vapor-assisted solution process. *J. Am. Chem. Soc.* **136,** 622–5 (2014).

16. Tan, K. W. *et al.* Thermally induced structural evolution and performance of mesoporous block copolymer-directed alumina perovskite solar cells. *ACS Nano* **8,** 4730–9 (2014).

17. Dualeh, A. *et al.* Effect of Annealing Temperature on Film Morphology of Organic-Inorganic Hybrid Pervoskite Solid-State Solar Cells. *Adv. Funct. Mater.* **24,** 3250–3258 (2014).

18. AuthLast, A. Reference Placeholder. *J. Name* **Vol,** XX

19. Colella, S. *et al.* MAPbI 3-x Cl x Mixed Halide Perovskite for Hybrid Solar Cells: The Role of Chloride as Dopant on the Transport and Structural Properties. *Chem. Mater.* **25,** 4613–4618 (2013).

20. Hadjichristidis, N., Pispas, S. & Floudas, G. in *Block Copolym. Synth. Strateg. Phys. Prop. Appl.* 313–334 (John Wiley & Sons, Inc., 2003). doi:10.1002/0471269808.ch17

21. Mittemeijer, E. J. Review Analysis of the kinetics of phase transformations. *J. Mater. Sci.* **27,** 3977–3987 (1992).

22. Liu, F., Sommer, F. & Mittemeijer, E. J. Analysis of the kinetics of phase transformations; roles of nucleation index and temperature dependent site saturation, and recipes for the extraction of kinetic parameters. *J. Mater. Sci.* **42,** 573–587 (2006).

23. Liu, F., Sommer, F., Bos, C. & Mittemeijer, E. J. Analysis of solid state phase transformation kinetics: models and recipes. *Int. Mater. Rev.* **52,** 193–212 (2007).

24. Avrami, M. Kinetics of Phase Change. II Transformation-Time Relations for Random Distribution of Nuclei. *J. Chem. Phys.* **8,** 212 (1940).

25. Moore, D. T., Sai, H., Wee Tan, K., Estroff, L. a. & Wiesner, U. Impact of the organic halide salt on final perovskite composition for photovoltaic applications. *APL Mater.* **2,** (2014).

26. Edri, E. *et al.* Why lead methylammonium tri-iodide perovskite-based solar cells require a mesoporous electron transporting scaffold (but not necessarily a hole conductor). *Nano Lett.* **14,** 1000–4 (2014).

27. Zhang, W. *et al*. Ultra-smooth organic-inorganic perovskite thin-film formation and crystallization for Efficient Planar Heterojunction Solar Cells. *Submitted Aug. 2014*

28. You, J. *et al.* Low-temperature solution-processed perovskite solar cells with high efficiency and flexibility. *ACS Nano* **8,** 1674–80 (2014).

29. Zhao, Y. & Zhu, K. CH 3 NH 3 Cl-Assisted One-Step Solution Growth of CH 3 NH 3 PbI 3 : Structure, Charge-Carrier Dynamics, and Photovoltaic Properties of Perovskite Solar Cells. *J. Phys. Chem. C* **118,** 9412–9418 (2014).

30. Bian, K. *et al.* Shape-Anisotropy Driven Symmetry Transformations in Nanocrystal. 2815–2823 (2011).

5.7 *Supporting Information*

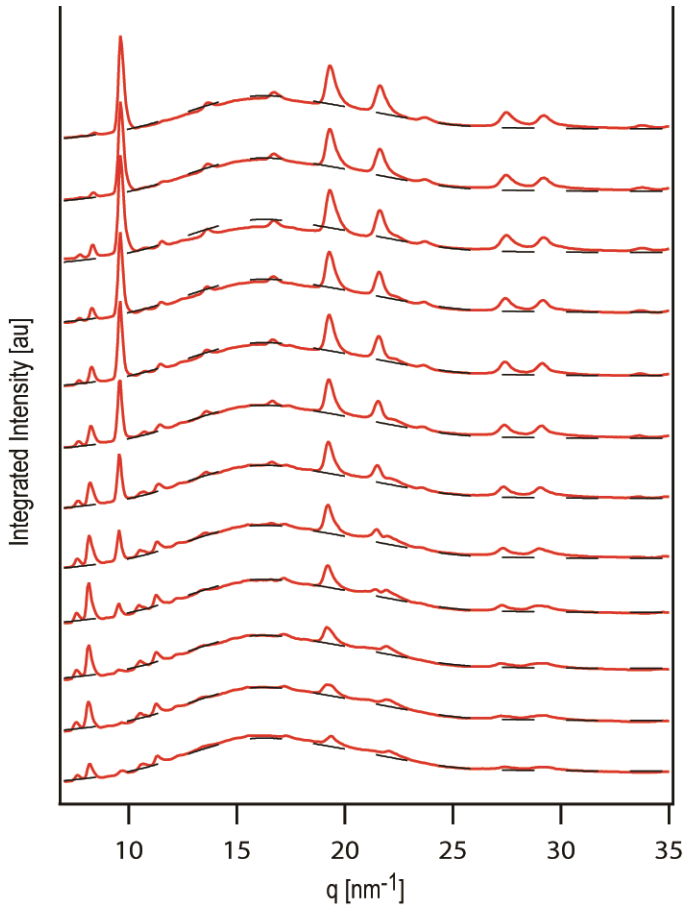

Figure 5.7: 1D radial plots of scattering images from the chloride system integrated over all azimuthal angles. Traces are taken at ~10 min. intervals and are shown prior to background subtraction to demonstrate the consistency of the background signal. Black dashed line is the background signal fit for the trace at t=50 min., the line is superimposed on top of all traces for comparison.

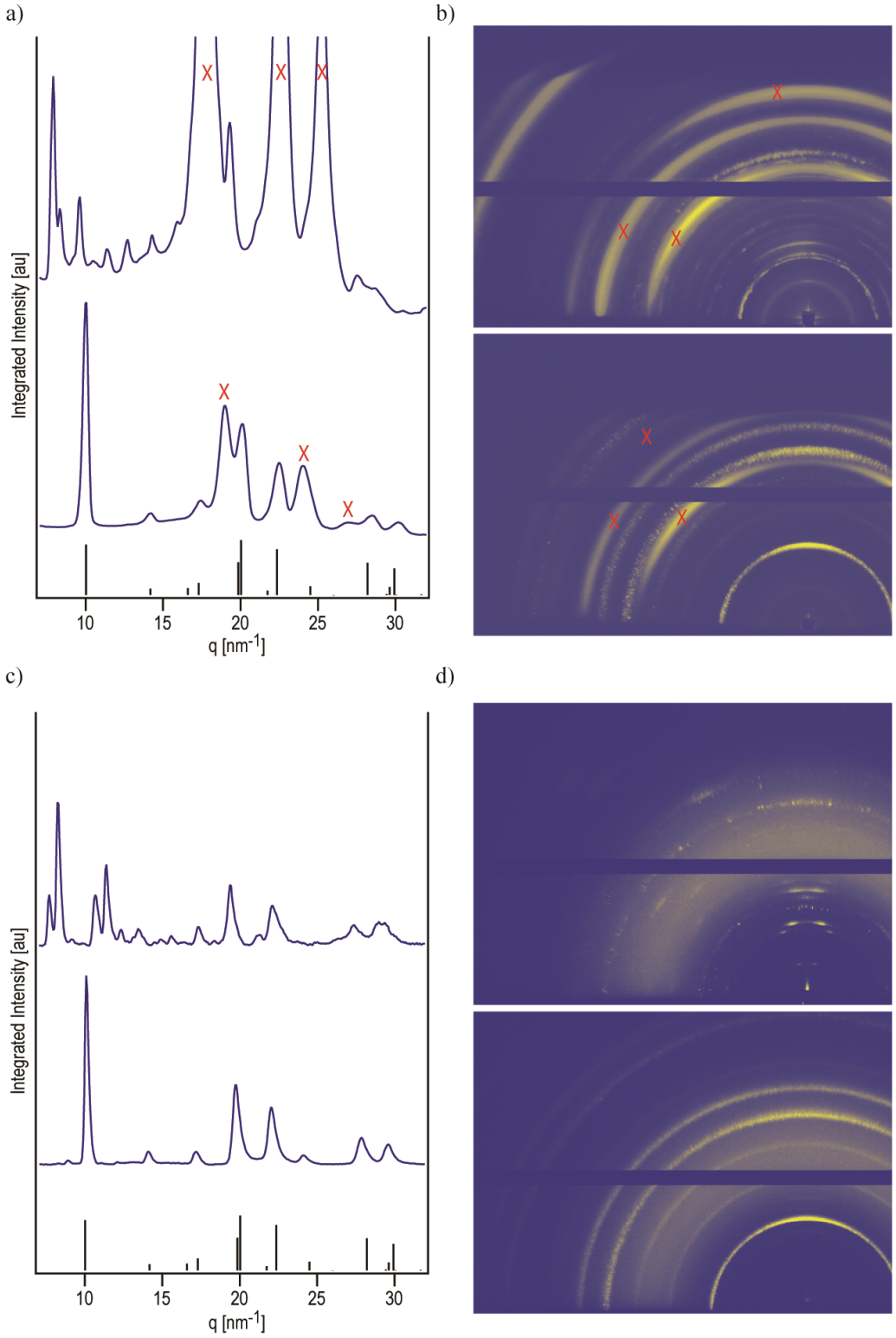
a)
b)
c)
d)
Integrated Intensity [au]
q [nm-1]
10
15
20
25
30
X

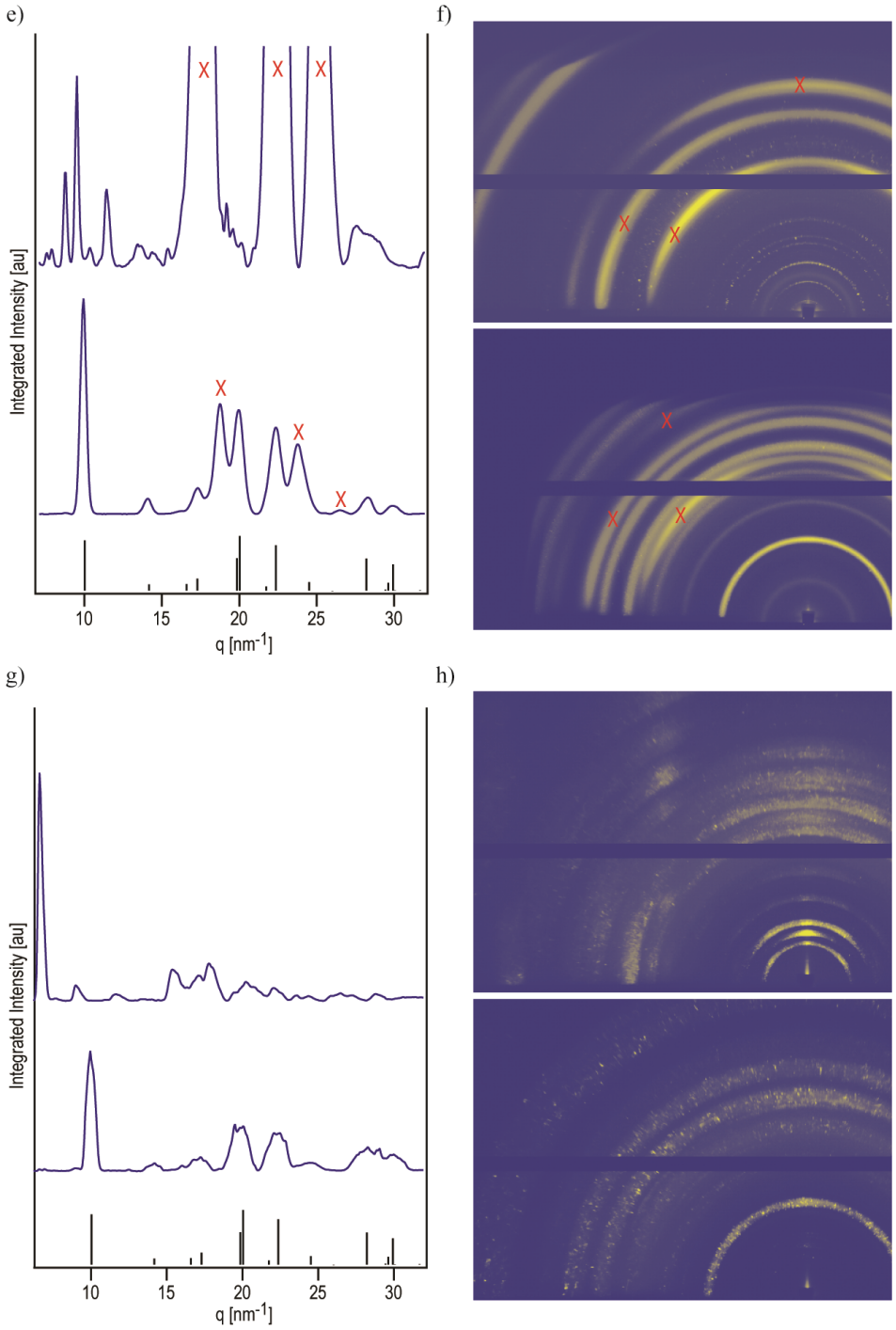

Figure 5.8: 1D and 2D scattering data for the precursor and perovskite material for the iodide (a,b), chloride (c,d), acetate (e,f) and nitrate (g,h) systems. (a,c,e,g) show the integrated plots of the precursor (top) and perovskite (bottom) along with the calculated peak locations for the tetragonal iodide perovskite (black stick markers). (b,d,f,h) are the raw 2D plots from which the respective 1D plots were generated. The iodide and acetate systems were made on TiO_2 substrates and the peak locations for the TiO_2 are marked with red "X"s on both the 1D and 2D plots.

Calculation of pathway process bars

	Evap Solvent	From TGA we know how long it takes DMF to evaporate, we know DMF isn't in the lattice so we set the start of this to t=0 and the length of time to the value derived from TGA data; we assume the lead salt doesn't change the evaporation rate of the solvent.
	Diffuse MASp	This process is the removal of the spectator from the precursor and is, essentially, the precursor-to-perovskite transition. Both the lag time and the total time for this process are calculated from the WAXS data and the kinetic parameters.
	Sublime MASp	This is the removal of the "amorphous" spectator from the film (not the lattice). The start time is set based on the assumption that it begins as soon as there is amorphous MASp to be removed, so it lags the diffusion by a short time in all cases. This process can't end until the diffusion is complete. Once diffusion is complete, in all cases we have a perovskite film with some MASp laying around, so we set the time between completion of diffusion and the end of sublimation based on the volatility of MASp
	Diffuse MAI	This is the removal of MAI from the perovskite, it is the decomposition. The case of all iodide is easiest to consider as MASp=MAI; therefore, we assume that the diffusion of MAI from the lattice (precursor or perovskite) is continuous. The delineation between the desirable process and the decomposition is just a matter of counting the number of MAI units removed from the lattice; thus, the start of decomposition coincides with the end of the Diffuse MASp step. The case of non-iodide MASp is the most difficult to assess, for chloride it is based on experimental observation. For acetate and nitrate, the timing of the first three processes suggests that all three are complete before decomposition begins. Therefore we select a lag time for the start of decomposition at 100 °C and set it the same for both systems. *Note: the length of this bar on the chart is random, it actually continues until only PbI_2 is left.*
	Growth	Time available for perovskite grain growth, begins when the transformation begins and ends when the MASp is completely removed from the lattice OR when the solvent is gone, whichever comes first. i.e. growth only occurs while both precursor and solvent still exist.
	Coarsen	Time available for coarsening. This begins when MASp is done diffusing from the lattice and ends when decomposition begins.

CHAPTER 6 CONCLUSIONS

In this work I have presented several studies that investigate different aspects of the crystallization of the methylammonium lead halide perovskites, particularly in thin film configurations for solar energy applications. After briefly investigating the implications of the absorption profile on the theoretical efficiency of PV cells, I turned my attention to the methylammonium lead halide perovskites. I began this dissertation by asking three principal questions and, hopefully, have convinced the reader that the answers presented are appropriate and correct.

As to our observations we successfully correlated several key processing-structure relationships as well as their impact on performance. Chapter 3 detailed the impact of the effect of air during processing and the effect of an isochronal annealing profile. The presence of air during crystal formation speeds up the crystal evolution substantially, highlighting the importance of an inert environment during processing. The effect of an isochronal temperature profile is shown to dramatically improve the film morphology which, in turn, is correlated to increased PV device performance as determined by the J_{sc}, V_{oc}, FF, and overall efficiency. Further, it was shown that the introduction of an immediate step to 130 °C, at the end of the temperature ramp, improved the crystal surface roughness and domain size while maintaining the advantages of the temperature ramp on the film morphology. This rapid step to 130 °C was also correlated to increased efficiency mostly due to an increased J_{sc}.

Chapter 4 explored the mechanism of topotacticity in both reagent salts used to prepare $(MA)PbI_3$. We found that all salts are completely dissociated during the crystallization and, when either or both salts are in the solid state at the beginning of the reaction, the resulting perovskite is fully determined by the anion concentrations in the solution or vapor phase. This led to the idea that the crystal formation was insensitive to the lead source. We proved this concept by showing formation of the iodide perovskite using lead nitrate as the lead source.

The final results presented are in regards to the kinetics of the precursor-perovskite transition and were presented in Chapter 5. This study detailed a methodology for tracking the transformed fraction of a film using WAXS data and

applied that method to construct Arrhenius plots for two kinetically disparate systems; $(MA)PbI_3$ using either chloride or nitrate lead salts for the lead source. For the chloride and nitrate based systems we determined activation energies of 86 kJ/mol and 57 kJ/mol respectively, additionally, we used a single set of isothermal data to determine the relative speed of the iodide and acetate systems. The iodide system was found to have the highest E_a with the E_a of the acetate falling between the chloride and nitrate, although for these systems we cannot extract specific values. We use the kinetic results, along with previous data, to determine the general formula for the precursor phase which consists of formula units of the perovskite along with excess MAX salts. This explains the order of the activation energies as well as providing some insight into the mechanisms by which the perovskite forms.

The value of this work, and the work detailed in a few recent reports, is to show new potential pathways to templating optimal film growth. Decoupling the temperature from the driving force and activation energy will allow for broader and better control of the crystal growth. Control of the crystal growth will not only lead to continued performance improvements, it will also allow for an expanded study of the fundamental optical and electronic properties of this exciting new class of materials.

APPENDIX A: ULTRA-SMOOTH ORGANIC-INORGANIC PEROVSKITE THIN-FILM FORMATION AND CRYSTALLIZATION FOR EFFICIENT PLANAR HETEROJUNCTION SOLAR CELLS

Wei Zhang, Michael Saliba, David T. Moore, Sandeep K. Pathak, Maximilian T. Hörantner, Thomas Stergiopoulos, Samuel D. Stranks, Giles E. Eperon, Jack A. Webber, Antonio Abate, Aditya Sadhanala, Shuhua Yao, Yulin Chen, Richard H. Friend, Lara A. Estroff, Ulrich Wiesner & Henry J. Snaith

A.1 Abstract

Organic-inorganic metal halide perovskite solar cells have emerged over the last two years, captivating the research community. To date, there have been a plethora of reports on different means to fabricate thin films, but the inorganic starting materials have been limited to halide based anions. Here, we study the role of the anions in the perovskite solution and their influence upon perovskite crystal growth, film formation and device performance. We find that by using a non-halide lead source (lead acetate) instead of lead chloride or iodide, the perovskite crystal growth is much faster, which allows us to obtain ultra-smooth and almost pinhole-free perovskite films by a simple one-step solution coating with only a few minutes annealing. This synthesis leads to improved device performance in planar heterojunction architectures and answers a critical question as to the role of the anion and excess organic component during crystallization. Our work paves the way to tune the crystal growth kinetics by simple chemistry.

Perovskite solar cells have rapidly become an emerging photovoltaic (PV) technology, which has evoked widespread scientific and industrial interest[1-9]. The light absorbing material is an organic-inorganic trihalide perovskite with an ABX_3 structure (where A is an organic cation, B a divalent metal ion, and X a halide Cl, Br or I or any mixture thereof). Typically, this is methylammonium lead triiodide $CH_3NH_3PbI_3$ or mixed-halide variants $CH_3NH_3PbI_{3-x}Cl_x$ and $CH_3NH_3PbI_{3-x}Br_x$ which can be synthesized simply from cheap materials, in contrast to traditional semiconductors. Thin films can also be fabricated by various deposition procedures including simple one-step solution coating[1-3], sequential dip coating[4], vapour phase deposition[5] or

combinations thereof[10], similarly versatile to organic semiconductors. In contrast to the latter though, perovskites exhibit excellent crystallinity, ambipolar transport[3] and large diffusion length for both electrons and holes[11,12]. Since the seminal work by Miyasaka and co-workers in 2009, who showed a 3.8% efficient perovskite sensitized solar cell employing a liquid electrolyte[13], various device structures ranging from sensitized solar cells on mesoscopic semiconducting TiO_2[2-4] or insulating Al_2O_3 scaffolds[1,14], to the planar heterojunction (PHJ) architecture[5,7,11], have been explored. To date, through optimizing device design, material interfaces, and processing techniques, a recorded efficiency of 17.9% has been reported[15], in a device which is a combination of a mesoporous infiltrated anode with a solid perovskite thin film. These recent developments demonstrate the enormous potential of perovskite solar cells, with trajectory suggesting that they should soon compete with traditional silicon solar cells.

Although the performance of perovskite solar cells has improved rapidly in the last two years, the basic properties of organic-inorganic trihalide perovskites are not well understood. A lot of recent work exploring the absorber material has focused on tuning the band gap by changing the ratio of the anions[16], cations[17], or the divalent metal[18,19]. However, the impact of the solution composition on perovskite crystal growth and film formation, and thus on the device performance, is still under scrutiny[20,21]. For example, it is challenging to form a smooth and continuous perovskite film on compact TiO_2 (c-TiO_2) coated fluorine-doped tin oxide (FTO) substrates by one-step solution coating of a solution containing lead iodide (PbI_2) (or lead chloride ($PbCl_2$)) blended with methylammonium iodide (CH_3NH_3I)[22,23]. A non-continuous perovskite film is usually obtained, where pinholes can introduce shunting pathways limiting the solar cell performance. In addition, although the different electrical and photo-physical properties have been observed for the "mixed-halide" perovskite $CH_3NH_3PbI_{3-x}Cl_x$ as compared to $CH_3NH_3PbI_3$[11,12], the existence and role of Cl in mixed-halide perovskite are still debatable and the varied results from groups employing different characterization techniques are hard to reconcile[1,20,23-26]. We have previously found that by employing a large excess of organic component (CH_3NH_3I)

much larger crystalline domains can be formed[1], and smoother films can be created than those processed from a stoichiometric mix of CH_3NH_3I and PbI_2[11]. However, the role and the fate of the excess organic component during film formation and crystallization remain mysterious. A complete understanding of these issues is hence critically important for advancing our understanding of perovskite semiconductors and solar cell performance.

In this work, we employ several lead salts, lead chloride ($PbCl_2$), lead iodide (PbI_2), and lead acetate ($PbAc_2$) in conjunction with a 3 molar excess of methylammonium iodide (CH_3NH_3I). All material processing routes lead to the formation of $CH_3NH_3PbI_3$ with undetectable amounts of the "spectator" anion (Cl or Ac) but with considerably different thin film properties. In the latter case, $PbAc_2$, the only halide source in the final perovskite film is from CH_3NH_3I, which helps to identify more clearly what role the spectator ion (Cl or Ac) plays during perovskite film formation. Our findings reveal that the anion has a substantial effect on the perovskite crystal growth kinetics and film morphology. By simple one-step solution coating using $PbAc_2$ as lead source, we obtained a compact perovskite film with full-coverage on the substrate. Surprisingly, the smoothness of the films surpasses that of vapor-deposited films. Additionally, the processing time is greatly reduced to a few minutes for the $PbAc_2$ route due to the more rapid loss of excess organic material and ensuing faster crystal growth. By optimizing device fabrication conditions, we achieve a power conversion efficiency of 15.2% in a planar heterojunction architecture through the $PbAc_2$ route, measured under one sun illumination, which is a significant improvement upon similar solar cells fabricated from either $PbCl_2$ or PbI_2 routes.

A.2 Results

A.2.1 Crystallographic structure and evolution of perovskite

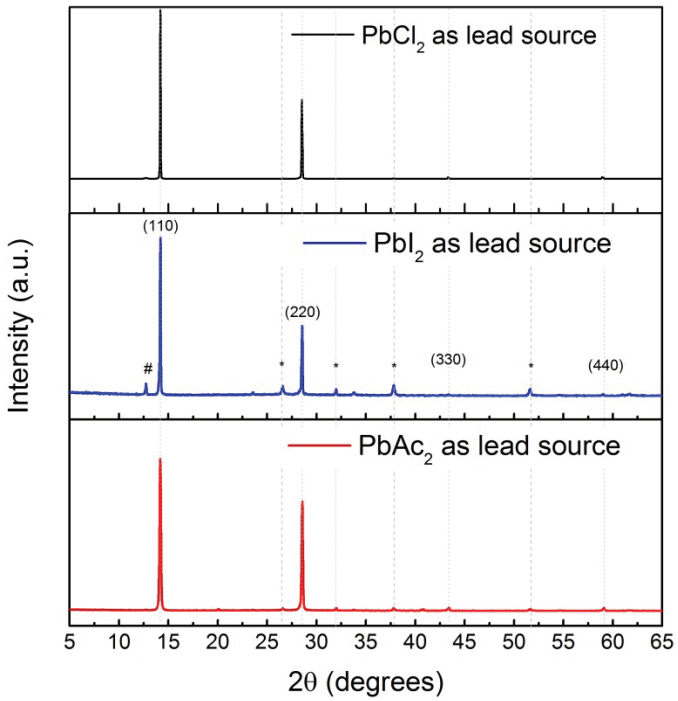

Figure A.1: X-ray diffraction spectra for perovskite films deposited on a FTO/c-TiO_2 substrate from the reagent solution containing different lead sources (lead chloride, lead iodide and lead acetate). Peaks are assigned to the reflections from a tetragonal perovskite lattice with unit cell parameters a=b=8.85Å, c=12.64Å. Peaks marked with * and # are assigned to the fluorine-doped tin oxide (FTO), and traces of PbI_2, respectively.

We prepared different perovskite solutions by mixing 3:1 (by moles) of CH_3NH_3I:PbX_2 in N,N-Dimethylformamide (DMF), where X is Cl, I or Ac. It is noted that we do not use a ratio of 1:1 of CH_3NH_3I:PbI_2 as the focus of this study is to elucidate the role of anions when processed with excess organic component, as we employ in our conventional "mixed halide" perovskite $CH_3NH_3PbI_{3-x}Cl_x$. We fabricated films on FTO/c-TiO_2 substrates by one-step solution coating of different perovskite solutions in a nitrogen filled glovebox. The perovksite films made from solutions using $PbCl_2$ or $PbAc_2$ as lead source were annealed at 100°C in the glovebox after spin coating. Since the perovskite does not form at 100°C from the solution using PbI_2 as lead source, even after 12 hours annealing, the temperature was increased to

150 °C for this PbI_2 route. The annealing times were optimized separately for each route to achieve best solar cell performance (see Methods). In Figure A.1, we show the XRD patterns of perovskite films fabricated using different lead sources. From the XRD reflections it is evident that the materials fabricated from perovskite solutions with different lead sources are invariably the same in their crystal structure. XRD reflection confirms the $CH_3NH_3PbI_3$ perovskite structure with lattice parameter with **a**=**b**=8.85 Å and **c**=12.64 Å[13].

From analysis using the Scherrer equation, the crystal sizes of perovkites made from $PbCl_2$, PbI_2 and $PbAc_2$ routes are estimated to be >500 nm (larger than machine resolution), 305±65 nm and 135±45 nm, respectively. It is important to note that these values are based on the assumption of spherical perovskite crystals. In contrast, for our samples, due to the film thickness limitation, crystals are much larger parallel than perpendicular to the substrate, meaning that the crystal size is underestimated by the Scherrer equation analysis. Considering that all samples have similar film thickness (Figure A.4), it is safe to assume that the observed size trend is still valid. In addition, scanning electron microscope (SEM) images shown below are consistent with the $PbAc_2$ route delivering smaller crystals.

To understand the evolution of the perovskite crystal formation using different lead sources, we performed in-situ wide-angle X-ray scattering (WAXS). Figure A.2a-c show a series of 1D plots obtained from 2D data sets which have been integrated over all azimuthal angles. Similar to previous reports, we note a "precursor" material formed prior to the perovskite crystallization[27]; although each system exhibits a different diffraction pattern for the "precursor" structure, they are all distinguishable from the perovskite pattern. The kinetics of the systems are assessed by tracking key "precursor" peaks (marked in Figures A.2a-c on the bottom-most traces) and defining t_{end} as the time when all "precursor" peaks are gone. The $PbAc_2$ and $PbCl_2$ based films are annealed at the same temperature and can be compared straight away with t_{end}=2.5 min. and t_{end}=43.8 min., respectively. The PbI_2 based film was annealed at 150 °C and has a t_{end}=17.8 min. In a previous experiment we annealed $PbCl_2$ films at 130 °C and

found t_{end}~8-10 min. From this data we can extrapolate that perovskite crystal formation is faster from $PbCl_2$ route than from PbI_2 route, and fastest from $PbAc_2$ route leading to the following order: $PbAc_2$ >> $PbCl_2$ > PbI_2.

In addition to providing a relative comparison of the kinetics of the three systems, the WAXS data also reveal information about the crystal texture and coarsening. Panels d-f in Figure A.2 show 2D perovskite patterns obtained at t_{end}. The dashed red lines note the location of the (110) peaks that are radially integrated resulting in line scans as shown in panels g-i. The less spotty 2D pattern and a weak dependence of peak intensity on azimuthal angle for the $PbAc_2$ based film suggests a material with smaller grains and weaker crystallographic orientation, as expected from the faster rate of crystallization. Overall, the $PbCl_2$ based film shows a similar orientational behavior as the PbI_2 based one, but with larger crystal sizes. We attribute this difference to longer overall annealing times at lower temperatures allowing for better crystal growth prior to the beginning of decomposition. It should be noted that these are crystal morphology effects that need to be distinguished from film morphology effects discussed further below.

Figure A.2j-l shows the (110) peak intensity for each film beginning just prior to the time when all "precursor" peaks are gone, t_{end}, and extending to the end of the experiment. While for PbI_2 and $PbCl_2$ based films the complete transformation to the perovskite is immediately followed by a decrease in peak intensity, for the $PbAc_2$ based film the intensity first increases after the perovskite is fully formed and only then decreases on a time scale slower than the time scale for perovskite formation. Since the scattering intensity decrease in all samples can be attributed to decomposition into PbI_2, as verified by the respective decomposition peaks occurring at later time points, we can ascertain key information about the crystal evolution from Figure A.2l. First, we ascribe the initial increase in peak intensity for $PbAc_2$ based film to the film coarsening not present for PbI_2 or $PbCl_2$ based films. Second, we note that when the (110) peak intensity of the $PbAc_2$ based film does decrease, the peak

intensity still remains above its value at t_{end} implying a slower decomposition relative to the crystallization time.

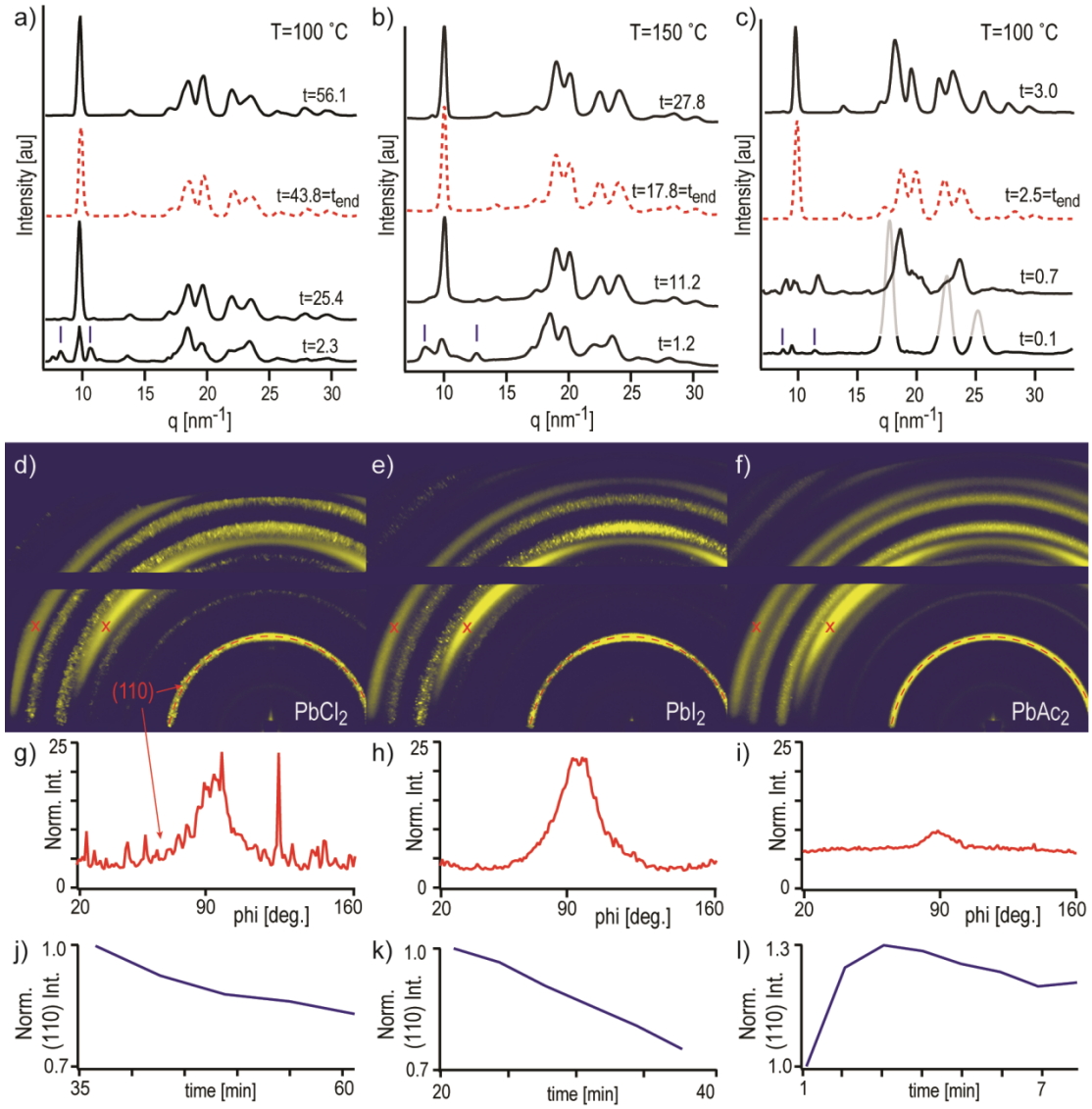

Figure A.2: In-situ WAXS data for all three systems. Azimuthally integrated 1D plots at several key time points (t, in minutes) of annealing for films made from (a) $PbCl_2$, (b) PbI_2, and (c) $PbAc_2$ routes. Red dashed traces indicate the point of complete perovskite transformation, blue stick markers on the bottom-most traces note the peaks used to track the "precursor" structure; the three gray peaks in (c) are from the TiO_2 substrate and have been grayed out for clarity. (d-f) 2D WAXS images corresponding to t_{end} of the respective samples in a-c. Two rings marked with a red "x" are from the TiO_2 substrate, horizontal line is the detector seam; red dashed line is the (110) peak for the tetragonal perovskite. (g-i) Azimuthal line scans for (110) peak at 10 nm^{-1} (q vector) radially integrated between 9.9-10.1 nm^{-1} and normalized such that the entire integrated area = 1000. (j-l) Peak intensity of the (110) peak normalized by the intensity at t_{end} (defined in text). Plots begin approx. 1 time point prior to t_{end} and extend to the end of the experiment.

The transition process of starting materials into perovskite is generally described by the following equation:

$$PbX_2 + 3\ CH_3NH_3I \rightarrow CH_3NH_3PbI_3 + 2\ CH_3NH_3X\ (X = Cl, I, Ac)$$

The above reaction typically involves the evaporation of solvent, sublimation/evaporation of the by-product (CH_3NH_3X), crystal nucleation and growth, etc[28]. As shown in the WAXS study, the anneal time is much shorter for perovskite made from $PbAc_2$ route than $PbCl_2$ and PbI_2 routes, which could be correlated to the ease with which the by-product can be removed during perovskite film formation. To confirm this hypothesis, we recorded the thermal gravimetric analysis (TGA) curves for the by-product CH_3NH_3X (X= Cl, I, Ac). As shown in Figure A.3, the initial decomposition temperature (defined by T at 95% weight) is 97.4, 226.7 and 245.0 °C for CH_3NH_3Ac, CH_3NH_3Cl and CH_3NH_3I, respectively, which is consistent with the trend of the maxima, T_d, of the derivative weight loss/temperature curves for which $T_d(CH_3NH_3Ac) \ll T_d(CH_3NH_3Cl) < T_d(CH_3NH_3I)$. This data indicates that the CH_3NH_3Ac is thermally unstable and much easier removed than CH_3NH_3Cl and CH_3NH_3I at the adopted processing temperature range. Thus, at the same annealing temperature, the nucleation density is much higher for the films processed from $PbAc_2$ route, which tend to form a large amount of relatively small crystals on a short time scale (1-2 min) and fully cover the substrate. In contrast, for the $PbCl_2$ and PbI_2 routes, the CH_3NH_3Cl and CH_3NH_3I need longer annealing times to be removed. As a result, the nucleation density is lower leading to large crystals[11,22]. In addition, non-continuous films are frequently observed which could be due to the thermal energy enabling pore growth to occur before the perovskite film is crystallized [22].

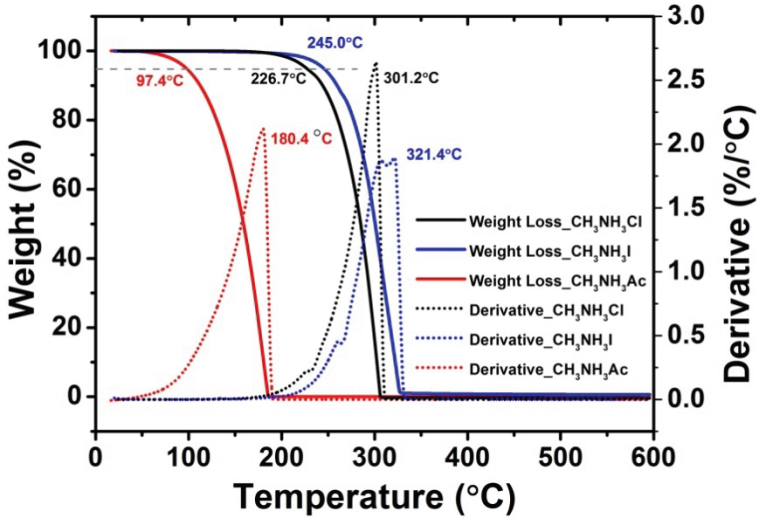

Figure A.3: TGA curves and their derivatives for CH_3NH_3X (X= Cl, I, Ac) in nitrogen atmosphere.

For perovskites made from $PbAc_2$ or PbI_2 routes, the presence of only one type of halide in the reagent solution, i.e. I^-, ensures the formation of methylammonium lead triiodide ($CH_3NH_3PbI_3$) crystals. In contrast, the perovskite obtained from the reagent solution with $PbCl_2$ contains both I^- and Cl^-, giving the more complicated possibility of forming a mixed halide perovskite ($CH_3NH_3PbI_{3-x}Cl_x$). Interestingly, in the mixed halide perovskite the exact location and the concentration of the Cl^- remains unclear to date, with varying observations by several groups[1,20,23-26]. The difficulty of detecting the Cl^- in the mixed halide perovskite may partly be due to the detection limit of the techniques used, but the fact that often only small quantities are observed suggests that the final content in the films may be very low. Here, we employ oxygen flask combustion-potentiometric titration method to detect the Cl^- concentration in the perovskite[29], which reaches down to the level of 30 ppm, a much higher resolution than the traditional analytical methods adopted so far[1,20,23-26]. For the perovskite films prepared via $PbCl_2$ route, the titration process showed no change of electric potential corresponding to Cl^-, suggesting an upper bound of the concentration of Cl^- in the final films of 30 ppm (mass ratio). Even if we take into account other possible experimental errors (e.g. sample weighing, solution volume error, etc.) and relax the error by 10 times (very conservative), the Cl^- is less than 300 ppm (mass ratio). This then led us to believe that the predominant phase in the mixed halide approach ($PbCl_2$ as lead

source) is $CH_3NH_3PbI_3$, similar to the pure iodide source. (i.e. reagent solution with PbI_2). We note that such results are based on the films deposited on flat substrates rather than on mesoscopic structures (TiO_2 or Al_2O_3). Whether the Cl^- will remain at the interface in mesoscopic structures still needs further scrutiny[30]. We also note that the predominant absence of Cl^- in the final film is consistent with the by-product (CH_3NH_3Cl) of the reaction between CH_3NH_3I and $PbCl_2$, evaporating from the film during annealing. Even though the bulk TGA results suggest that the CH_3NH_3Cl should be thermally stable until 230℃, lowering of this temperature in a thin film is expected due to the relative increase in surface area relative to volume. Therefore, if there is remnant unreacted organic-halide within the film, it is at a very low level.

A.2.2 Perovskite film morphology

The composition of the perovskite solution and the temperature and rate at which the by-products are driven out of the film directly influence the crystallization rate, crystal size and film morphology. To illustrate this we show scanning electron microscope (SEM) images of the respective perovskite films deposited from the different perovskite solutions in Figure A.4. The perovskite films made from $PbCl_2$ (a) and PbI_2 (b) routes are non-continuous with pinholes on different length-scales. For the $PbCl_2$ route, the crystalline platelets appear to be on the 10's of micrometer length scale with large voids between them. This appearance is consistent with literature reports on similar films[22]. For the PbI_2 route, the pore size scale is much smaller, on the order of 100's of nanometers. However, there are no clear crystalline grain boundaries on this same length scale, and coupled with the XRD results we presented earlier, this is consistent with the PbI_2 route delivering a porous crystalline film, rather than micro pores between crystalline grains. The perovskite films derived from $PbAc_2$ (c) route exhibit a considerably different morphology attaining almost full coverage on the substrates with an absence of pinholes. Crystal grains are apparent that range from a few hundred nm to 1 micrometer in size (c, inset). In addition, from the cross-section SEM images we can observe that the perovskite films derived from $PbAc_2$ route are much smoother (f) than films made from $PbCl_2$ (d) and PbI_2 (e) routes, which in contrast show an undulating nature.

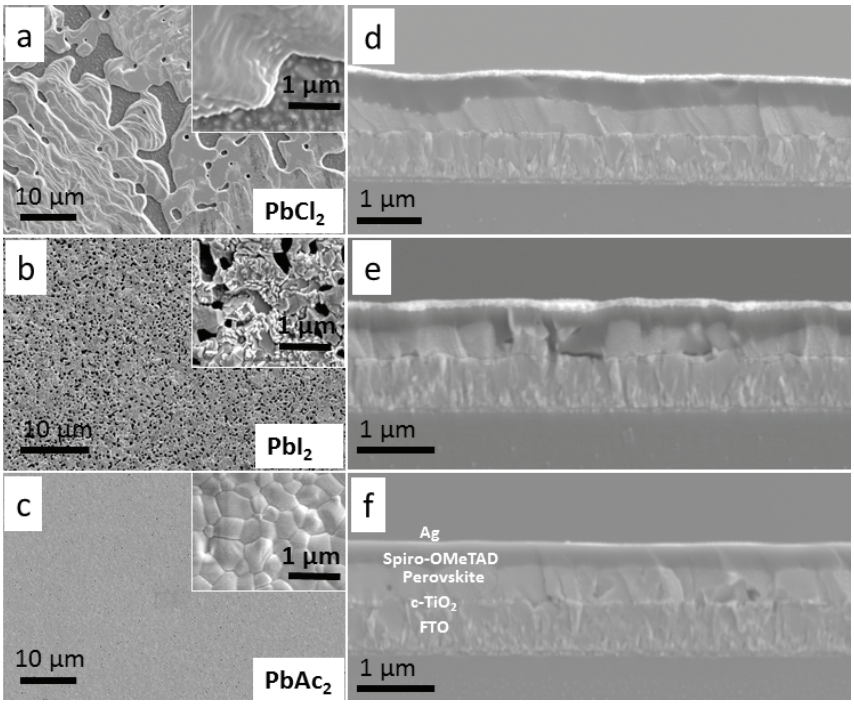

Figure A.4: SEM images of perovskite films deposited on FTO/c-TiO2 substrates from the three different lead sources PbCl2 (a), PbI2 (b) and PbAc2 (c), (insets show images with higher resolution); cross-sections of full devices with the perovskite derived from PbCl2 (d), PbI2 (e), and PbAc2 (f) routes.

We further characterized the films derived from different lead sources by atomic force microscopy (AFM) as shown in Figure A.5. We calculated the root mean squared roughness of the perovskite films made from $PbCl_2$ (Figure A.5a), PbI_2 (Figure A.5b) and $PbAc_2$ (Figure A.5c) routes to be 62.4, 52.2 and 12.3 nm respectively, for areas of 15 µm × 15 µm. The roughness of films fabricated via $PbAc_2$ route is greatly reduced compared to traditional one-step solution coating, as is evident from both, AFM line segments (Figure A.5e) and height distribution analysis (Figure A.5f). It is worth emphasizing that there is a lack of pinholes for the $PbAc_2$ derived film as compared to films from both $PbCl_2$ and PbI_2 (see circles in Figure A.5a,b). In addition, we show the surface AFM image of films produced by dual source vapour deposition of CH_3NH_3I and $PbCl_2$[5], which until now has delivered much smoother and more continuous films than solution coatings. It is encouraging that by choosing the appropriate anion of the lead source, the smoothness of the perovskite films made by a

simple one-step solution coating are even better than those of the vapor-deposited films based on $PbCl_2$ (16.2 nm, Figure A.5d) or PbI_2 (23.2 nm)[10].

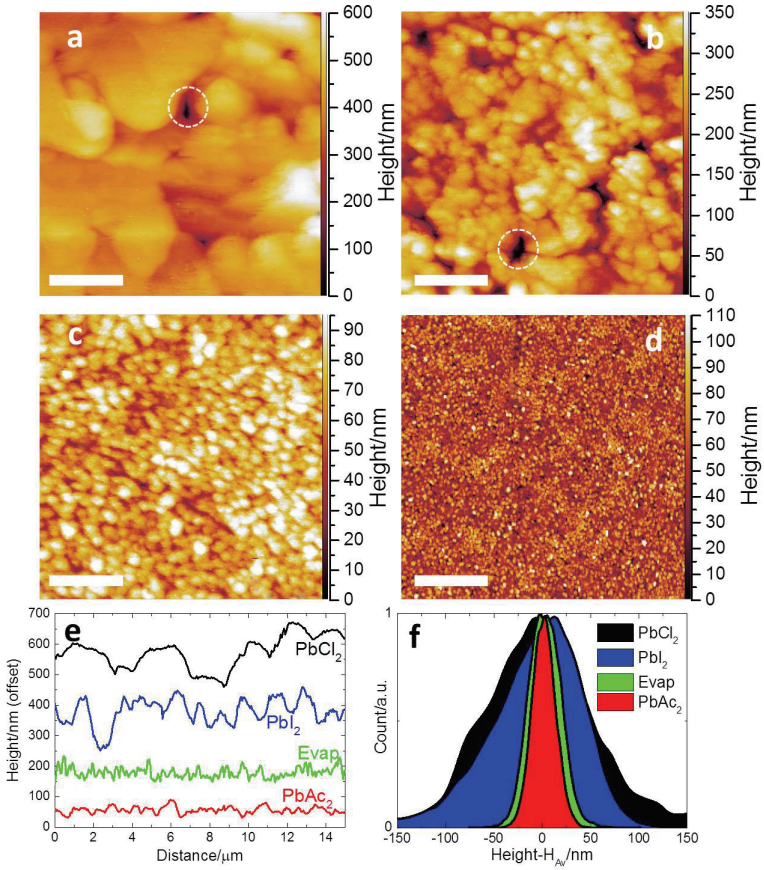

Figure A.5: AFM images of perovskite films deposited on a FTO/c-TiO_2 substrate derived from the three different lead sources, $PbCl_2$ (a), PbI_2 (b), $PbAc_2$ (c), and a vapor-deposited film based on $PbCl_2$ (d). The scale bars are 4 μm. Examples of pinholes in $PbCl_2$ and PbI_2 derived films are circled, which are notably absent in the film from $PbAc_2$. Line segments from each scan (e) and the height distribution (f) around the average height, H_{Av}, show the exceptional smoothness of the $PbAc_2$ derived films.

A.2.3 Optical properties of the perovkite films

We show the absorption and photoluminescence (PL) spectra of perovskite films derived from the different lead sources in Figure A.6a. We observe similar absorption edges and sharp PL spectra at about 775 nm for all samples, consistent with non-detectable Cl or Ac in the perovskite structure. The PL spectra for films derived from PbI_2 and $PbAc_2$ routes are slightly blue-shifted with respect to the $PbCl_2$ derived film. The magnitude of the shift correlates inversely with the observed crystal size,

which is consistent with recent findings by De Bastiani *et al*., who saw that small perovskite crystallites result in blue-shifted emission relative to perovskite crystals which are free to grow without any constraints[31]. We note that this is unlikely to be a quantum confinement effect due to the relatively large size of all crystals, but may be due to crystal strain induced or relaxed at the grain boundaries.

We used photothermal deflection spectroscopy (PDS) to measure the optical absorption of the perovskite films near the band edge with high sensitivity and show the results in Figure A.6b. As was recently reported by De Wolf *et al.* and Sadhanala *et al.* for $CH_3NH_3PbI_3$, we observe sharp band edges for all the samples with an exponential decay of the density of states at the band edge, known as the Urbach tail.[32] [33] The extent of the absorption tail below the band gap is correlated with the degree of electronic disorder within the material, which could originate from thermal fluctuation of the ions composing the material but also from defects of the crystalline structure. Indeed, several recent modelling works reported that defects within $CH_3NH_3PbI_3$ perovskite crystals would result in localized states in the range of a few hundred meV from the extended states of the bands, which will be detected as a broadening of the Urbach tail[34]. Assuming the same level of thermal disorder, the slope of the exponential part of the Urbach tail gives an estimation about the concentration of these defects, in terms of Urbach energy 'E_u' [32,33]. The estimated Urbach energies for samples derived from $PbCl_2$, PbI_2 and $PbAc_2$ routes are shown in the inset of Figure A.6b, along with the respective fitting error, and are 14.0, 15.8 and 14.4 meV, respectively. These values suggest that within the measurement error, PbI_2 derived perovskite has a higher level of electronic disorder compared to both $PbCl_2$ and $PbAc_2$ derived perovskites.

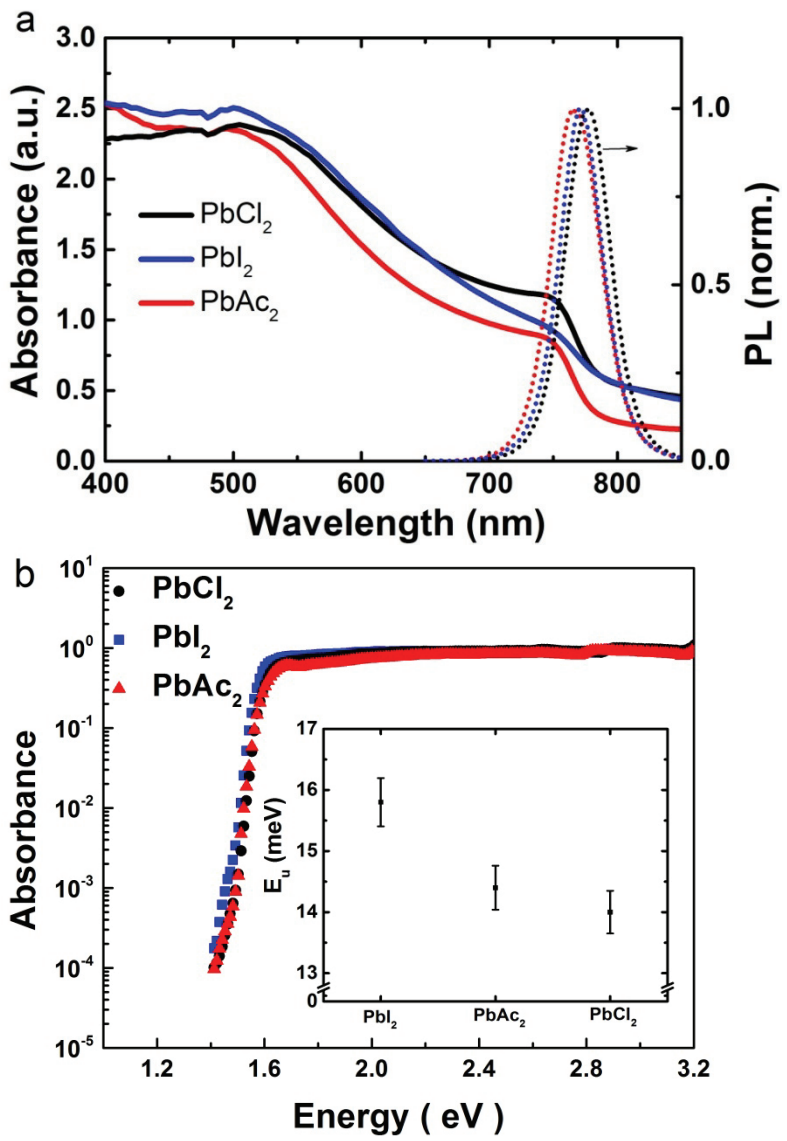

Figure A.6: (a) UV-Vis absorption spectra for perovskite films deposited on FTO/c-TiO_2 substrates derived from different lead sources. The right axis shows the PL spectra of the perovskites prepared on glass, with photo-excitation at 507 nm. (b) The absorption spectra of perovskite films derived from different lead sources measured using photothermal deflection spectroscopy (PDS) technique. The inset shows the corresponding Urbach energies for all three samples.

A.2.4 Photovoltaic performance and characterization

We fabricated planar heterojunction solar cells employing the perovskite films prepared from the different lead sources, and present the results for the optimized devices in Figure A.7a. To achieve the best device performance, the perovskite films made from $PbCl_2$ and PbI_2 routes needed to be anneal for 2h and 40 min, respectively,

at their corresponding temperatures of 100 and 150 ℃. However, the optimised anneal time was much shorter for the films made from $PbAc_2$ route (5 min at 100 ℃), which is consistent with the much more facile removal of excess CH_3NH_3Ac during crystallization. Importantly, this represents a considerable saving in time, energy and capital expenditure when considering industrial scale manufacture of this technology. The average power conversion efficiency (PCE) with optimized annealing times for perovskites from $PbCl_2$, PbI_2 and $PbAc_2$ routes are 12.0, 9.3 and 14.0%, respectively. Therefore, by using $PbAc_2$ as lead source, we have not only achieved much faster and more uniform crystallization, but this has translated into improved device performance over the other two routes. The average open-circuit voltage (V_{oc}) of devices increases in the sequence PbI_2 (0.85 V) ~ $PbCl_2$ (0.88V) < $PbAc_2$ (0.99V). The lower voltages with PbI_2 and $PbCl_2$ derived samples can be explained by the increased shunting pathway due to contact between spiro-OMeTAD and TiO_2 compact layer from the non-continuous perovskite films, as evident from the SEM images (Figure A.4). This feature was further confirmed by electrochemical impedance spectroscopy (EIS) measurements showing that the recombination was severely suppressed by the $PbAc_2$ route. We also observed that the average fill factors (FFs) of devices via PbI_2 route are relatively low, in comparison to those based on $PbCl_2$ and $PbAc_2$ routes. The electron and hole diffusion lengths were observed to be much lower in the materials prepared via the PbI_2 route in this manner, due to much shorter electron and hole lifetimes[11,12]. This faster bulk recombination may explain the lower fill factors, which may be attributed to more defects in the film (consistent with the PDS measurements we show here) or due to the minor impurity of PbI_2 after annealing (as we also observed in the in XRD).

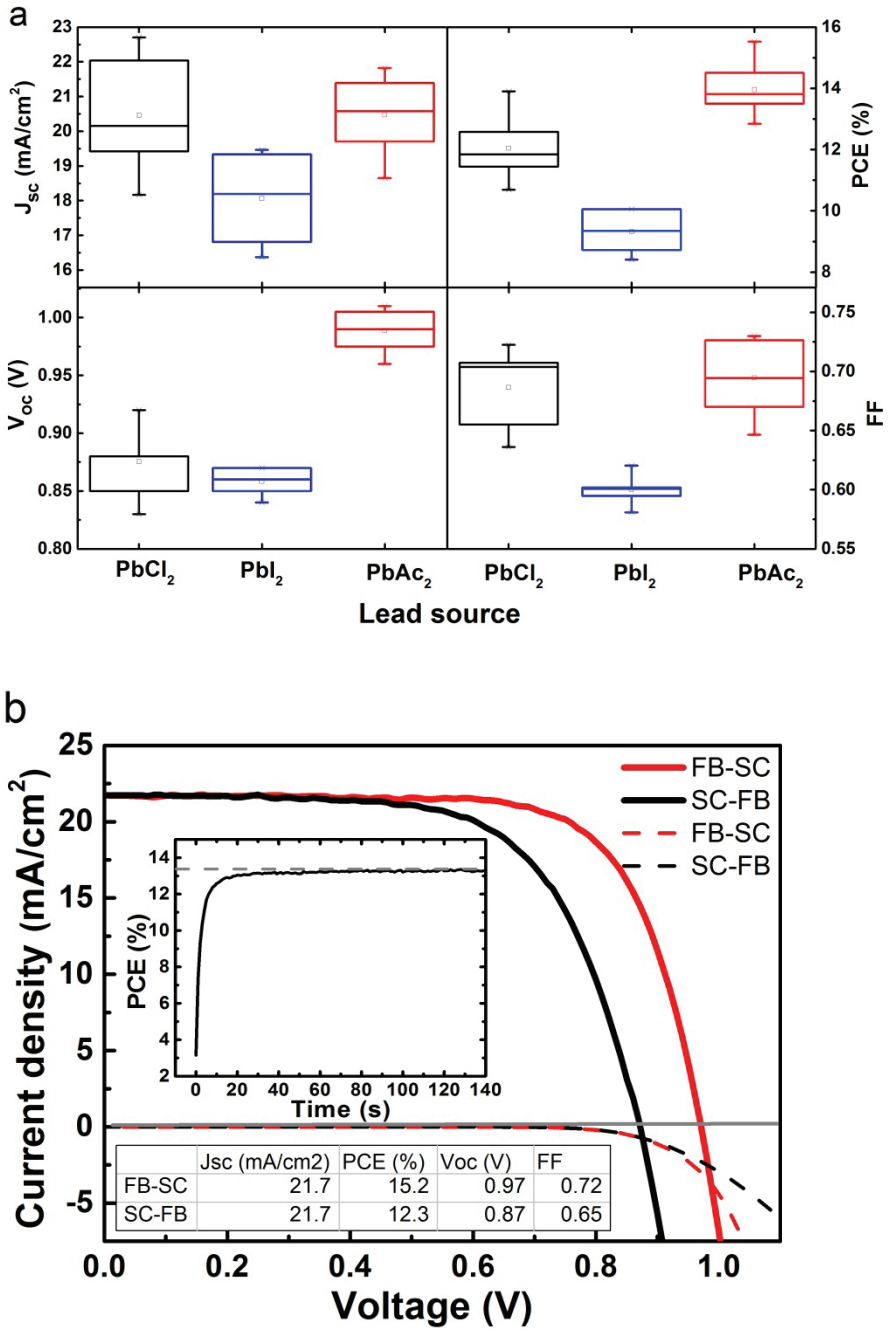

Figure A.7: (a) Device performance at optimized conditions using different lead sources measured under simulated AM1.5 sunlight of 100mW/cm^2 irradiance. (b) Current-density/voltage (J-V) curves of the best-performing device using $PbAc_2$ as lead source measured under simulated AM1.5 sunlight of 100mW/cm^2 irradiance (solid lines) and in the dark (dashed lines), with the stabilized power output of the same cell shown in the inset. All J-V scans were performed from forward bias to short circuit (FB-SC) and from short circuit to forward bias (SC-FB) at a scan rate of 0.15V/s. The data in (a) is derived from the FB-SC scans.

We show in Figure A.7b the J-V curve for the best device fabricated from $PbAc_2$ route measured under simulated AM 1.5G (100 mW/cm^2) solar irradiation in air, exhibiting outstanding performance with J_{SC} = 21.7 mA/cm^2, V_{OC} = 0.97 V, FF = 0.72, and PCE = 15.2% when scanned from forward bias (FB) to short-circuit (SC), and J_{SC} = 21.7 mA/cm^2, V_{OC} = 0.87 V, FF = 0.65, and PCE = 12.3% when scanned from SC to FB, so far among the highest efficiencies based on $CH_3NH_3PbI_3$ with a PHJ structure[5,7,10,26]. The stabilized power output of the same cell is shown in the inset, exhibiting a PCE of around 13.4%. For a planar heterojunction solar cell, this level of hysteresis and the difference between the two J-V curves determined and stabilized power output is relatively low[35].

A.3 Discussion

Through this study we have unraveled a number of previously perplexing issues associated with solution processed organic-inorganic thin film formation and crystallization, and in addition presented a new route to creating $CH_3NH_3PbI_3$ films which results in much faster and more uniform thin film formation. The specific steps in the perovskite crystallization from a solution containing excess organic component are:

1. During the initial stages of solution coating, solvent evaporation occurs, however the excess organic component remains predominantly entrapped with the film and full crystallization to the perovskite is strongly retarded. As such the excess organic component is responsible for the formation a uniform film. We note there may be a “precursor” material which forms from the starting composition during this stage[27].
2. The crystallization to the ABX_3 pervoskite *only* proceeds as the excess organic component is driven out of the film with increased enthalpy, but the temperature and time over which this process occurs depends strongly upon the by-product of the crystallization (CH_3NH_3X, X=Cl, I or Ac).
3. If the excess organic component is not volatile enough, we have to put in too much heat for too long to drive it out and the film morphology coarsens. What we do not know yet is what the impact of excessive heating has upon

the stoichiometry of the crystals, but we speculate that this may lead to CH_3NH_3 and halide deficiency which may be the cause for the increased energetic disorder in the perovskites fabricated via the PbI_2 route.

4. By choosing a by-product salt with volatility much higher than CH_3NH_3Cl and CH_3NH_3I we have managed to reduce the required thermal input and hence achieved crystallization faster resulting in much smoother films with smaller and fewer pinholes.

As an example, we show an illustration of the stages in the fabrication of $CH_3NH_3PbI_{3-x}Cl_x$ thin films in Figure A.8.

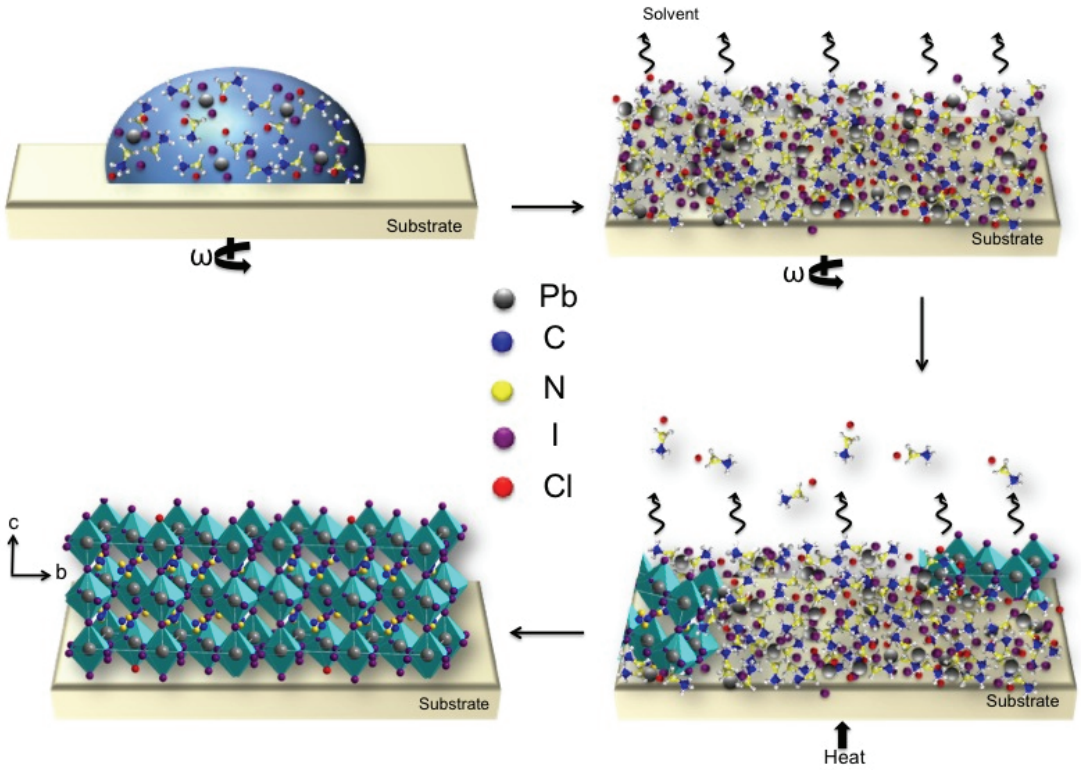

Figure A.8: Illustration of the stages in the fabrication of $CH_3NH_3PbI_{3-x}Cl_x$ thin films.

Through high-resolution elemental analysis, we confirmed that Cl does not exist at a high concentration in the perovskite films that we deposited on flat substrates using $PbCl_2$ as lead source in this study. The role of the Cl (in comparison to I) is to reduce the temperature at which the excess organic component can be driven off, enabling subsequent crystallization from an organic rich precursor. We cannot exclude

a direct electronic role of Cl, or incorporation of Cl at the grain boundaries or surfaces, but the current study is consistent with the main role being its influence on crystallization. The material fabricated from combining CH_3NH_3I and $PbCl_2$ has been referred to as a mixed halide perovskite $CH_3NH_3PbI_{3-x}Cl_x$. Even though the Cl content is likely to be very low, this notation remains relevant and clearly distinguishes between the $PbCl_2$ and PbI_2 routes. However, when non-halide lead sources are employed, we suggest simply referring to the material as $CH_3NH_3PbI_3$, but clearly identifying the fabrication route.

We note that we cannot exclude some excess organic component remaining within the film or being entrapped at the c-TiO_2/perovskite interface. We also have no precise knowledge of the time when solvent evaporation occurs, and whether entrapped solvent is driven out concurrently as the excess organic component is driven out of the film or if this happens sequentially and as such the relative importance of solvent organic component interaction remains uncertain.

In summary, we have systematically studied the role of the anions in the lead source during perovskite thin film crystallization. We found that the anions determine the perovskite crystal growth kinetics, which in turn affects the film morphology and device performance. The role of the excess organic component is to aid with uniform film formation in the early stages of film deposition. By changing lead halides ($PbCl_2$ and PbI_2) into a non-halide lead source ($PbAc_2$), we accelerated the crystal growth kinetics in the organic rich route, due to the facile removal of CH_3NH_3Ac. As such, by a simple one-step solution coating technique, we have enhanced both perovskite film smoothness and surface coverage, which in turn lead to better device performance. Also, a shorter annealing time will have a significant impact upon future manufacturing costs of perovskite solar modules. Importantly, this work demonstrates the possibility to tune the crystal growth kinetics by simple chemical management and opens an avenue to make uniform crystallized perovskite thin films at even lower temperatures by using other non-halide lead sources.

A.4 Methods

Perovskite solution preparation. Methylamine iodide (CH_3NH_3I) was prepared by reacting methylamine, 33 wt% in ethanol (Sigma-Aldrich), with hydroiodic acid (HI) 57 wt% in water (Sigma-Aldrich), at room temperature. HI was added dropwise while stirring. Upon drying at 100 ^oC, a white powder was formed, which was dried overnight in a vacuum oven and purified with ethanol before use. To generate the perovskite solution, CH_3NH_3I and PbX_2 (X= Cl, I, Ac) (Sigma-Aldrich) were dissolved in anhydrous N,N-Dimethylformamide (DMF) at a 3:1 molar ratio with final concentrations of ~40 wt%.

Substrate preparation. Devices were fabricated on fluorine-doped tin oxide (FTO) coated glass (Pilkington, 7Ω $\square^{-1}$). Initially, FTO was removed from regions under the anode contact by etching the FTO with 2M HCl and zinc powder. Substrates were then cleaned sequentially in 2% hallmanex detergent, acetone, propan-2-ol and oxygen plasma. A hole-blocking layer of compact TiO_2 was deposited by spin-coating a mildly acidic solution of titanium isopropoxide in ethanol, and annealed at 500°C for 30 minutes. Spin-coating was carried out at 2000 rpm for 60 seconds.

Perovskite deposition. For devices, the perovskites were prepared by spin-coating a 40 wt% perovskite solution at 2000 rpm in a nitrogen-filled glovebox. After spin-coating, the films were annealed at 100 °C for 5 minutes, 100 °C for 2 hours and 150 °C for 40 minutes for perovskites derived from $PbAc_2$, $PbCl_2$ and PbI_2 routes, respectively. The spiro-OMeTAD hole-transporting layer was then deposited from a 66 mM chlorobenzene solution containing additives of lithium bis(trifluoromethanesulfonyl)imide and 4-tert-butylpyridine. Finally, 120 nm silver electrodes were thermally evaporated under vacuum of ~10^{-6} Torr, at a rate of ~0.1nm/s, to complete the devices.

Characterization. XRD 2θ scans were obtained from samples of perovskite deposited on the compact-TiO_2 coated FTO glass using an X-ray diffractometer (Panalytical X'Pert Pro)

SEM A field emission scanning electron microscope (Hitachi S-4300) was used to acquire SEM images. The instrument uses an electron beam accelerated at 10 to 30 kV, enabling operation at a variety of currents.

AFM The atomic force microscopy (AFM) images were obtained using a ThermoMicroscope M5 in non-contact mode and scanning over a range of 15 μm by 15 μm at a resolution of 256 x 256 data points. The surface roughness was measured as the root mean squared roughness over the scanning area.

UV-Vis The absorbance of the perovskite films on compact-TiO_2 coated FTO glasses were measured on a Carry 300 Bio (Agilent Technologies). To reduce the sample variance, at least 3 samples were determined for each group and the average of all spectra presented.

Elemental Analysis The samples were made using the same spin-coating and annealing conditions for device fabrication. The pervoskite films were then carefully scratched off from the substrate in the glovebox. To determine the concentration of chlorine ion, 15 mg of sample was accurately weighted and filled into a flask with oxygen. The sample was then ignited and the combustion products were directly titrated in the combustion flask using $AgNO_3$ (0.1 μmol/μL, inject 1 μL each time, or corresponding to 30 ppm resolution).

Thermal gravimetric analysis (TGA) Thermal decomposition profiles of CH_3NH_3X (X=Cl, I, Ac) were recorded by a thermogravimetric analyzer TA Q500 in nitrogen atmosphere with a flow rate of 20 mL/min. The temperature varied from 25 °C to 600 °C at a heating rate of 10 °C/min. CH_3NH_3Ac was synthesized according to literature report[36].

PDS measurement The photothermal deflection spectroscopy (PDS) was performed using a setup similar to that previously reported by Jackson and co-workers[37]. We collected PDS measurements for perovskite films deposited on compact TiO_2 layer, following the same procedure we used to prepare the solar cells. For this particular measurement, we made use of quartz rather than the FTO coated glass to

minimize light absorption due to the substrate. During the measurement we kept the samples in a hermetically sealed quartz cuvette filled with an inert liquid, Fluorinert FC-72 from 3M Corporation, which acts as deflection medium with high temperature dependent refractive index. We excited the perovskite films from the quartz side with a modulated monochromated light beam perpendicular to the plane of the sample. Modulated monochromated light beam was produced by a combination of a Light Support MKII 100 W Xenon arc source and a CVI DK240 monochromator. The transverse probe beam was produced with Qioptiq 670 nm fiber-coupled diode laser and passed as close as possible to the perovskite film surface. Beam deflection was measured using a differentially amplified quadrant photodiode and a Stanford Research SR830 lock-in amplifier.

Photoluminescence (**PL**) Samples consisted of perovskites prepared on glass and coated with the inert polymer poly(methyl methacrylate) (PMMA). PL spectra were acquired using a time-resolved single photon counting setup (FluoTime 300, PicoQuant GmbH). Samples were photoexcited using a 507 nm laser head (LDH-P-C-510, PicoQuant GmbH) with pulse duration of 117 ps, fluence of ~0.03μJ/cm^2/pulse, and a repetition rate of 10 MHz.

Wide angle X-ray scattering (WAXS)

Samples were spin-coated at the Cornell High Energy Synchrotron Source (CHESS) and loaded on a custom-built temperature-controlled grazing incidence stage at the D1 beamline[38], with a typical transfer period of 2-5 minutes. Images were collected using a Pilatus 300 K high speed pixel array detector, 487×619 pixels with 172 μm/pixel resolution, at a distance of 93 mm from the sample. The x-ray wavelength was 0.1155 nm and the incident beam angle was approximately 0.5°, well above the substrate critical angle. Typical exposure times were <1 second. Samples were moved after each exposure to avoid beam damage and the total spectra for a given sample collected at 12-16 different locations. 2D WAXS images were integrated using the Fit2D software package from ESRF; background subtraction and peak area calculations were performed using IGOR, a commercially available software product.

Impedance Electrochemical impedance (EIS) measurements were performed under open-circuit conditions by illuminating the solar cells using a powerful LED array (maximum output power of 306 lumen at 700 mA driving current), emitting light at 627 nm. Light intensities were adjusted by controlling the diode's current by a LED driver; the LED was previously calibrated employing a Si reference photodiode. The illuminated area of the solar cells was set at 0.0625 cm^2, using a mask. The spectra were recorded by varying the frequency range from 100 KHz to 10 mHz (amplitude of voltage perturbation: 15 mV RMS) using an electrochemical working station (Autolab PGSTAT302N, Ecochemie) and its built-in frequency response analyzer (FRA2). The recorded spectra were fitted using the NOVA software.

Solar cell characterization The current density–voltage (J-V) curves were measured (2400 Series SourceMeter, Keithley Instruments) under simulated AM 1.5 sunlight at 100 $mWcm^{-2}$ irradiance generated by an Abet Class AAB sun 2000 simulator, with the intensity calibrated with an NREL calibrated KG5 filtered Si reference cell. The mismatch factor was calculated to be less than 1%. The solar cells were masked with a metal aperture to define the active area, typically 0.0625 cm^2 (measured individually for each mask) and measured in a light-tight sample holder to minimize any edge effects and ensure that the reference cell and test cell are located in the same spot under the solar simulator during measurement.

A.5 References

1. Lee, M. M., Teuscher, J., Miyasaka, T., Murakami, T. N. & Snaith, H. J. Efficient hybrid solar cells based on meso-superstructured organometal halide perovskites. *Science* **338**, 643-647 (2012).
2. Kim, H.-S. *et al.* Lead iodide perovskite sensitized all-solid-state submicron thin film mesoscopic solar cell with efficiency exceeding 9%. *Scientific reports* **2** (2012).
3. Heo, J. H. *et al.* Efficient inorganic-organic hybrid heterojunction solar cells containing perovskite compound and polymeric hole conductors. *Nature photonics* **7**, 486-491 (2013).
4. Burschka, J. *et al.* Sequential deposition as a route to high-performance perovskite-sensitized solar cells. *Nature* **499**, 316-319 (2013).

5. Liu, M., Johnston, M. B. & Snaith, H. J. Efficient planar heterojunction perovskite solar cells by vapour deposition. *Nature* **501**, 395-398 (2013).

6. Malinkiewicz, O. *et al.* Perovskite solar cells employing organic charge-transport layers. *Nature Photonics* **8**, 128-132 (2014).

7. Liu, D. & Kelly, T. L. Perovskite solar cells with a planar heterojunction structure prepared using room-temperature solution processing techniques. *Nature Photonics* (2013).

8. Jeon, N. J. *et al.* Solvent engineering for high-performance inorganic–organic hybrid perovskite solar cells. *Nature materials* (2014).

9. Hodes, G. Perovskite-based solar cells. *Science* **342**, 317-318 (2013).

10. Chen, Q. *et al.* Planar heterojunction perovskite solar cells via vapor-assisted solution process. *Journal of the American Chemical Society* **136**, 622-625 (2013).

11. Stranks, S. D. *et al.* Electron-hole diffusion lengths exceeding 1 micrometer in an organometal trihalide perovskite absorber. *Science* **342**, 341-344 (2013).

12. Xing, G. *et al.* Long-range balanced electron-and hole-transport lengths in organic-inorganic CH3NH3PbI3. *Science* **342**, 344-347 (2013).

13. Kojima, A., Teshima, K., Shirai, Y. & Miyasaka, T. Organometal halide perovskites as visible-light sensitizers for photovoltaic cells. *Journal of the American Chemical Society* **131**, 6050-6051 (2009).

14. Ball, J. M., Lee, M. M., Hey, A. & Snaith, H. J. Low-temperature processed meso-superstructured to thin-film perovskite solar cells. *Energy & Environmental Science* **6**, 1739-1743 (2013).

15. Green, M. A., Ho-Baillie, A. & Snaith, H. J. The emergence of perovskite solar cells. *Nature Photonics* **8**, 506-514 (2014).

16. Noh, J. H., Im, S. H., Heo, J. H., Mandal, T. N. & Seok, S. I. Chemical management for colorful, efficient, and stable inorganic–organic hybrid nanostructured solar cells. *Nano letters* **13**, 1764-1769 (2013).

17. Pellet, N. *et al.* Mixed-Organic-Cation Perovskite Photovoltaics for Enhanced Solar-Light Harvesting. *Angewandte Chemie International Edition* **53**, 3151-3157 (2014).

18. Ogomi, Y. *et al.* CH3NH3Sn x Pb (1–x) I3 Perovskite Solar Cells Covering up to 1060 nm. *The Journal of Physical Chemistry Letters* **5**, 1004-1011 (2014).

19. Hao, F., Stoumpos, C. C., Chang, R. P. & Kanatzidis, M. G. Anomalous band gap behavior in mixed Sn and Pb perovskites enables broadening of absorption spectrum in solar cells. *Journal of the American Chemical Society* (2014).

20. Zhao, Y. & Zhu, K. CH3NH3Cl-Assisted One-Step Solution Growth of CH3NH3PbI3: Structure, Charge-Carrier Dynamics, and Photovoltaic Properties of Perovskite Solar Cells. *The Journal of Physical Chemistry C* (2014).

21. Moore, D. T., Sai, H., Tan, K. W., Estroff, L. A. & Wiesner, U. Impact of the organic halide salt on final perovskite composition for photovoltaic applications. *APL Materials* **2**, 081802 (2014).

22. Eperon, G. E., Burlakov, V. M., Docampo, P., Goriely, A. & Snaith, H. J. Morphological Control for High Performance, Solution-Processed Planar Heterojunction Perovskite Solar Cells. *Advanced Functional Materials* **24**, 151-157 (2014).

23. Conings, B. *et al.* Perovskite-Based Hybrid Solar Cells Exceeding 10% Efficiency with High Reproducibility Using a Thin Film Sandwich Approach. *Advanced Materials* **26**, 2041-2046 (2014).

24. You, J. *et al.* Low-Temperature Solution-Processed Perovskite Solar Cells with High Efficiency and Flexibility. (2014).

25. Colella, S. *et al.* MAPbI3-xCl x Mixed Halide Perovskite for Hybrid Solar Cells: The Role of Chloride as Dopant on the Transport and Structural Properties. *Chemistry of Materials* **25**, 4613-4618 (2013).

26. Docampo, P. *et al.* Solution Deposition-Conversion for Planar Heterojunction Mixed Halide Perovskite Solar Cells. *Advanced Energy Materials* (2014).

27. Tan, K. W. *et al.* Thermally Induced Structural Evolution and Performance of Mesoporous Block Copolymer-Directed Alumina Perovskite Solar Cells. *ACS nano* **8**, 4730-4739 (2014).

28. Dualeh, A. *et al.* Effect of Annealing Temperature on Film Morphology of Organic–Inorganic Hybrid Pervoskite Solid-State Solar Cells. *Advanced Functional Materials* (2014).

29. Haslam, J., Hamilton, J. B. & Squirrell, D. C. M. The determination of chlorine by the oxygen flask combustion method: a single unit for electrical ignition by remote control and potentiometric titration. *Analyst* **85**, 556-560 (1960).

30. Mosconi, E., Ronca, E. & De Angelis, F. First Principles Investigation of the TiO2/Organohalide Perovskites Interface: The Role of Interfacial Chlorine. *The Journal of Physical Chemistry Letters* (2014).

31. De Bastiani, M., D'Innocenzo, V., Stranks, S. D., Snaith, H. J. & Petrozza, A. Role of the crystallization substrate on the photoluminescence properties of organo-lead mixed halides perovskites. *APL Materials* **2**, -, doi:http://dx.doi.org/10.1063/1.4889845 (2014).

32. Urbach, F. The long-wavelength edge of photographic sensitivity and of the electronic absorption of solids. *Physical Review* **92**, 1324 (1953).

33. De Wolf, S. *et al.* Organometallic Halide Perovskites: Sharp Optical Absorption Edge and Its Relation to Photovoltaic Performance. *The Journal of Physical Chemistry Letters* **5**, 1035-1039 (2014).

34. Kim, J., Lee, S.-H., Lee, J. H. & Hong, K.-H. The Role of Intrinsic Defects in Methylammonium Lead Iodide Perovskite. *The Journal of Physical Chemistry*

Letters **5**, 1312-1317 (2014).

35. Snaith, H. J. *et al.* Anomalous Hysteresis in Perovskite Solar Cells. *The Journal of Physical Chemistry Letters* **5**, 1511-1515 (2014).
36. Buckingham, D. A., Clark, C. R., Rogers, A. J. & Simpson, J. Synthesis and Structures of Five [Co (Mecyclen)(S-AlaO)] 2+ Isomers: Use of nOe and COSY 1H NMR Spectroscopy for Structural Assignment in Solution. *Inorganic Chemistry* **34**, 3646-3657 (1995).
37. Jackson, W. B., Amer, N. M., Boccara, A. C. & Fournier, D. Photothermal deflection spectroscopy and detection. *Applied Optics* **20**, 1333-1344 (1981).
38. Bian, K. *et al.* Shape-anisotropy driven symmetry transformations in nanocrystal superlattice polymorphs. *ACS nano* **5**, 2815-2823 (2011).

A.6 Acknowledgements

The authors acknowledge the EPSRC Supergen, ERC Hyper Project for financial support and thank Prof. Ming-Hui Lu for elemental analysis and Ms Mingzhen Liu for providing vapor-deposited perovskite film for AFM study. D.T.M. acknowledges financial support from the National Science Foundation (NSF) through the Materials World Network grant (DMR-1008125 and DMR-1210304). This work made use of the research facilities of the Cornell High Energy Synchrotron Source (CHESS) which is supported by the NSF and the NIH/National Institute of General Medical Sciences under NSF award DMR-1332208. The authors acknowledge the use of Fit2D for WAXS data analysis and thank AP Hammersley and ESRF, for its development and free use.

Author contributions

W.Z. and H.J.S. conceived of the project. W.Z. performed the device fabrication and characterization. M.S., M. T. H. and J.A.W. contributed to the film morphology study. S.K.P. performed TGA analysis. M.S. prepared samples for WAXD and D.T.M., L.A.E. and U.W. contributed to WAXD study and analysis. A.A., A.S. and S.D.S performed optical measurements. G.E.E. performed XRD analysis. T.S. performed EIS study. S.Y. and Y.C. contributed to the elemental analysis. W.Z. wrote the first draft of the paper. All authors contributed to the writing of the paper.

APPENDIX B: SOLUTION PROCESSED PEROVSKITE THIN FILMS USING AN IONIC LIQUID SOLVENT

The work presented in this dissertation was done to elucidate the crystallization pathway for the halide perovskites with the goal of controlling that crystallization. Generally speaking, controlling crystal growth requires knowledge of the starting state, the ending state, and the way in which the system moves between the two. In the present case, we know the composition of the starting state but not the exact material. Additionally, the pathway between the starting and ending states requires some heat which, unfortunately, also accelerates the undesirable process of decomposition. Therefore, in order to gain better control over the crystal growth we need a more specific knowledge of the starting state and a method by which the temperature for crystallization can be decoupled from the temperature for decomposition.

Chapter 5 of this dissertation details a kinetic study which includes the use of lead acetate or nitrate salts; perovskites made from either of these salts can be crystallized near room temperature and in very short times, 3-10 minutes. The transformation to perovskite in 5 minutes at 40 °C tells us that the complete removal of the solvent and excess spectator salt are not a requirement for the crystallization; the temperature can be decoupled. The second requirement is an exact knowledge of the starting state; this could be accomplished by further elucidation of the precursor structure or, as an alternative, the development of a crystallization pathway in which there is no precursor structure. If a processing pathway can be developed in which the perovskite crystallizes directly from the solution phase we would also have a well defined starting point.

In order to solve both of the issues noted above we proceeded by exploring the use of an ionic liquid (IL) as the solvent, rather than the typical organic solvents that have been reported. Ionic liquids have several properties which could allow for direct crystallization as well as a decoupling of the temperature:

- ILs are highly polar, a requirement of any solvent used for lead halide salts
- ILs have negligible vapor pressure at temperatures below the boiling point

- ILs have strong solvating effects for ionic solids

The high polarity and low vapor pressure should allow us to decouple the crystallization temperature from the decomposition. The high polarity allows for the use of an IL as the solvent, removing the organic solvent from the process. Use of an IL whose boiling point is well above the crystallization temperature would allow for the tuning of crystal growth times and temperatures without the risk of decomposition as the solvent would still be present. The strong solvation effects of ILs on ionic solids ensures that only structures with a large ΔG of crystallization will form, higher energy, metastable phases are less likely as they will stay solvated.

The initial approach was to look at organic cation ILs, specifically methylammonium; this was done to invoke Le Chatelier's Principle with respect to the decomposition. Since the decomposition consists of the removal of (MA)I units from the perovskite, saturation of the solvent with (MA) should inhibit this effect as long as the solvent is still there. Investigation of the literature showed that there is one, all organic, (MA) based IL, methylammonium formate. We used methylammonium formate as the solvent with stoichiometric ratios of PbI_2 and (MA)I and deposited films using the same spincoating or spraycoating methods used in the other work reported here. This work is ongoing and we report here only the preliminary results.

The primary result, thus far, is the successful crystallization of (MA)PbI3 from a one-step, solution based, deposition method directly from solution with no precursor material. Figure B.1 shows a time series of integrated 2D WAXS data taken from spuncast films at 50 °C. It is clear from the plots that the initial crystal phase is the perovskite, with the (110) peak reflection being the first discernable peak. Additionally, the entire crystallization is completed in ~6 minutes after deposition with the transition itself taking less than 2 minutes.

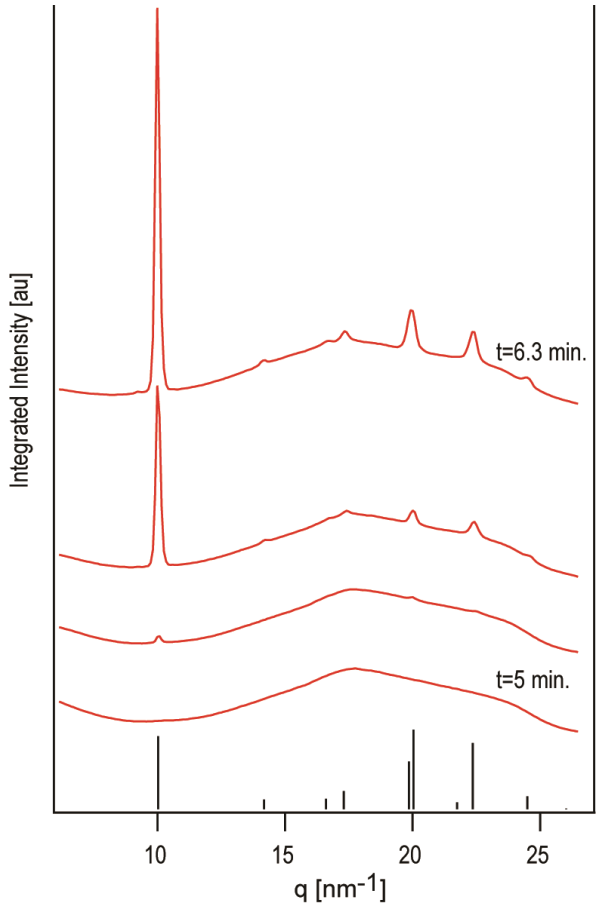

Figure B.1: Integrated 2D WAXS patterns for spincast films of (MA)PbI3 using methylammonium formate as the solvent. Bottom trace is the last trace for which no diffraction peaks are present, top trace is the first trace for which crystallization is complete, intermediate traces are evenly time-spaced.

To explore the manner in which the films grow we employed an airSEM, which allows for imaging at typical SEM resolutions but in air. The lack of need for high vacuum in the SEM allows for in situ imaging of the film growth from a wet film. Figure B.2 shows a time lapse of a film grown at 50 °C, with two distinct regions marked in panel (a); "A" denotes preexisting nuclei and we can track the resulting growth in time, "B" denotes an area with no nuclei that was monitored for the appearance of new nuclei after growth has begun. Two things are clear from the time lapse, growing domains continue to grow until they are impinged, and nucleation continues after the growth phase begins. This result infers that controlling the nucleation will be a key step in making films with larger crystal domains; if nucleation

centers are too close together impingement will limit their growth, if too far apart the film will not be continuous.

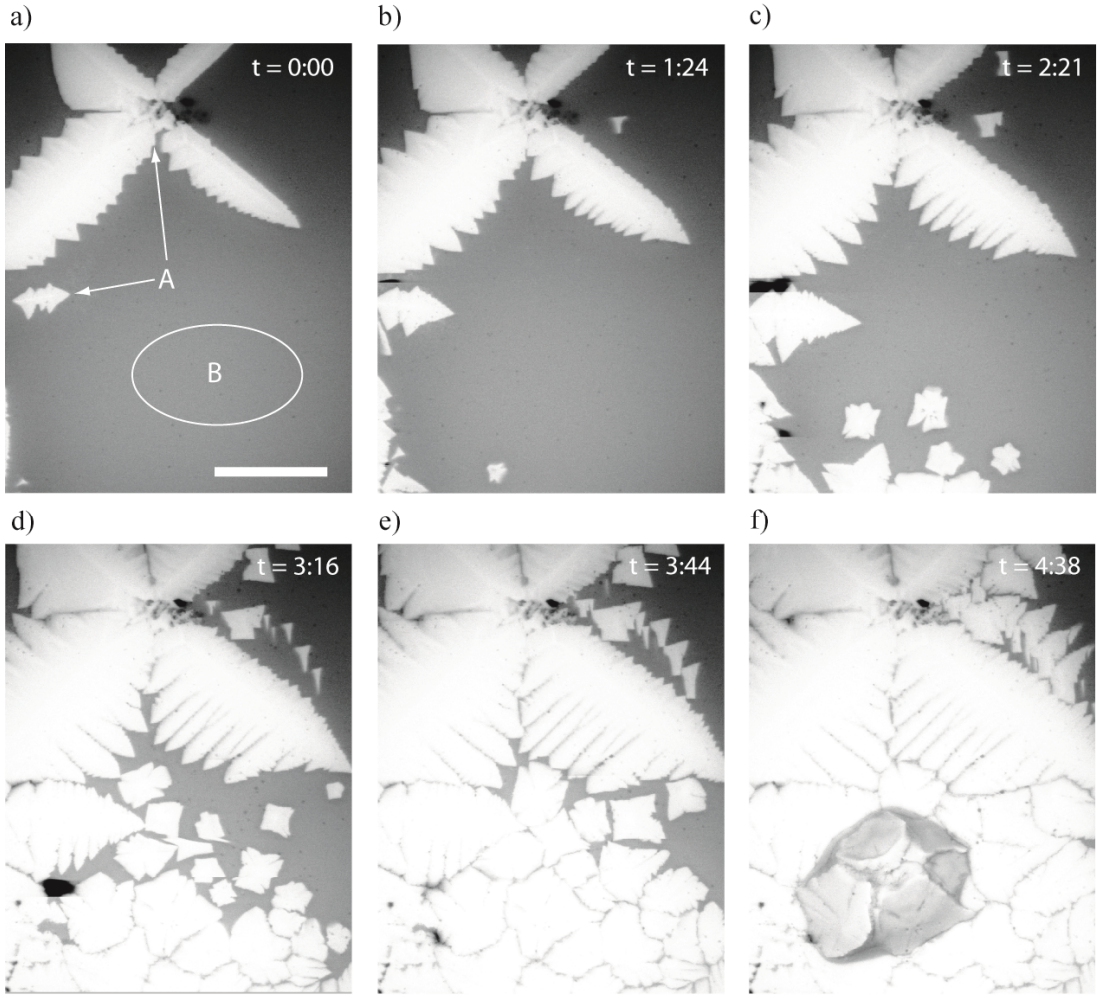

Figure B.2: SEM micrographs of (MA)PbI3 thin films made using (MA) formate as the solvent, films were spin cast and immediately placed into the airSEM. The first image (a) was taken at ~ 6 minutes after the completion of the spin cycle with subsequent times marked on each panel, scale bar (shown on a only) is 50 microns.

The large dendrite at the top of the micrographs (the topmost "A" site) appears to be growing into a square, however, it never completes due to impingement. It may be the case that the creation of large, 2D crystals happens by the coalescence of 4 orthogonal dendrites similar to the one shown here. To check this we made a film from a very dilute solution and using a very high spin speed in order to create a sparsely covered substrate. Figure B.3 shows the result of this test; many square

crystals appear on the substrate and in Fig. B.3b we see clear indications of 2D growth steps implying that these square domains are single crystals.

a) b)

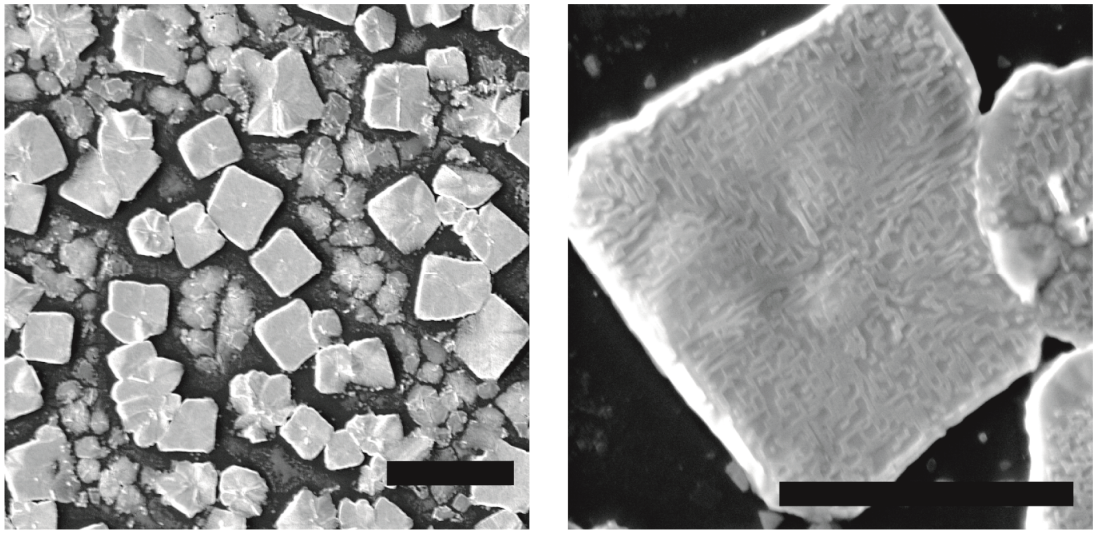

Figure B.3: SEM micrographs of single crystals grown using methylammonium formate as the solvent; scale bars are 10 micrometers and 3 micrometers for (a) and (b) respectively.

Lastly, to test the formate systems decoupling of the crystallization time from the decomposition we grew a film at 35 °C for 16 hours under a mild vacuum (~ 10 torr). Figure B.4 shows micrographs of the film as well as the resulting XRD pattern. The XRD pattern shows no indication of decomposition to PbI_2 while the film morphology now consists of 100% coverage of the substrate. Although this is only a preliminary result, it suggests that the temperature/time parameters can be tuned to achieve the film and crystal morphology desired without concern of the decomposition effects.

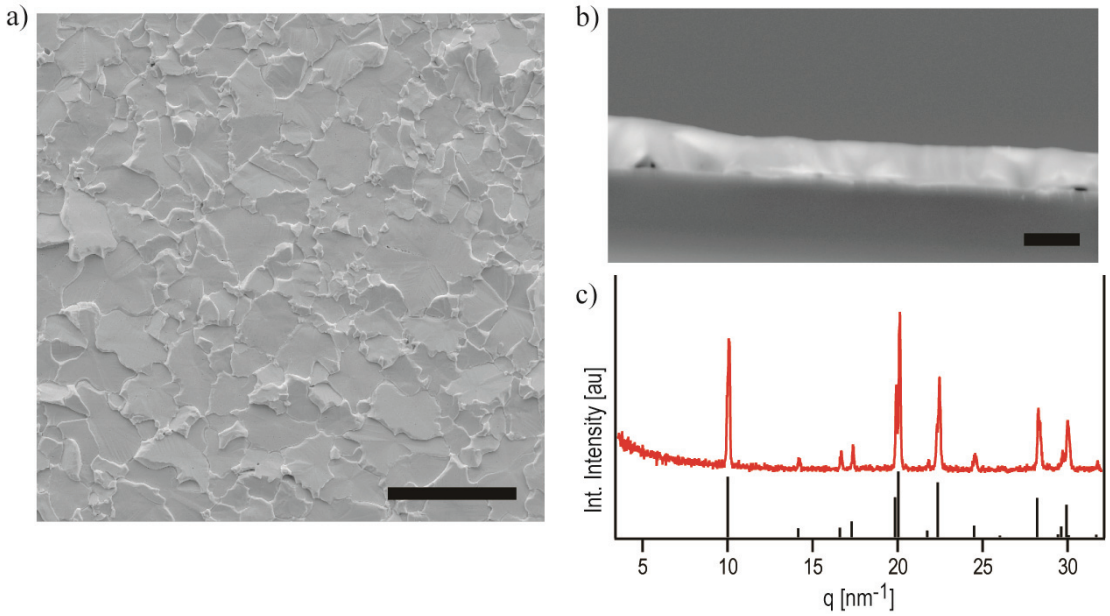

Figure B.4: SEM micrographs (a and b) and XRD pattern (c) of thin film grown using methylammonium formate as the solvent; scale bars are 100 micrometers and 1 micrometer for (a) and (b) respectively.

Although there is still much work to be done on the formate system, it shows promise in providing a low temperature, high throughput deposition process capable of producing continuous, well oriented films. Additionally, this process uses inexpensive (and recoverable) solvents, is one-step for the deposition, and produces films faster and at lower temperatures than any previously reported process.